THE UNIVERSITY OF MICHIGAN

INDUSTRY PROGRAM OF THE COLLEGE OF ENGINEERING

PLASTIC DEFORMATION OF NONMETALLIC PHASES WITHIN DUCTILE METALS

Robert J. Warrick

A dissertation submitted in partial fulfillment
of the requirements for the degree of
Doctor of Philosophy in the
University of Michigan
Department of Chemical and Metallurgical Engineering
1963

June, 1963

IP-626

To my wife

ACKNOWLEDGEMENTS

It is my pleasure to acknowledge a number of individuals and organizations for their indispensable assistance during the course of this investigation.

I am particularly grateful to Professor Lawrence H. Van Vlack who served as Chairman of the Doctoral Committee. He stimulated interest in the topic, provided encouragement throughout the experimental work, and was always available for helpful discussions.

Invaluable aid was received from the Doctoral Committee Members. Professor Robert M. Haythornthwaite made many helpful suggestions for test and stress analysis methods. The interest, discerning discussions and advice of Professors James M. Freeman, Maurice J. Sinnott, and Lars Thomassen are appreciated, as are those of Professor C. T. Yang who served on the Doctoral Committee while still at the University of Michigan.

I should like to thank the faculty of the Department of Chemical and Metallurgical Engineering who provided helpful discussions and aid during the course of my graduate work and the departmental shop personnel who helped with equipment and supplies.

Valuable discussions and assistance with experimental programs were obtained from a number of my fellow graduate students. In particular, I wish to thank Mr. John W. Moore, Mr. Robert M. Rusnak, Mr. William E. Sutar, and Mr. John W. Upp for their help with metallographic work and routine measurements.

The financial support for the thesis was provided by the National Science Foundation. The Wheelabrator Corporation and the General Electric Company supported part of my graduate work through fellowships.

I wish to acknowledge Miss Dolores Gillies, who typed the first draft of the thesis, and the Industry Program of the College of Engineering, which prepared the dissertation in its final form.

TABLE OF CONTENTS

TABLE OF CONTENTS (CONT'D)

TABLE OF CONTENTS (CONT'D)

TABLE OF CONTENTS (CONT'D)

LIST OF TABLES

LIST OF FIGURES

LIST OF FIGURES (CONT'D)

LIST OF FIGURES (CONT'D)

LIST OF FIGURES (CONT'D)

LIST OF FIGURES (CONT'D)

ABSTRACT

The plastic deformation of nonmetallic inclusions in a ductile metal matrix was studied. Primary emphasis was on the effects of extrusion parameters and sample variations on the fracture and flow of the included nonmetallic phase. Secondary emphasis was on strain hardening and flow patterns during extrusion, effect of extrusion parameters and sample variations on extrusion pressure, and properties of two phase materials.

The experimental materials included face-centered cubic metals (Pb, Al, Ag, Cu, and brass) and inclusions with the NaCl structure (KCl, NaCl, NaF, and LiF). Samples were prepared using standard powder metallurgical techniques.

Extrusion was used as the deformation method since it provides stress states the same as, or similar to, those found in the common metal forming operations, i.e., extrusion, drawing, and rolling. Consequently, the results should apply for these forming operations.

After extrusion, the samples were sectioned on a symmetry plane parallel to the extrusion direction. Inclusion length/width ratios were measured in this plane as an index of the amount of inclusion deformation while inclusion and matrix hardnesses were used as an index of the relative properties of the phases.

A modification of Shield's stress analysis for plastic flow in a converging connical channel was used to calculate stress distributions. However, accurate stress distributions were not achieved because of an inability to accurately evaluate the stress required to change the direction

of material flow at the die entry and exit sections. As a result, ram pressure was used as an index of the stress levels in the samples.

The ram pressure required for extrusion can be reduced by (1) use of more effective lubricants, (2) proper deformation equipment design, (3) decreasing the sample reduction, (4) decreasing the extrusion velocity, (5) increasing the extrusion temperature, and (6) decreasing the sample yield strength.

NaCl-type ionic inclusions were found to have high ductilities when subjected to the confined stress conditions that accompany extrusion.

As the stress levels are increased, three types of inclusion behavior occur: (1) rigid inclusions, (2) brittle-ductile inclusions (fracture and deformation occur), and (3) ductile inclusions. For a given sample, the minimum stress acting on the inclusions is limited by the relative metal/inclusion hardness ratio.

The amount of inclusion deformation can be decreased by the following process changes: (1) use of more effective lubricants, (2) proper deformation equipment design, (3) decreasing the sample reduction, (4) decreasing the strain rate, and (5) proper operating temperature selection.

The amount of inclusion deformation can be controlled by the following material variations: (1) changing the relative yield strengths of the phases, and (2) changing the relative amounts of the phases. Inclusion size does not have a major effect on the amount of inclusion deformation.

CHAPTER I

INTRODUCTION

This investigation is concerned with the fracture and plastic deformation of NaCl-type nonmetallic inclusions in a face-centered cubic metal matrix. The topic is of importance since the deformation, or fracture and dispersion, of nonmetallic inclusions during forming operations can have a marked effect on the properties of a metal. In addition, increased usage of two phase materials, such as cermets, has created interest in the way these materials deform under load.

As a hypothesis, it was suggested that the fracture and plastic deformation characteristics of an included ionic solid would be governed by the stress states acting on the inclusions. These stress states are expected to be influenced by both deformation process variables and sample parameters. For example, as sample reductions or metal/inclusion hardness ratios change, the stress levels acting on the inclusions would be expected to change. This change in stress levels would be expected to influence inclusion fracture and deformation behavior. A systematic investigation of the effects of process and sample variations was undertaken to determine the parameters affecting fracture and flow characteristics of an included ionic solid.

While primary thesis emphasis was on the fracture and flow of an included nonmetallic phase, supplemental information was obtained in the areas of strain hardening and flow patterns during extrusion, effects of extrusion parameters and sample variations on extrusion pressure, and properties of two phase materials.

A study of sulfide inclusions in steel[1] stimulated the author's interest in this topic. Consequently, experimental materials were selected to match the face-centered cubic structure of austenite and the NaCl structure of MnS. Materials were selected to provide model systems allowing a broad range of sample variations; and to permit study at low deformation temperatures. The extensive literature on the properties of NaCl-type ionic solids makes them advantageous for study.

Extrusion was used as the deformation method since it permits the study of a broad range of deformation parameters. In addition, extrusion provides stress states which are the same as, or similar to, those found in common metal forming operations; i.e., extrusion, drawing, and rolling.

The effects of the following process and sample variations were studied:

1. Die angle.
2. Per cent reduction in area.
3. Strain rate.
4. Temperature.
5. Per cent nonmetallic material.
6. Nonmetallic inclusion size.
7. Nonmetallic inclusion type.
8. Matrix type.

CHAPTER II

LITERATURE REVIEW

This literature review presents material which is important to the study and understanding of the thesis topics. Pertinent references will be considered under the following headings:

A. Deformation of Nonmetallic Materials.

B. Deformation of Included Nonmetallic Materials.

C. Hardness and Yield Strength for Two Phase Systems.

D. Extrusion.

A. Deformation of Nonmetallic Materials

Ionic crystals have a special place in the history of crystal plasticity since they were among the first to be investigated systematically. Because of their ionic bonds, ceramic materials generally have higher stability, melting temperature, hardness, and resistance to chemical alteration than metals or organic materials.[2] Consequently, they are interesting materials for many engineering applications. However, lack of sufficient ductility limits their application in many cases.

Ionic materials were long thought to be inherently brittle. However, in 1867, Reusch[3] studied the deformation of rock salt crystals and reported glide on (110) planes in the [110] directions. In 1903, Coblentz[4] reported that NaCl crystals can be plastically bent if their surfaces are first wetted and in 1909, Milch[5] reported that sticks of rock salt could be bent very readily after heating. Since these early experiments with NaCl, investigators have demonstrated the ductility of

many alkali halides, sulfides, and oxides.[6-19] Plastic deformation has been observed in ceramic phases having a wide range of crystal structures: for example, NaCl structure (MnS, MgO, NaCl, KCl, LiF),[6,7] CsCl structure (CsBr),[7] CaF_2 structure (Cu_2S,[8] CaF_2[9,10]), hexagonal structure (Al_2O_3,[11,12] SiO_2,[13] $CaCO_3$[14]), and diamond cubic structure (diamond).[15]

The greatest ductility has been observed in ionic materials having the NaCl structure. Because only ionic materials with the NaCl structure were used in this thesis, and since the preponderance of the literature is devoted to such materials, most of the review will be devoted to NaCl type materials.

The deformation characteristics of ionic solids will be considered under the following headings:

1. Slip and Fracture Systems.
2. Strength.
3. Plastic Deformation.
4. Fracture.

The fracture stress for ionic materials is generally lower than the yield stress. Consequently, factors which control fracture behavior will be considered in detail.

For a more general discussion of the mechanical properties of ionic solids, the reader is referred to the classic work of Schmid and Boas (1936)[16] and the more recent reviews by Laurent (1958),[17] Pask (1961),[18] and Gilman (1961).[19]

1. Slip and Fracture Systems

Plastic deformation of ionic crystals occurs by the movement of dislocations through the lattice. The primary slip system for KCl, NaCl, NaF, and LiF is (110) [110] while the secondary slip system is (100) [110].[20-24] Buerger[22] and Tammann and Salge[25] report slip on the (111) [110] system for NaCl at elevated temperatures. The probability of (100) [110] slip increases with increasing temperature and increasing ion polarizability. PbS and PbTe, which have high polarizability, use the (100) [110] glide system at room temperature.[22,23,26]

For all active glide planes, the [110] glide direction requires the least displacement for structure restoration. In addition, like ions do not pass over each other with this glide direction.

In many crystals, the slip planes are those of widest spacing (densest packing). These are the (100) planes for NaCl type materials. Huntington, Dickey, and Thompson[27] made detailed calculations of the dislocation energies for glide in NaCl. Their calculations show that screw dislocations have a definite preference for (110) planes rather than (100) planes. Their results were not as clear for the preference of (110) planes over (100) planes for edge dislocations.

Ionic crystals cleave along (100) planes with secondary cleavage along (110) planes.[19] For cleavage with no accompanying plastic deformation or step formation, the energy required to form new surface represents the surface energy of the material. Surface energies calculated by Van Zeggeren and Benson[28] using the Born Mayer hard sphere model predict the observed cleavage behavior.

2. Strength of Ionic Solids

In a perfect crystal, dislocation nucleation by the action of stress alone would be expected to occur with stresses of approximately $G/4\pi$.[19] Sears,[29] Gyulai,[30] and Hulse[31] have shown that "whiskers" of LiF, NaCl, and MgO can withstand very high stresses without the occurance of plastic flow. Stokes[32] has shown that bulk MgO crystals can withstand stresses within 1/10 of their theoretical strength. He removed "fresh" surface dislocations by chemical polishing and "grown in" dislocation sources (inclusions and precipitate particles) by annealing.

3. Plastic Behavior of Ionic Solids

The plastic behavior of ionic solids will be discussed under the following headings:

a. Yield Stress.

b. Surface Effects.

a. Yield Stress-The yield stresses of ionic crystals are determined primarily by the stresses required to nucleate and move dislocations in them. The effect of dislocation source has been demonstrated by Stokes[32] for MgO crystals. "Fresh" dislocations, introduced by cleavage or mechanical contact, move and multiply to generate slip bands at approximately 3,000 psi. The crystal can be quite ductile under these conditions. When the "fresh" dislocations are removed by chemical polishing, the crystals have to depend on "grown-in" dislocations which are considered to be associated with precipitate particles or inclusions. Chemically polished crystals deform elastically for stresses up to $> 70{,}000$ psi. Crystals which rely on "grown-in" dislocation sources or

homogeneous dislocation nucleation often fracture at, or soon after, yield. This is probably a result of crack nucleation at intersecting slip bands. (See section A-4-b of this chapter.)

When "fresh" dislocations are present in a crystal, the yield stress is determined by the stress required to move dislocations in the crystal. This was demonstrated by Johnston and Gilman[33] who showed that the macroscopic yield stresses of crystals are linearly proportional to the stresses required to cause motion of "fresh" dislocations. Consequently, when fresh sources are present, the yield stress is determined by the resistance of the crystal to dislocation motion.

Ender,[34] Schoenfeld,[35] and Metag[36] show the effect of various solute additions on the yield strength of NaCl. Luhman and Gorum[37] and Gorum, Luhman, and Pask[38] made the same type of studies for AgCl and MgO respectively. In all cases, solute additions increase the yield strength. The rate of strain hardening was observed to increase with increasing solute additions. Divalent ion additions to NaCl and AgCl have a much greater effect than monovalent ions which may be explained in part by charged dislocations as discussed later in this section.

For a given material and temperature, Phillips[39] reports that an increase in the strain rate results in an increase in the critical resolved shear stress. He reports that the change in the rate of strain hardening with log strain rate $[d(d\sigma/d\epsilon)/(d \log \dot{\epsilon})]$ is independent of temperature for NaCl, LiF, and MgO.

Strain hardening is essentially linear for ionic crystals, as can be observed from the stress-strain curves presented by Luhman and Gorum[37] (AgCl), and Gorum, Parker, and Pask[7] (KCl, KBr, MgO).

In general, a temperature increase would increase the ease of dislocation motion and thus decrease the yield strength. For NaCl, LiF, and MgO, Phillips[39] reports the following relationships

$$\sigma_c = \sigma_o e^{-KT} \qquad (1)$$

where σ_c is the critical resolved shear stress, σ_o is a stress constant, K is a constant (for constant strain rate), and T is the absolute temperature. A break in the log σ_c vs. absolute temperature plot occurs at approximately 300°K for NaCl, 420°K for LiF, and 440°K for MgO. Above these characteristic temperatures, there is a decrease in the rate of change of log σ_c/T.

Pratt[40] points out that dislocations in an ionic crystal should be charged (have an excess of jogs of one sign). Eshelby, et al.[41] suggest that vacancies formed in an ionic crystal will form a charge cloud around a dislocation which will lock the dislocation in place. They point out that the addition of divalent impurities to NaCl would cause maxima and minima to be expected in the yield strength vs. temperature plot. Maxima and minima were observed by Ekstein[42] and Eshelby, et al.[41] The dislocation locking effect resulting from divalent impurities could account for the previously noted greater yield strength increase for divalent vs. monovalent solute additions.

Westbrook[43] reports that the yield stress is given approximately by the following equation for NaCl type ionic solids

$$Y.S. = H_v/35 \qquad (2)$$

where Y.S. is the yield stress in Kg/mm^2 and H_V is the Vickers hardness in Kg/mm^2. Gilman[17] shows that there is a linear relationship between elastic modulus and microhardness for NaCl type ionic solids. The linear yield stress-hardness relationship would be expected since the theoretical stress required to move a dislocation is proportional to the elastic modulus.[44]

b. Surface Effects-The surface conditions of ionic crystals often limit plastic behavior by causing premature fracture, as will be discussed in the next section. However, surface conditions do not have a strong effect on the fundamental event in plasticity: the mobility of dislocations.[19] Vaughan and Davisson[45] show that the stress required to move dislocations in a given NaCl crystal is independent of exposure to air, water, oil, and air aging.

The surface is important as a source of "fresh" dislocations as pointed out in the previous section and as discussed by Stokes.[32]

Because the number of dislocation sources in the surface control the distribution of glide, they also control the rate of strain hardening. As the number of interfering glide bands increases, the rate of strain hardening increases. The influence of the surface on the rate of strain hardening of MgO was demonstrated by Stokes.[32]

4. Fracture of Ionic Solids

Fracture of ionic solids often occurs at stress levels lower than those required for appreciable plastic flow. In this section the factors influencing fracture will be considered under the following

headings:

a. Surface Effects.

b. Plastic Flow Effects.

c. Stress State Effects.

a. Surface Effects-For all NaCl type ionic solids, ductility is limited by the presence of surface micro-cracks. These micro-cracks can be introduced by conventional sample preparation techniques such as cleavage, or sawing, grinding, and wet polishing.(46-48) Stokes, Johnston, and Li(47) have recently shown that surface defects can readily be introduced into polished ionic crystals by conventional handling techniques. Clarke and Sambell(45) report that chemical polishing will remove cleavage micro-cracks and enhance the ductility of MgO crystals 5 to 10 times. Considering the susceptability of ionic crystals to surface damage and the marked effect of this damage on their ductility, it is not surprising that much conflicting data exist in the literature.

Special surface effects have been observed in the water soluble ionic salts such as KCl, KBr, and NaCl.(7) Freshly cleaved and/or water polished samples of these materials are ductile.(49) However, authors(49-51) have reported a loss of ductility with aging in air. The air aging effects are less or nonexistent for LiF and MgO.(7) Murray has shown that air aging raises the ductile-brittle transition temperature for NaCl and MgO.(52) Gorum, Parker, and Pask(7) report that the air embrittlement is caused by oxygen and nitrogen. Aerts and Dekeyser(50) report that nitrogen diffuses into NaCl, pins the dislocations, hardens the material, and leads to premature failure. Class, Machlin, and Murray(51) have found that the surface of NaCl reacts with ozone in the atmosphere to form $NaClO_3$.

Three different mechanisms have been proposed for the air embrittlement phenomenon:

1. For a crystal containing flaws, gas absorption will result in a lowering of the critical stress for crack propagation according to the Griffith equation. This would cause a deterioration of the mechanical properties.[47]
2. A surface layer is formed which is difficult for the dislocations to penetrate.[7,53] The dislocations pile up against this surface layer and nucleate a crack.
3. The $NaClO_3$ layer forms a brittle coherent surface film which can start cracks in the underlying crystal.[51]

A fourth mechanism might also be considered. The gases tend to pin "fresh" dislocations at the surface, decreasing the number of active slip systems. This would lead to fracture at interacting slip planes as discussed in the next section.

Stokes, Johnston, and Li[47] have demonstrated that surface precipitates formed on improperly dried NaCl crystals lead to premature failure. They have also shown that air embrittlement is slowed down markedly if the crystals are stored in a desicator. Moisture in the air could cause local salt solution and reprecipitation and thus speed up the embrittlement phenomenon.

The role of gases in air embrittlement phenomena is an area deserving more study for clarification. The major effect of chemical polishing is probably the removal of surface defects, such as microcracks.

b. Plastic Flow Effects-Cracks can be nucleated in ionic crystals by the pile-up of dislocations against an obstacle.[54-58] Three types of crack nucleation mechanisms have been observed in MgO. Stokes, Johnston, and Li[54,55] report crack formation associated with the Stroh mechanism.[59] In their compression samples, dislocations were observed to pile up at a kink band and nucleate a crack. Washburn, Gorum, and Parker[56] observed crack nucleation associated with the Cottrell mechanism.[60] They observed this type of crack formation in tension samples. Dislocation pile up on two intersecting (110) slip bands leads to crack nucleation along a (100) plane. Keh, Li, and Chou[57] proposed a third type of mechanism to account for (110) crack formation around hardness indentations in LiF and MgO. For their mechanism, an immobile dislocation is formed in a (112) plane having the vector $1/2a[1\bar{1}0]$. Dislocations generated on the two intersecting slip planes (011) and (101) will pile up against this immobile dislocation and initiate a crack in the $(1\bar{1}0)$ plane.

The significance of these mechanisms and observations is that they show cracks can be nucleated as a result of plastic flow. These crack nuclei can lead to catastrophic failure.

Melankholin and Regel[61] studied crack formation and propagation in NaCl. They observed that cracks often stop in regions of local plastic hardening. This observation is substantiated by the later observations of Stokes, Johnston, and Li.[58]

Stokes, Johnston, and Li[58] state that the amount of plastic deformation preceding cleavage fracture depends on the density and distribution of slip sources at the onset of plastic flow. Their reasoning

follows. A cleavage crack is nucleated at the end of a $(\bar{1}10)$ slip band by the coalescence of edge dislocations, which are held up by an orthogonal intersecting (110) slip band. The crack nucleus propagates parallel to the (110) plane until halted by another $(\bar{1}10)$ slip band parallel to the original $(\bar{1}10)$ slip band. The $(\bar{1}10)$ slip band prevents the crack from propagating further in the $[\bar{1}10]$ direction, but it is free to develop parallel to the [001] line of intersection. For fracture, the slit transfers to the (100) plane normal to the applied stress. The effectiveness of the adjacent $(\bar{1}10)$ band in halting and stabilizing the crack nucleus is a function of its distance from the [001] line of nucleation. This distance determines the crack velocity when it hits the slip band and the stabilized crack length, which in turn determines its associated stress concentration.

If all slip bands are parallel, high plastic deformation can occur. If a high number of intersection slip bands are present, the cracks are stabilized and high ductility occurs. This mechanism effectively explains the high ductility observed for crystals whose surfaces were sprinkled with hard powders.

c. Stress State Effects-The ability of an ionic material to be plastically deformed is dependent on the stress state. Bridgman[62] has shown that the introduction of large hydrostatic pressures markedly increases the ductility of metals. Bridgman[63] has also shown that the strength and ductility of NaCl and Al_2O_3 are increased by the application of hydrostatic pressure. Hydrostatic pressures plus superimposed shear stresses would also account for the plastic deformation occurring naturally in rock strata.[13,64]

Scheil[8] states that MnS inclusions within a steel deform plastically when the steel is deformed while inclusions fracture in a polished surface. He suggests that cleavability is suppressed by imbedding the inclusions in a metal matrix.

Pask[18] states that hydrostatic pressures tend to eliminate pure tensile stresses, allowing the development of sufficiently high shear stresses to cause plastic deformation.

B. Deformation of Included Nonmetallic Phases

The type, size, shape, and distribution of nonmetallic inclusions can have a marked effect on the properties of a metal. In free-machining steels, for example, sulfur is intentionally added to improve machinability.[65] Knowlton[66] and Boulger, et al.[67] have observed that steels containing globular sulfide inclusions had higher machinability indices. Inclusions have a detrimental effect on fatigue properties,[68-74] ductility,[75-77] and impact strength.[78] Cummings, et al.[68] and Ransom[72] show that inclusion size and shape have a marked effect on fatigue properties while Gagnebin[75] and Ogawa, et al.[77] show that globular, randomly distributed inclusions are a requirement for high ductility.

The size, shape and distribution of inclusions in metals can be controlled to some extent by forming operations. Pickering[79] suggests that inclusion fracture during deformation is necessary to disperse larger detrimental inclusions into smaller, less harmful particles. Proper selection of deformation parameters which favor spherical sulfide inclusions is important to producers of free-machining steels.

Consequently, parameters affecting inclusion deformation and/or fracture and dispersion during metal forming operations are important.

No systematic study has been made of the effects of deformation parameters on the deformation and fracture of included nonmetallic phases. The material that follows will illustrate the types of studies that have been made.

In 1935, Scheil and Schnell[80] showed qualitatively that different types of inclusions in steel behave differently during deformation. Dehlinger[81] observed the deformation of FeS, NiS, Cu_2S, Ag_2S, and Cu_2Se inclusions in their base metal. The inclusions were found to deform readily. Dehlinger[81] suggested that all sulfides, selenides, and telurides should be expected to deform readily in their base metal. For MnS, Cu_2S, and Ag_2S in their base metals, Scheil[8] reported the sulfide length/width (L/W) ratio is approximately equal to the square root of the metal L/W ratio.

Van Vlack[82] studied the effects of composition and mechanical working on the L/W ratio of inclusions in resulphurized steels. He found that fracture and diminuition in the size of sulfide inclusions becomes pronounced on cold working. Deoxidizers, such as silicon and aluminum, were found to increase the plasticity of sulfide inclusions during hot rolling.

More recently, Van Vlack, et al.[1] studied the effects of steel composition and temperature on the equilibrium shape, and type of sulfide and sulfide-oxide inclusions. MnS deformation was known to increase with increasing silicon content in the steel.[82] A siliceous liquid was found to envelop the MnS inclusions with higher silicon levels in the

steel. It was postulated that this liquid would facilitate the development of hydrostatic pressures on the MnS inclusions. MnS deformation would be facilitated by hydrostatic pressures rather than single shear stresses.

Scheil[8] and Pickering[79] studied the effects of inclusion size on deformation. Scheil[8] reports the L/W ratios of Cu_2S inclusions in Cu were statistically independent of their size. Pickering[79] states that small inclusions deform less readily than large ones. Pickering also states that larger inclusions fracture earlier. The probability of fracture increases with increasing deformation.

Scheil[8] and Pickering[79] studied the effects of temperature on the deformation of inclusions in steel. For a 0.23% S steel, Scheil[8] found no change in sulfide deformation in the temperature range from -80 to 1250°C. However, the scatter in his data was large. For silicate inclusions, he found low deformation at 700°C. At 900°C, the amount of inclusion deformation approaches that of the steel. Only slight deformation increases were observed above 900°C. Except for a 100°C difference in the brittle-ductile transition, Pickering's[79] silicate curve has the same shape. Pickering[79] found the silicates were brittle below 1000°C. He found that iron oxide inclusions become increasingly plastic as the rolling temperature decreases from 1150 to 800°C.

Scheil and Sibert[83] made a statistical study of the extent to which needle-like brittle inclusions, such as FeAl and Si, in Al are broken on rolling. FeAl was found to be more brittle than Si, except at 400°C where they were about the same.

Puttick[84] studied the deformation and fracture of pearlite. He observed plastic deformation of cementite lamellae in pearlite. The following sequence of events was found during deformation:

1. Fine slip in ferrite near pearlite grains.
2. Large shear deformation of ferrite.
3. Eventual fracture of ferrite and pearlite in regions of heavy deformation.

Gurland[85] and Nishimatsu and Gurland[86] studied the deformation of two-phase alloys of tungsten carbide and cobalt. WC ($94R_A$) is considered to be a rigid, brittle inclusion in the Cobalt ($42R_A$) matrix. The samples deform by plastic flow in the matrix. At stress levels approaching those required for sample fracture, fracture of WC grains is observed. In a 50 WC - 50 Co sample, slip lines were observed to pass through a few WC grains. Thermal history can create stress concentrations in the sample. Consequently, slip is observed with lower loads as the WC content increases.

C. Hardness and Yield Strength

In extrusion theories, ram pressure is linearly proportional to the average yield strength of the samples. Thus, the experimental data yield indirect evidence on the effects of sample variations on the average yield strength. A brief discussion of trends which can be predicted from the literature will be presented in this section.

Indentation hardness is influenced by yield strength and rate of strain hardening. Hill[87] states that the indentation force per unit area is three times the yield stress for a spherical indentor.

Westbrook[43] has shown a linear hardness-yield strength relationship for face-centered cubic metals and NaCl-type ionic solids. Hardness and yield strength will be considered simultaneously, since a factor which increases hardness will also increase average yield strength.

In general, hardnesses and yield strengths of two-phase materials are structure sensitive. These properties are influenced by the size, shape, and distribution of the second phase. Generally, the yield strength would not be expected to follow a simple law of mixtures rule

$$\sigma_{sample} = \sigma_a f_a + \sigma_b f_b \qquad (3)$$

where σ is the yield strength and f is the volume fraction of the phase indicated by the subscripts.

Edelson and Baldwin[88] have demonstrated that the second phase must be harder than the matrix for hardening to occur. Edelson and Baldwin[88] and Geisler[89] demonstrated that the second phase must be coherent with the matrix for the occurrence of major yield strength increases. Particle strenghtening would not be expected when the included phase is weaker than the matrix.

Edelson and Baldwin[88] and Geisler[89] suggest that the yield strength increase is a function of the mean free path between particles. For Cu-Cr and Cu-Fe systems, where the second phase is coherent, the yield strength increases for mean free paths below approximately 1270μ. For WC-Co alloys, where the phases are not coherent, the yield strength does not increase significantly until the mean free path is below 10μ.[86] For noncoherent phases, particle strengthening would not be expected unless the mean free path was very small.

Koppenaal and Parikh[90] and Keeler[91] show that the stress required to initiate slip in the matrix is largely independent of the amount of a harder, included phase. This stress is the stress required to start dislocation motion in the weakest phase. Since the phases have different expansion coefficients, thermal history can create residual stress fields in the sample which can modify the applied stress required to initiate yield. This effect is minimized as the inclusion spacing is increased.

Koppenaal and Parikh[90] and Keeler[91] show data where the second phase has a marked effect on the rate of strain hardening of the matrix. As the amount of a hard second phase increases, matrix strain hardening increases rapidly. Thus, for moderate strains, the yield strength is influenced significantly by the amount of the second phase.

To date, no general theory exists for predicting the yield strength of two-phase samples for a broad range of sample variations.

D. Extrusion

The extrusion literature will be considered under the following headings:

1. Extrusion Methods.
2. Extrusion Pressure Curves.
3. Flow Patterns During Extrusion.
4. Extrusion Theories.
5. Factors Controlling Ram Pressure and Stress State.

For more general reviews, the reader is referred to Pearson and Parkin's book on extrusion,[92] Bishop's recent review on the theory of extrusion,[93] and Wistreich's review on wire drawing.[94]

1. Extrusion Methods

Extrusion can be accomplished by either the direct or the indirect method (Figure 1). In direct extrusion, the billet is pushed down the chamber and through the die. For indirect extrusion, the billet is stationary while the die moves. Lower ram pressures are required for indirect extrusion since sliding friction between the billet and the chamber wall does not have to be overcome. However, the reduced ram cross-sectional area for indirect extrusion often limits the application of this method.

There are a number of extrusion variables which can be readily studied, i.e.:

1. Per cent reduction in billet area.
2. Die angle.
3. Ram velocity.
4. Temperature of extrusion.
5. Coefficients of friction along the die and chamber walls.
6. Sample type.

2. Extrusion Pressure Curves

Ram pressure-ram displacement curves are shown in Figure 2. The ram displacement at point RP corresponds to the ram contacting the die lip. A hollow conical "pipe" forms at the ram end of the billet. This hollow "pipe" collapses readily when it enters the die resulting in the dip at the end of the ram pressure-ram travel curve. The linear decrease in ram pressure with increasing ram travel represents a decrease in the contact area between the billet and the chamber wall. As

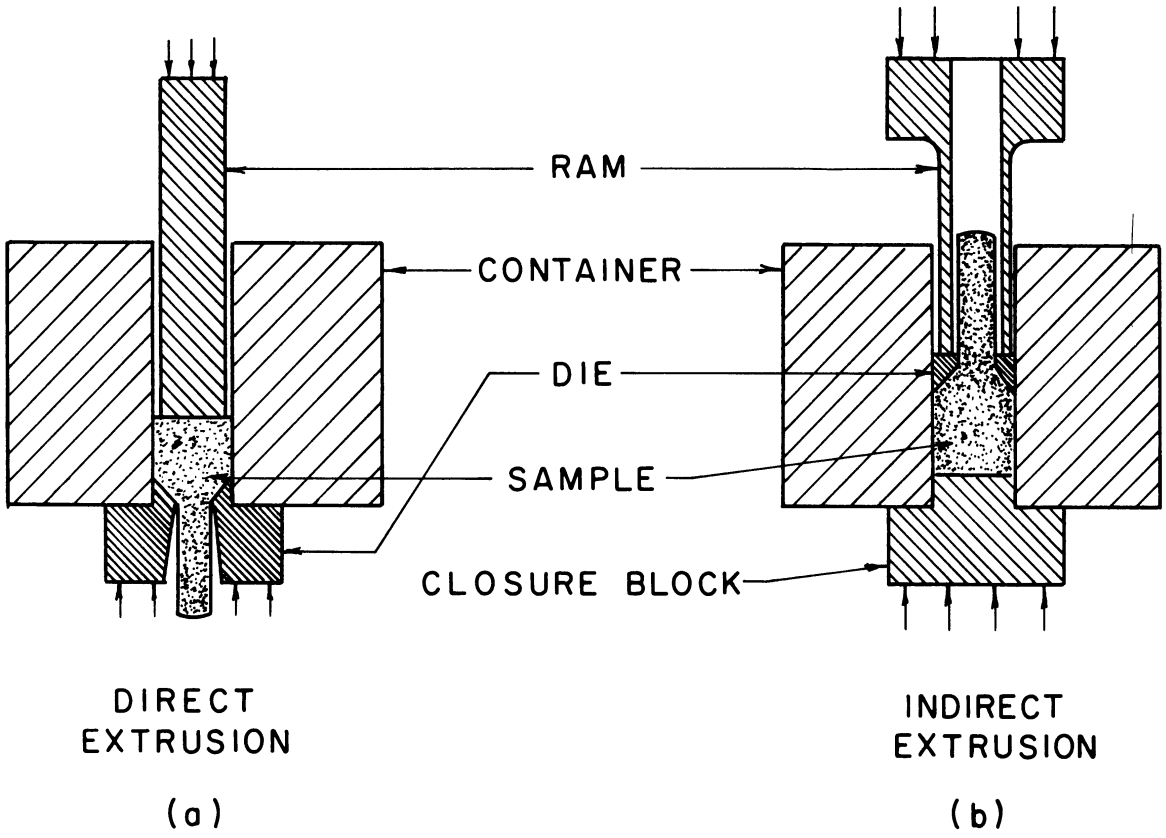

Figure 1. Direct and Indirect Extrusion Equipment.

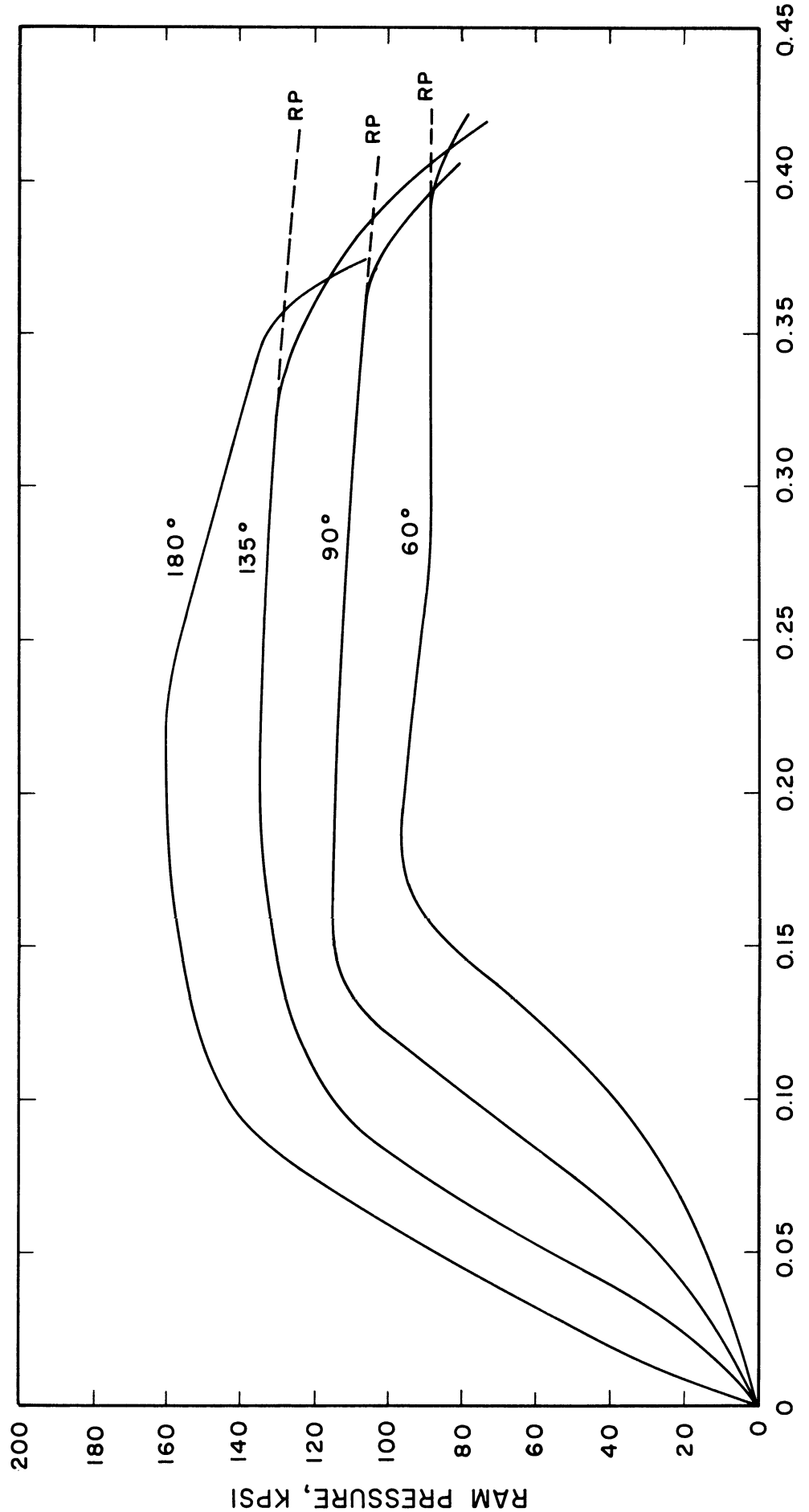

Figure 2. Ram Pressure versus Ram Displacement. 75 per cent reduction dies, having the indicated die angle, were used.

the frictional forces associated with this area decrease, the ram pressure decreases.

3. Flow Patterns During Extrusion

The literature on flow patterns during extrusion is summarized by Pearson and Parkins.(92)

Sachs and Eisbein(95) show the effects of die cone angle on the flow distribution for tin samples. The flow patterns were obtained by observing the deformation of a grid inscribed on a plane of symmetry. As the die cone angle decreases, the amount of grid distortion decreases. The amount of grid distortion increases as the sample surface is approached. With small die angles, there is a fairly close approximation to uniform deformation by simple elongation.

For large die angles and strain-hardening materials, dead metal zones are observed at the die-container junction.(96) Under these conditions, the sample forms its own die surface.

A number of extrusion theories assume that the material in the die flows radially toward the virtual apex of the die (Point O in Figure 3(a)). Examination of the pictures of gridded samples presented by Sachs and Eisbein(95) indicate that this is a reasonably good approximation for small die angles. However, for large die angles the lines become curved as shown schematically in Figure 3(b).

The use of lubricants decreases the shear distortion near the sample surface.(92)

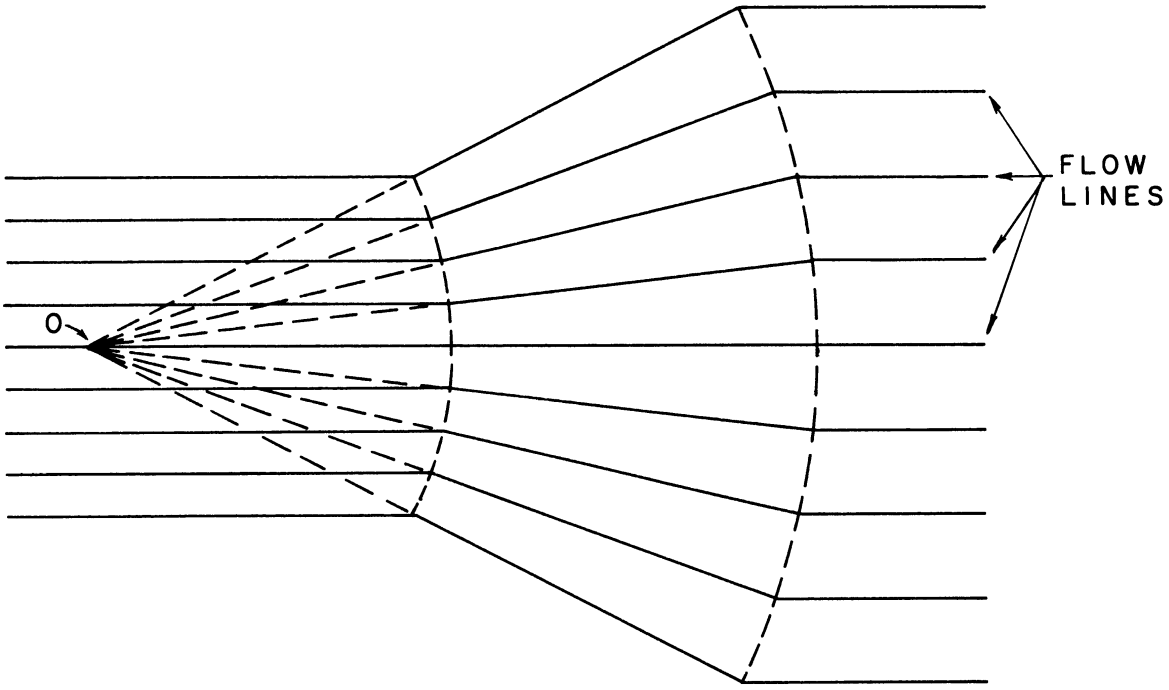

a) Flow pattern assumed by a number of extrusion theories

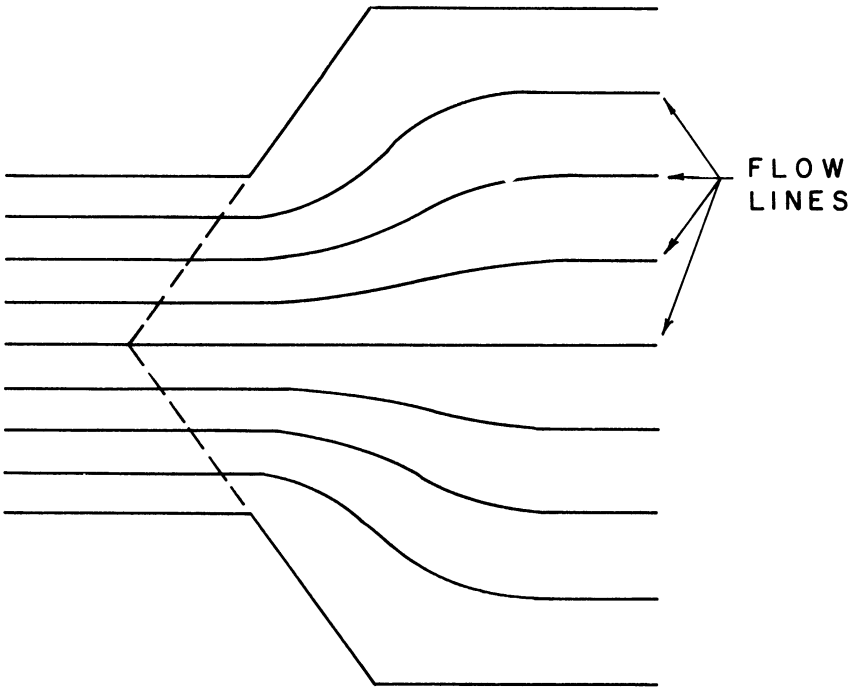

b) Flow pattern for large die angles. This figures is based on results presented by Sachs and Eisbein[95] for gridded tin sample.

Figure 3. Schematic Flow Patterns for Extrusion.

4. Extrusion Theories

An ideal extrusion theory would allow the prediction of the optimum combination of process variables for minimizing ram pressure and maximizing product quality. However, a rigorous solution to the apparently simple problem of the extrusion of a cylindrical billet into a cylindrical rod is not known for the process variables, even under highly idealized conditions.(93) The extrusion theories presented in the literature are for "simplified" cases of the practical problems. Solutions to actual problems are limited by the complexity of the mathematics involved and in some cases, by knowledge of the metallurgy involved. The solutions to many of these "simplified" problems are difficult to handle. They do represent a real advance toward the understanding of the extrusion process.

Most extrusion theories simplify the problem by considering isotropic, incompressible, non-strain hardening materials. They do not consider the elastic stress components present in the material, nor in general, the stress required to change the direction of material flow at the die entrance and exit sections. Many of the solutions are for the plane strain rather than the more common axially symmetric case. For plane strain, the stress and velocity equations are hyperbolic equations and can thus be treated by known mathematical methods. The balance of this section will be devoted to various analytical and empirical extrusion theories. Since ram pressure is used as an indication of stress state in the thesis, ram pressure-process variable relationships will be presented for the various theories.

a. Homogeneous Deformation-For homogeneous deformation only the work required to change the shape of the material is considered. This derivation does not consider the work required for redundant deformation or for overcoming frictional forces. In 1874, Fink[97] deduced the work required to deform a plastic material from observations on the rolling of metals. Siebel and Fangemeier[98] applied the same approach to calculate the ram pressure (RP) required for extruding a cylindrical rod from a cylindrical billet. They obtained the equation

$$RP = \sigma_o \log_e \left(\frac{A_i}{A_f}\right) \tag{4}$$

where σ_o is the tensile yield strength of the material, A_i is the initial cross-sectional area, and A_f is the final cross-sectional area. Observed extrusion pressures are approximately 45 per cent greater than those calculated from Equation (4).

b. Plane Strain Extrusion Without Friction-Hoffman and Sachs[99] present a derivation of extrusion stresses for the frictionless case. The stress components are indicated in Figure 4(a) where σ_R and σ_φ are the principal stresses. It is a plane strain solution. The pertinent equations are

$$\sigma_R = \sigma_o \log_e \left(\frac{D_f^2}{D^2}\right) \tag{5}$$

$$\sigma_\varphi = \sigma_o \left[\log_e \left(\frac{D_f^2}{D^2}\right) - 1\right] \tag{6}$$

$$RP = \sigma_o \log_e \left(\frac{D_f^2}{D_i^2}\right) \tag{7}$$

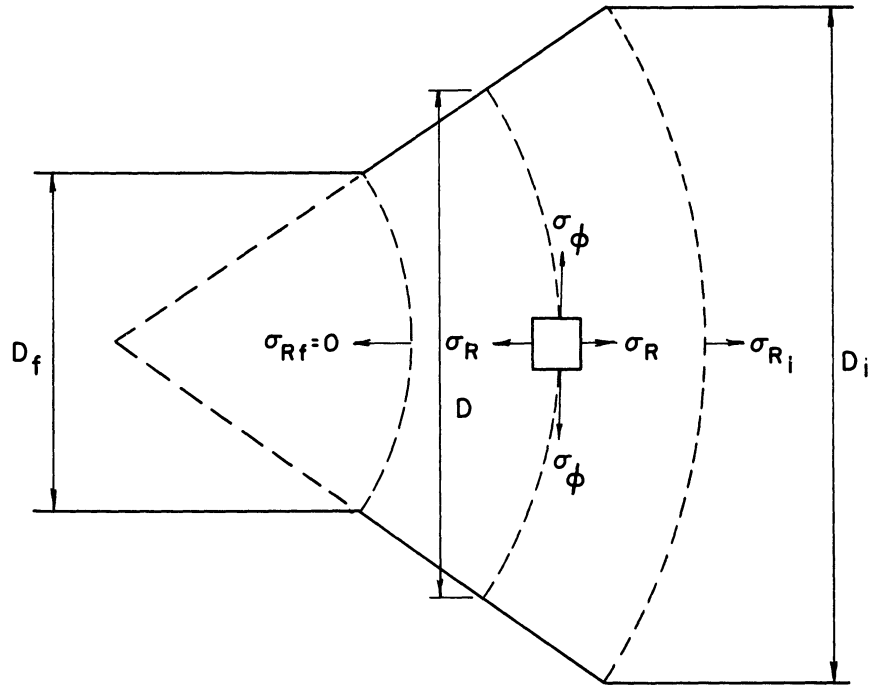

a) Plane strain extrusion without friction.

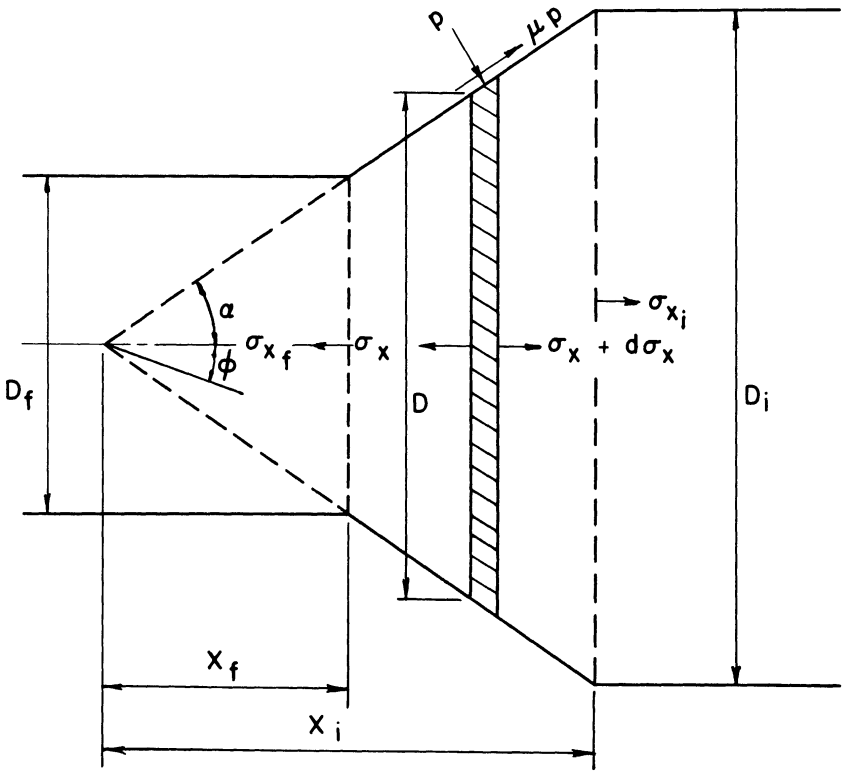

b) Plane strain extrusion with friction.

Figure 4. Dimensions for Extruding a Cylindrical Body.

Note that the principal stress components are independent of the distance of an element from the center line. This would not be expected to be the case. Equation (7) is the same as Equation (4).

c. Plane Strain Extrusion with Friction-Hoffman and Sachs[99] present a derivation of stress fields for the extrusion of a cylindrical billet with friction between the billet and the die wall. A plane strain analysis is used to determine the stress components shown in Figure 4(b). The resulting equations are

$$\frac{\sigma_x}{\sigma_o} = \frac{1+B}{B}\left[1-\left(\frac{D}{D_f}\right)^{2B}\right] + \frac{\sigma_{xf}}{\sigma_o}\left(\frac{D}{D_f}\right)^{2B} \tag{8}$$

$$\frac{p}{\sigma_o} = \frac{1}{B}\left[1+(1+B)\left(\frac{D}{D_f}\right)^{2B}\right] - \frac{\sigma_{xf}}{\sigma_o}\left(\frac{D}{D_f}\right)^{2B} \tag{9}$$

$$\frac{RP}{\sigma_o} = \frac{1+B}{B}\left[1-\left(\frac{D_i}{D_f}\right)^{2B}\right] + \frac{\sigma_{xf}}{\sigma_o}\left(\frac{D_i}{D_f}\right)^{2B} \tag{10}$$

where

$$B = \frac{\mu}{\tan\alpha} \tag{11}$$

μ is the coefficient of friction, and σ_{xf} represents the pressure applied to the rod leaving the die. In general, σ_{xf} would be set equal to zero and the last term in the Equations (8) through (11) would drop out. Treco[100] has recently extended this analysis to allow for friction at the chamber wall and at the die exit.

The problem in applying the above equations lies in determining the value of the coefficient of friction. The coefficients of friction

are often empirical constants which are used to make the equations fit experimental data. Treco[100] has shown that a reasonable estimate of the coefficient of friction for his extended analysis will lead to maximum calculated ram pressure values within seven per cent of those obtained experimentally.

d. Slip Line Theories-Luders lines develop in annealed mild steel which is deformed slightly beyond the yield point. The Luders lines are lines of maximum shear stress along which there is relative movement of the adjacent material. The Luders lines intersect each other at 90°. The slip line deformation theory is based on the development of Luders lines. For a given deformation process, a slip line field is assumed which is composed of the so-called α and β lines which are orthogonal. Stress and velocity equations are then developed for the assumed slip line field. The solutions are developed for plane strain since the mathematics of the situation become too complex when a third strain direction is introduced.

The laws governing the properties of slip line fields were developed by Hencky[101] (stress equations) and Geiringer[102] (velocity equations). Methods of application of slip line theory are discussed by Hill[87] and by Prager and Hodge.[103] Hill[104] first applied slip line theory to extrusion in 1948. Johnson[105-107] has applied the method to direct extrusion for a variety of die cone angles, reductions, and coefficients of friction.

For all slip line solutions, the ram pressure is equal to the average tensile yield strength times a function which considers the die

geometry and frictional conditions. As an example, for 50 per cent reduction in diameter and a square die, Hill[104] proposes the slip line field shown in Figure 5. The ram pressure is given by the following equation

$$RP = k\left(1 + \frac{\pi}{2}\right) \qquad (12)$$

where $k = \sigma_o/\sqrt{3}$ for the Mises yield condition or $\sigma_o/2$ for the Tresca yield condition.

Purchase and Tupper[108] have shown that there is good agreement between the experimental and calculated flow pattern for an inscribed square grid. The theoretical solution for 50 per cent reduction in thickness and a square die was compared with the flow pattern obtained for gridded lead using a square die and 46.7 per cent reduction.

Johnson[109] conducted a series of experiments using different materials, reductions, and friction conditions in an examination of extrusion pressure. His conclusions give a fair summary of slip line theory. They are listed below:

1. Lubricated extrusions are accompanied by coefficients of friction which are not small.
2. In the case of lubricated slip over the die face, which occurs for die semi-angles up to about 60°, pressures can be reasonably well predicted if a high value of μ is assumed.
3. With large angle or square dies, pressures will be predicted to better than about 15 per cent by the curves

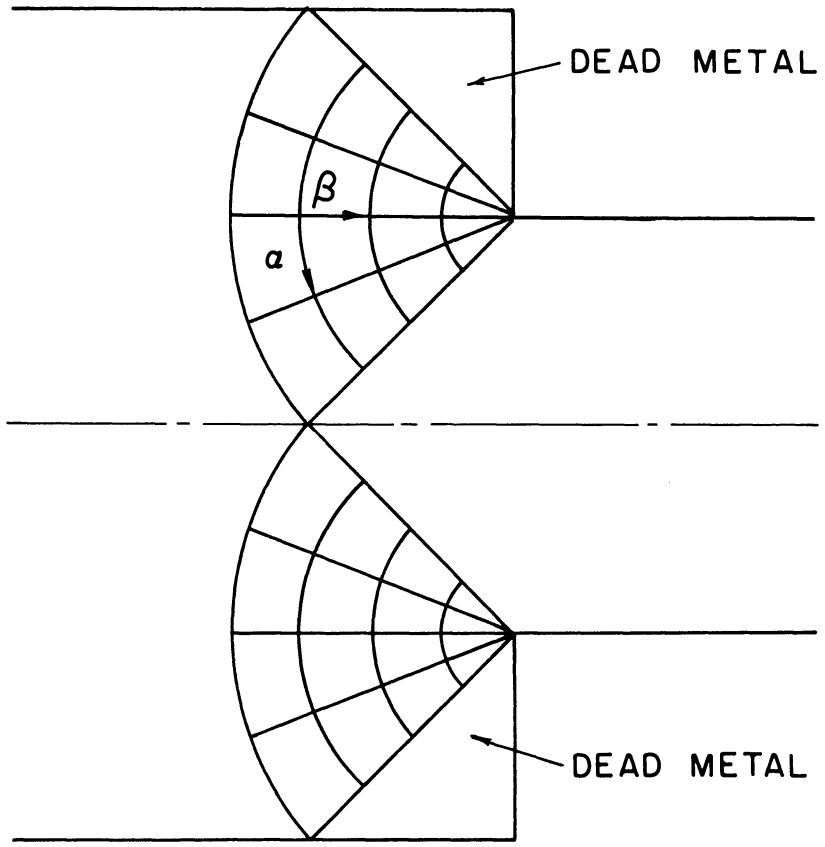

Figure 5. Slip Line Field for 50 Per Cent Reduction in Thickness and a 180° Die.

associated with the dead metal zone hypothesis and a rough container wall.

4. The method of allowing for strain hardening by using an averaged value of the yield stress is quite satisfactory for practical purposes.

5. Distorted grids, as predicted by the thoery, though not exact, certainly provide very good first approximations.

Dodeja and Johnson[110] suggest that the values k and σ_o be replaced by the average values $\bar{k}$ and $\bar{\sigma}_o$ for a strain hardening material. These average values could be obtained from a true stress-strain diagram. $\bar{\sigma}_o$ would represent the average value of true stress over the strain range of interest. In conclusion (4) above, Johnson shows that the average value works quite well for computing ram pressure. However, $\bar{\sigma}_o$ would not yield an accurate value for the stress state at various points in the material. Stresses near the die exit would be higher than the values calculated using $\bar{\sigma}_o$. The converse would be true near the entrance section of the die.

e. Axially Symmetric Extrusion-Shield[111] presents an analysis for the axisymmetric case of flow through a converging conical channel. This stress analysis method will be considered in detail in the thesis. The directions of the nonzero principal stress components are given in Figure 6. The ram pressure and the principal stress components are given by the following equations for the von Mises yield condition

$$RP = \frac{\sigma_o}{\sqrt{3}} C \log_e \left(\frac{D_i}{D_f} \right) \qquad (13)$$

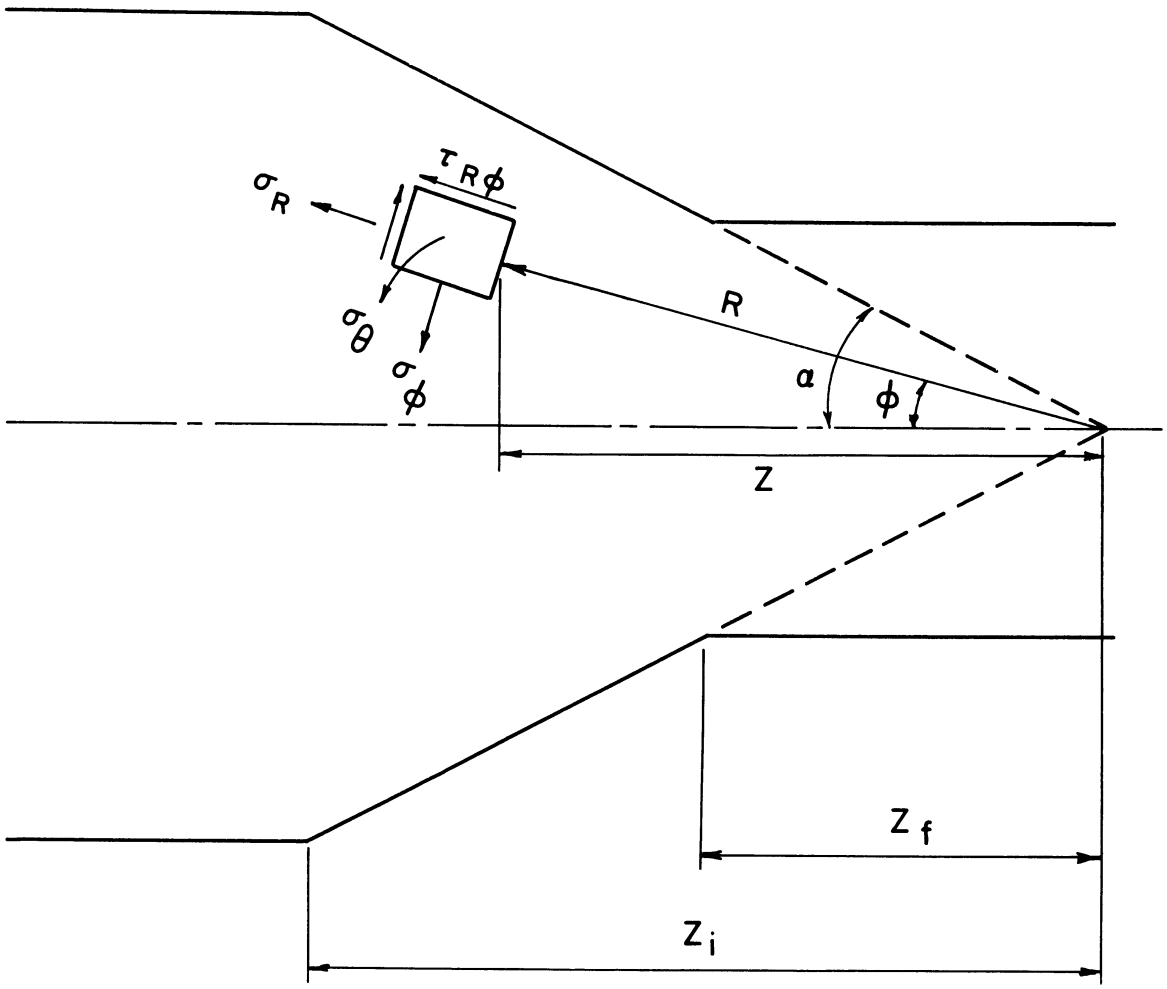

Figure 6. Dimensions for the Axially Symmetric Extrusion of a Cylindrical Body.

$$\tau_{R\varphi} = \frac{\sigma_o}{\sqrt{3}}\tau \tag{14}$$

$$\sigma_\varphi = \sigma_\theta = \frac{\sigma_o}{\sqrt{3}}\left[g(R) - 3\int \tau d\varphi\right] \tag{15}$$

$$\sigma_R = \sigma_\theta + \sigma_o\sqrt{1-\tau^2} \tag{16}$$

where τ is $(\tau = f(\varphi))$ obtained from the equation

$$\tau'(\varphi) + \tau\cot\varphi + 2\sqrt{3(1-\tau^2)} = C \tag{17}$$

and

$$g(R) = -C\log_e R + A \tag{18}$$

A and C are constants of integration to be determined from the boundary conditions. The mathematical complexity of the "simplified" axisymmetric model considered here is readily apparent.

f. Stress Determination from Gridded Specimens-Thomsen and coworkers[112-116] have experimentally determined stress and velocity fields for extrusion. A grid is inscribed on a plane of symmetry through the sample and the sample is then extruded incrementally. After each deformation increment, the grid shape is photographed. The velocity field is found directly by analysis of the deformed grids while the stress field is determined from the experimentally determined velocity field.

g. Empirical Formulas for Extrusion Pressure-Johnson[107] states that ram pressure curves calculated from plane strain theory can be expressed empirically in the form

$$\frac{RP}{2k} = a + b\log_e\left[\frac{1}{1-r}\right] \tag{19}$$

where $\underline{r}$ is the reduction and $\underline{a}$ and $\underline{b}$ are constants. Since

$$r = \frac{A_i - A_f}{A_i} \tag{20}$$

Equation (19) can also be stated as

$$\frac{RP}{2k} = a + b \log_e \left(\frac{A_i}{A_f}\right) \tag{21}$$

Bishop[93] summarizes values of $\underline{a}$ and $\underline{b}$ to be used for various frictional conditions and reductions.

For lead, Johnson[117] found $a = 0.8$ and $b = 1.5$. For lead, tin, and super-pure aluminum, he demonstrates that the use of these constants in Equation (17) leads to values of $RP/2\bar{k}$ which are within seven per cent of experimental $RP/2\bar{k}$ values. Reductions between 75 and 93.8 per cent were used with square dies.

5. Factors Controlling Ram Pressure and Stress States

In this section, the effects of extrusion variables on ram pressure will be considered. A variable which increases the ram pressure will increase the stress levels in the sample.

a. Per Cent Reduction-As shown in the previous section, experimental data would be expected to fit Equation (21). Consequently, a linear relationship would be expected between ram pressure and $\log_e(A_i/A_f)$.

b. Die Angle-The flow patterns presented by Sachs and Eisbein[95] show that more uniform deformation is achieved as the die angle decreases. With more uniform deformation, the amount of redundant work would decrease, and the extrusion pressure would decrease. However, for a given

reduction, as the die angle decreases, the area of contact between the billet and die wall increases. As this area increases, the ram pressure would be expected to increase for a fixed coefficient of friction. For a fixed die angle, the contact area increases with increasing reductions. These counteracting effects explain the die cone angle effect discrepancies which are reported in the literature. For a fixed reduction, there is some optimum die angle. As the reduction increases, the optimum angle would be expected to increase.

Johnson[106] shows this ram pressure minimum using plane strain theory. For a reduction of 20 per cent and a coefficient of friction of 0.20, the ram pressure minimum occurs for a die semi-angle of 17°.

c. Sample Variations-For the extrusion theories, changes in the sample material are accounted for by yield strength changes. The theories presume a linear relationship between ram pressure and average yield strength. The results obtained with empirical formulas indicate that this is a good first assumption.

d. Temperature-For the various extrusion theories, temperature effects would be accounted for in the yield strength term. As the temperature increases, the yield strength and ram pressure would be expected to decrease. Schishokin[118] presents the following empirical formula for use where temperature is the only variable

$$RP = A e^{-\lambda T} \tag{22}$$

where A and λ are constants and T is the extrusion temperature. This formula would only be expected to be valid for the hot working

temperature range. For Equation (20) to be valid, the following yield strength relationship would have to be valid

$$\sigma_o = B e^{-\lambda T} \tag{23}$$

where B and λ are constants and T is the temperature.

e. Extrusion Speed-Pearson and Parkins[92] present experimental data for the effects of extrusion speed on ram pressure. Cadmium and lead were the experimental materials. The following equations fit the experimental data

$$V = b(RP)^a \tag{24}$$

or

$$\log_e(RP) = \frac{(\log_e V + \log_e C)}{a} \tag{25}$$

where V is the extrusion speed and a, b and c are constants. As the extrusion speed increases, the ram pressure would be expected to increase.

CHAPTER III

EXPERIMENTAL PROCEDURE

The following areas were investigated experimentally:

1. The effects of extrusion parameters and sample variations on inclusion deformation.
2. Strain hardening of copper during extrusion.
3. Hardnesses of pure inclusion materials.
4. Matrix and inclusion hardnesses in as-sintered and as-extruded samples.
5. Hot hardness of sodium chloride.
6. Compressive yield strength as a function of matrix hardness.

Experimental procedures used for the various studies will be discussed under the headings:

A. Sample Preparation.

B. Test Methods.

The procedures used for inclusion deformation analysis will be discussed in Chapter IV. The methods used to treat hardness data are described in this chapter.

A. Sample Preparation

Sample preparation techniques will be considered under the following headings, which describe the sample type:

1. Extrusion Samples.
2. Strain Hardening Samples
3. Inclusion Hardness Samples.

4. NaCl Hardness Samples.

5. Compressive Yield Strength Samples.

1. Extrusion Samples

Standard powder metallurgical techniques were used to prepare the extrusion samples.

a. Sample Materials-Face-centered cubic metals (Pb, Al, Ag, Cu, and 65-35 brass) were used as matrix materials and ionic solids having the NaCl structure (KCl, NaCl, LiF, and NaF) were used as inclusions. The sample types and deformation parameters studied are listed in Table I. High purity aluminum and brass powders were used while all other materials were reagent grade.

The as-received KCl, NaF, and LiF powders were too fine for inclusion use. To produce coarser particles, each inclusion material was held at a temperature 50°F above its melting point for 1/2 hour in graphite crucibles and then furnace cooled. This procedure produced coarse-grained ingots having a grain diameter of approximately 1/4 to 3/8 inch. Each ingot was crushed and screened to produce inclusions in the desired size range.

b. Powder Metallurgical Treatment-Granular silver and lead shot, having a size range of -40 +120 mesh, were used. All other metals were -120 mesh. The nonmetallic inclusions were -60 +80 mesh for all but the particle size effect samples.

Surface oxides were removed from the lead, copper, and silver by a hydrogen anneal. The temperature and times used are listed in Table II.

TABLE I

EXTRUSION SAMPLE TYPES AND DEFORMATION PARAMETERS STUDIED

Type Sample	Deformation Parameters Studied
Cu - NaCl	Die cone angle Per cent reduction in area Per cent nonmetallic material Inclusion particle size Strain rate Temperature Type of nonmetallic material Matrix type
Ag - NaCl	Matrix type
Al - NaCl	Matrix type
Brass - NaCl	Matrix type
Pb - NaCl	Matrix type
Cu	Temperature Per cent nonmetallic material
Cu - KCl	Type of nonmetallic material
Cu - LiF	Type of nonmetallic material
Cu - NaF	Type of nonmetallic material
NaCl	Per cent nonmetallic material Temperature

TABLE II

HEAT TREATMENT DATA FOR POWDER PURIFICATION

Metal	Temperature, °F	Time, hrs.
Ag	1000	1/2
Cu	1000	1/2
Pb	500	1/2

A magnetic device was used so that the metals could be inserted in the furnace, annealed, and cooled to room temperature without being removed from the hydrogen atmosphere. The brass and aluminum powders were not annealed in hydrogen since the H_2/H_2O ratio was not high enough to remove the oxide layer from aluminum and brass powders dezincify during annealing.

The large metal-nonmetallic phase density difference leads to phase separation during mechanical mixing. To avoid this problem, hand mixing, which results in more uniform phase distribution, was used.

The samples were pressed in a single action, 3/8 inch diameter die. After the initial press, the samples were repressed from the opposite end. The two step pressing operation maximizes sample densification (Figure 7(a)) and yields samples which shrink uniformly during sintering.

The nonmetallic inclusions were flattened during the pressing operation, as shown in Figures 7(b) and 8. The inclusion length/width (L/W) ratio was used as an index of the amount of flattening where the length is measured in the direction of load application. Ideally, the L/W ratio would equal one in the unextruded sample.

The effect of pressing load on sample density is illustrated in Figure 7(c). Above some optimum load, the samples grow during sintering. The pressing loads listed in Table III were selected to minimize inclusion deformation and maximize sample densification. The samples were pressed at the same load prior to each sinter.

The maximum sintering temperature is limited by the melting point of the nonmetallic phase for all but the Pb-NaCl and Al-NaCl

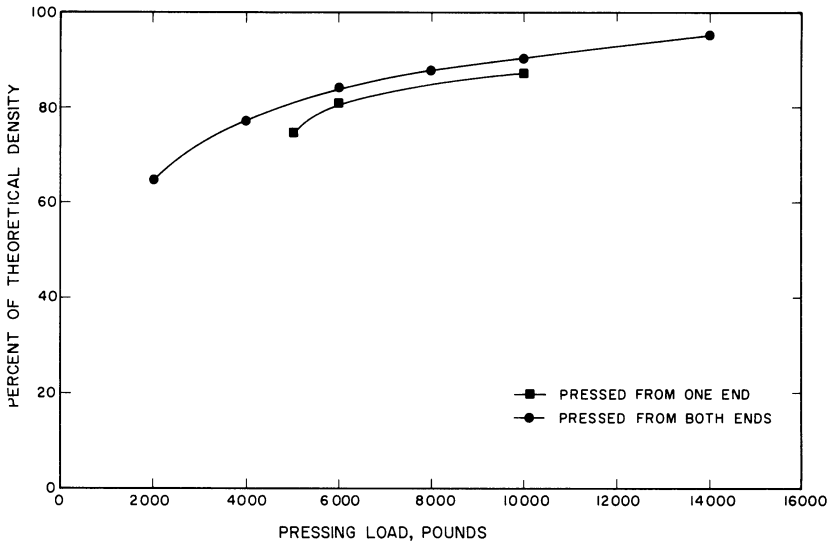

a) Effect of pressing method on sample density. Copper samples were used.

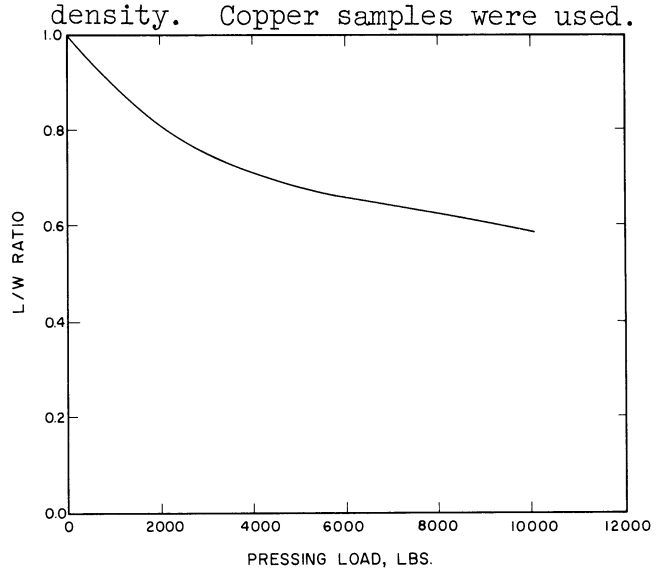

b) Pressing load vs. inclusion L/W ratio. Cu - 10 Per Cent NaCl samples were used. A single pressing and sintering operation was used.

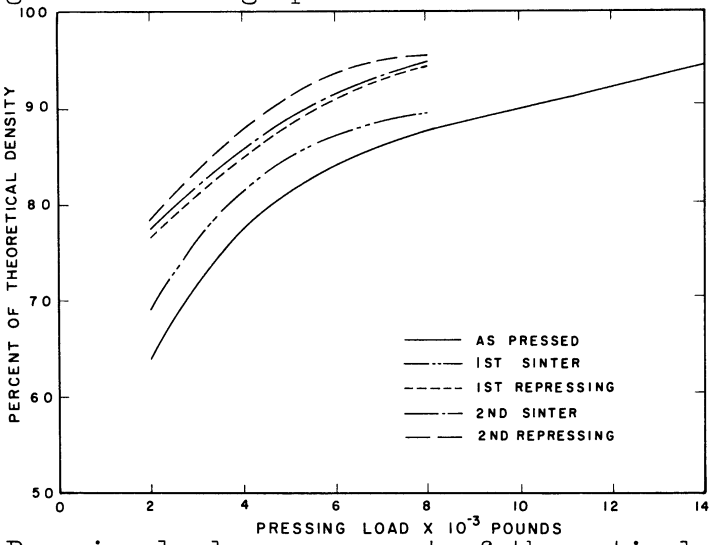

c) Pressing load vs. per cent of theoretical density. Copper samples were used.

Figure 7. The Effect of Pressing Variables on Sample Properties.

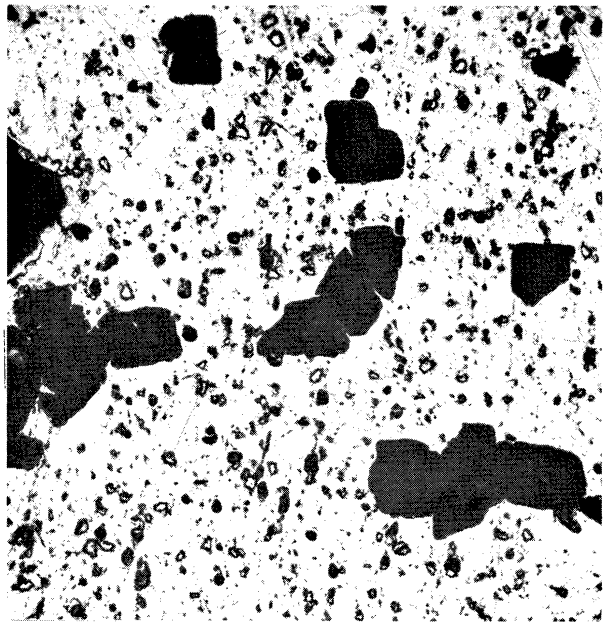

a) Sample: 90 Pb - 10 NaCl.
L/W Ratio: 0.937.

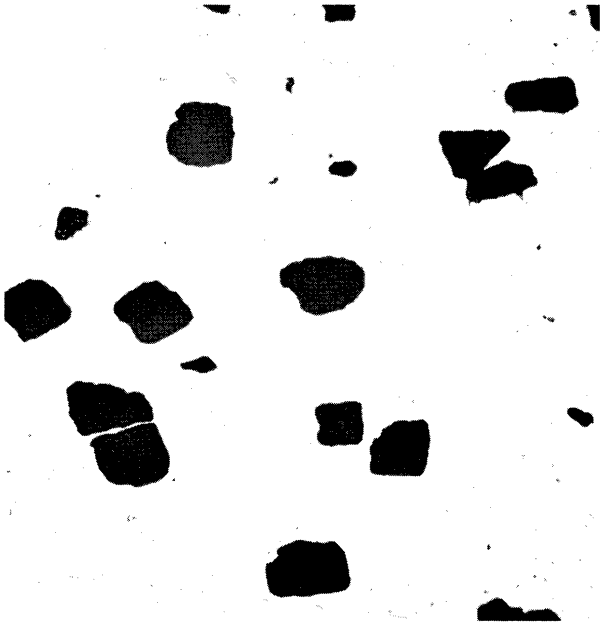

b) Sample: 90 Al - 10 NaCl.
L/W Ratio: 0.714.

c) Sample: 90 Cu - 10 LiF.
L/W Ratio: 0.620.

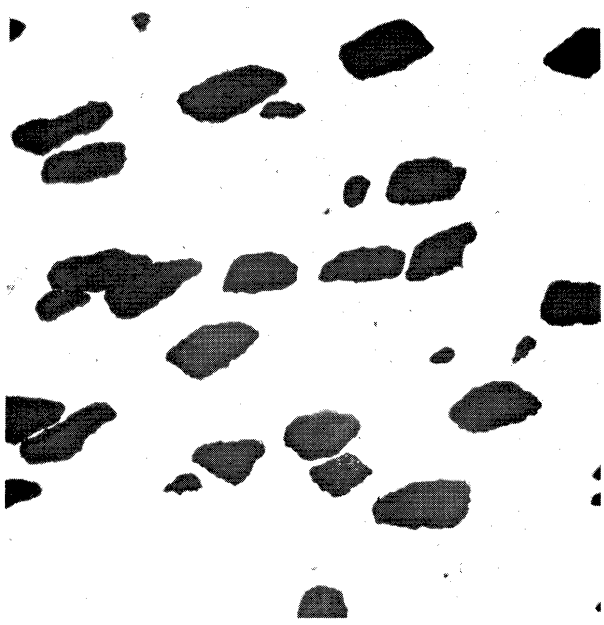

d) Sample: 90 Cu - 10 NaCl.
L/W Ratio: 0.536.

Figure 8. Microstructures of As-Sintered Samples. 37.5X.

TABLE III

PRESSING AND SINTERING TREATMENTS

Sample Type	Pressing Load, lbs*	Sintering Temp. °F(±10°F)
Ag - NaCl	4,000	1150
Al - NaCl	4,000	1150
Brass - NaCl	6,000	1430
Cu	6,000	1430
Cu - KCl	6,000	1380
Cu - LiF	6,000	1430
Cu - NaCl	6,000	1430
Cu - NaF	6,000	1430
NaCl**	6,000	1430
Pb - NaCl	4,000	575

* Load on a 0.375 inch diameter ram.

** The NaCl sample received a single pressing and six hr. sintering treatment.

samples since liquid inclusions were found to sweat from the samples. Since densification is controlled by the sintering of the metallic phase, the sintering temperatures were generally lower than the ideal sintering temperature. Pure copper, for example, was found to sinter more rapidly at 1650°F than at 1430°F.

Three pressing and sintering operations were used for each sample. With the temperature and load limitations, three pressing and sintering operations were necessary to obtain satisfactory densification.

The times for the three sinters were six hours, three hours, and three hours respectively. The sintering temperatures are listed in Table III. The samples were sintered and cooled in a hydrogen atmosphere.

c. As-Sintered Sample Properties-The densities and inclusion L/W ratios for the various as-sintered sample types are presented in Table IV.

2. Strain Hardening Study Samples

Strain hardening patterns were determined on annealed, high purity copper. The copper rods were machined to be a slip fit in the extrusion assembly and the sample length was approximately 0.4 inches. The samples were annealed in hydrogen for one hour at 1430°F (±10°) before and after machining.

3. Inclusion Hardness Samples

Single crystals of KCl, NaF, and LiF were used for hardness samples. The crystals were cleaved along (100) crystal faces from the furnace-cooled melts described in section A-1-a of this chapter. After cleaving, the single crystals were annealed in hydrogen for the temperatures and times listed in Table V.

4. NaCl Hardness Samples

Room and elevated temperature NaCl hardness measurements were made on optical quality single crystals purchased from the Harshaw Chemical Company. Prior to testing, the crystals were annealed in hydrogen for the temperatures and times listed in Table V.

TABLE IV

AS-SINTERED EXTRUSION SAMPLE PROPERTIES

Sample Type	Per cent of Theoretical Density	L/W Ratio
Brass - NaCl	90.8	0.533
Cu - NaCl	94.7	0.536
Cu - NaF	92.9	0.620
Cu - LiF	93.3	0.666
Cu - KCl	93.8	0.461
Al - NaCl	96.5	0.714
Ag - NaCl	96.9	0.745
Pb - NaCl	100.0	0.937
Cu	94.8	-
NaCl	93.1	-

TABLE V

IONIC SINGLE CRYSTAL HEAT TREATMENT DATA

Sample	Annealing Temperature °F ($\pm$10°F)	Annealing Time Hrs.
KCl	1380	2
NaCl	1430	2
NaF	1430	2
LiF	1430	2

5. Compressive Yield Strength Samples

Compressive yield strength was determined as a function of matrix hardness using 90 Cu - 10 NaCl extrusion type samples (Section A-1 of this chapter). The samples were hardened after the final sinter by repressing the sample from both ends in the original pressing die. The pressing load-sample hardness relationship is shown in Figure 9.

B. Testing Techniques

The experimental testing procedure will be described under the following headings:

1. Method of Inclusion Deformation.
2. Metallographic Techniques.
3. Hardness Measurements.
4. Yield Strength Determinations.
5. Sample Density Determinations.

1. Method of Inclusion Deformation

a. Selection of the Deformation Method-Plastic flow in a deformation study can either be "constrained" or "unconstrained." "Unconstained" plastic flow occurs with methods such as tensile testing under hydrostatic pressure, as used by Bridgman;[62] or tube testing under combined tension and torsion, as used by Taylor and Quinney.[119] "Unconstrained" test methods are useful for determining the yield strength of a material. However, continuing changes in sample geometry make these methods unsuitable for deformations involving large plastic strains.

"Constrained" flow tests, such as extrusion, involve high frictional forces which are often difficult to evaluate. However, they

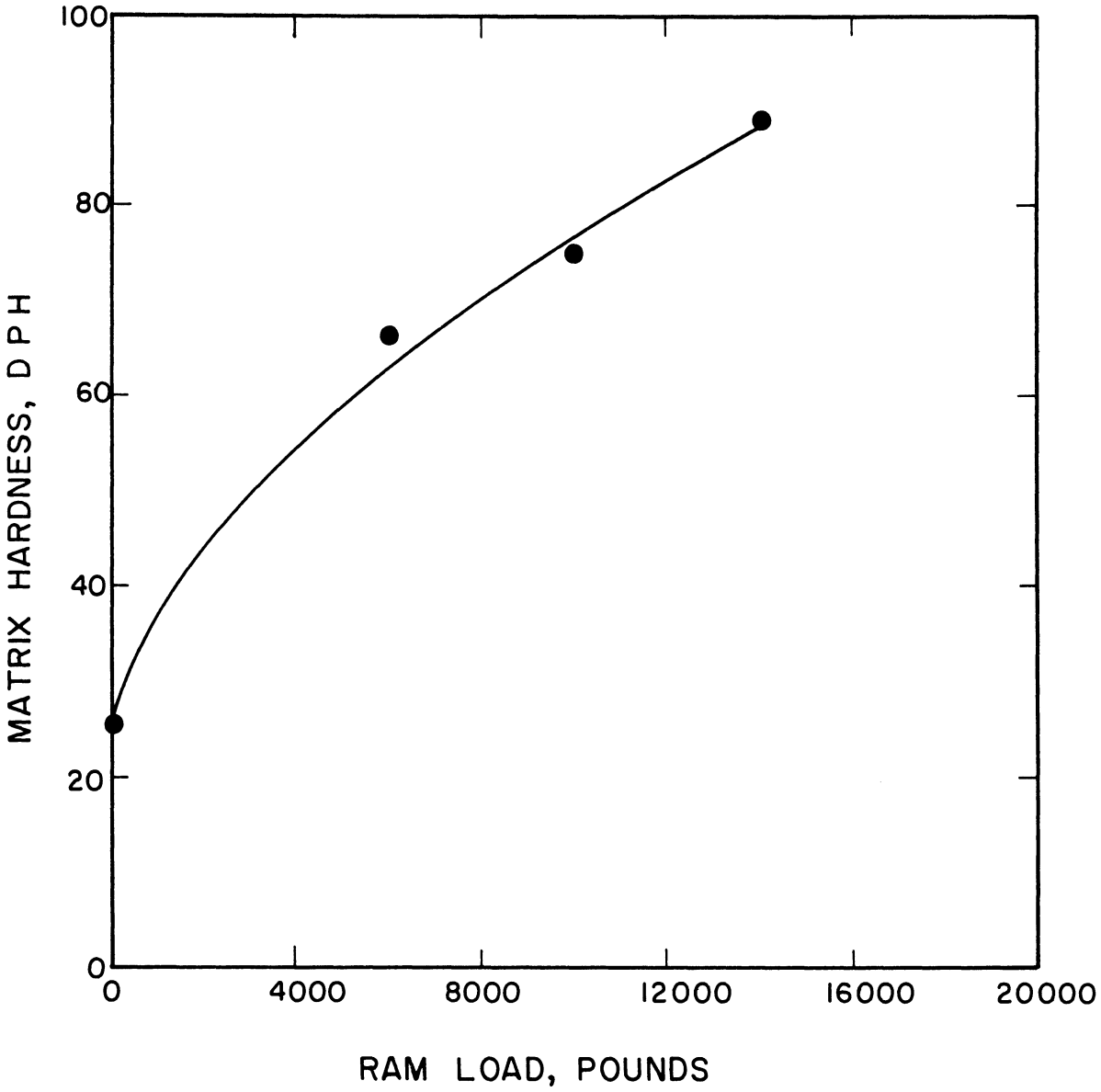

Figure 9. Pressing Load versus Matrix Hardness. 90 Cu - 10 NaCl samples were used.

provide constant strain patterns throughout the test. The latter factor makes "constrained" methods more suitable for tests involving large plastic strains.

Extrusion was selected as the test method. A number of factors influenced this choice:

1. Extrusion theory is better developed than rolling theory.
2. Ram pressures can be easily measured.
3. Dies can be changed to provide a wide range of stress distributions in the sample.
4. One die can be used for a number of tests. Consequently, the effect of individual parameters, such as temperature and sample type, can be readily determined.
5. Extrusion provides stress distributions the same as, or similar to, those found in the metal forming processes of major interest; i.e., extrusion, drawing, and rolling.

The stresses acting on a material element are somewhat similar for extrusion, drawing, and rolling. The similarities are great enough that inclusion deformation results for extrusion would be expected to apply to the other forming operations.

Consider the stresses on the elements shown in Figure 10. The roll shape can be considered as a conical die with a continually turning tangent. For sheets with a width to thickness ratio greater than 10/1, the sheet does not deform significantly in the Z direction. Consequently, the stress σ_Z would be compressive in the interior of the sheet. The constraint offered by the rolls would make σ_φ compressive. For extrusion and drawing, the die constraint would make the stresses σ_φ and σ_θ

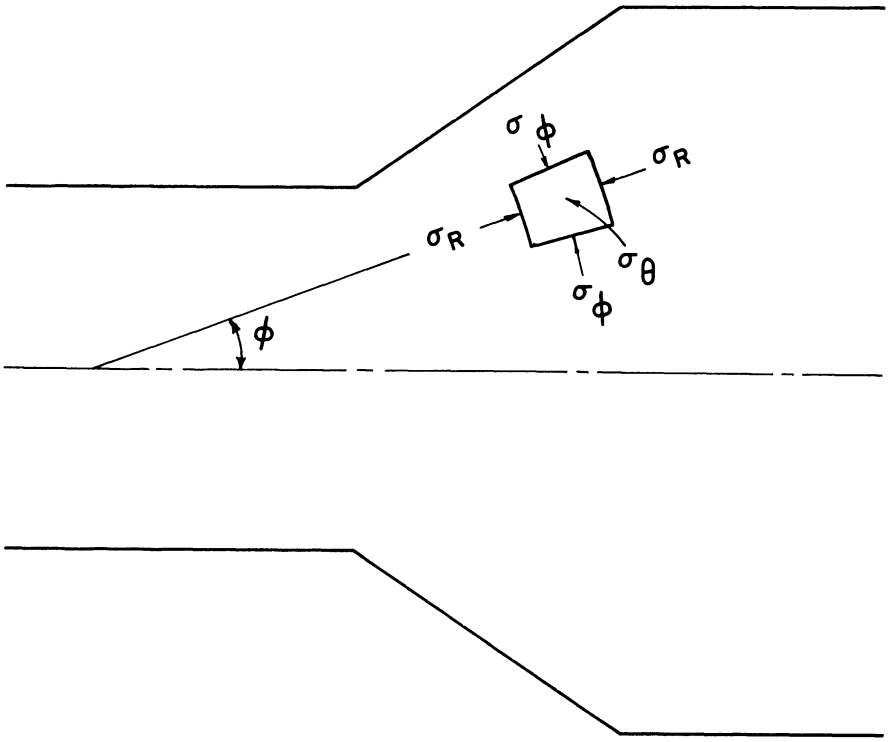

a) Extrusion and drawing

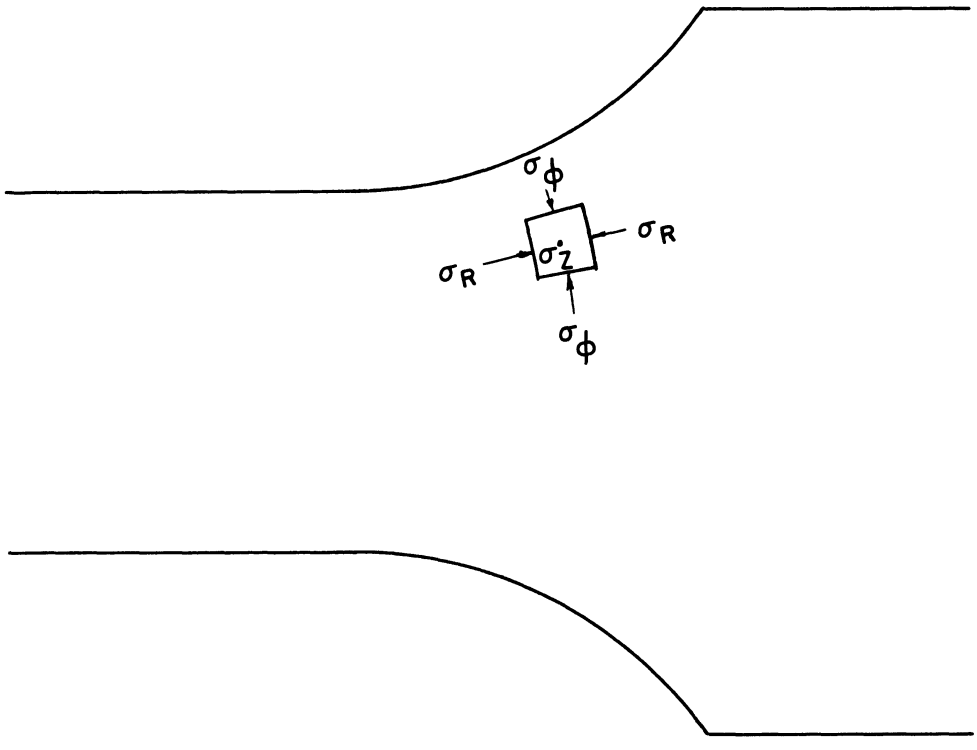

b) Rolling

Figure 10. Stress Components Acting on a Material Element for Extrusion, Drawing, and Rolling.

compressive. As a result, a material element in rolling, drawing, and extrusion is subjected to compressive stresses in two directions. For all three processes, σ_R is compressive for some values of $\underline{R}$ and tensile for others. The tensile and compressive regions depend on the nature of the process and the use of front and back tensions. For extrusion, σ_R is primarily compressive while the converse is true for drawing. The presence of tensile and compressive values of σ_R in rolling can be demonstrated by the following analysis.

The sheet velocity increases during rolling since the area is being reduced. At some point (neutral point), the roll velocity equals the sheet velocity. From the roll entrance to the neutral point, the roll travels faster than the sheet. This velocity difference introduces tensile stress in the $\underline{R}$ direction. Between the neutral point and the exit, the rolls move slower than the sheet, introducing compressive forces in the $\underline{R}$ direction.

b. Extrusion Equipment-A series of extrusion dies were used to permit studies of the effects of per cent reduction in area and included die angle. The geometries of these dies are listed in Table VI.

Extrusions were run at subzero, room, and elevated temperatures. The basic extrusion equipment shown in Figure 11 was used for all runs. For subzero runs, the extrusion equipment was immersed in a dry ice-alcohol bath. The extrusion temperature was assumed to be the sublimation temperature of dry ice (-108.6°F). For elevated temperature tests, the experimental equipment was inserted in a tube furnace with chromel-alumel thermocouples placed at the locations indicated in Figure 11.

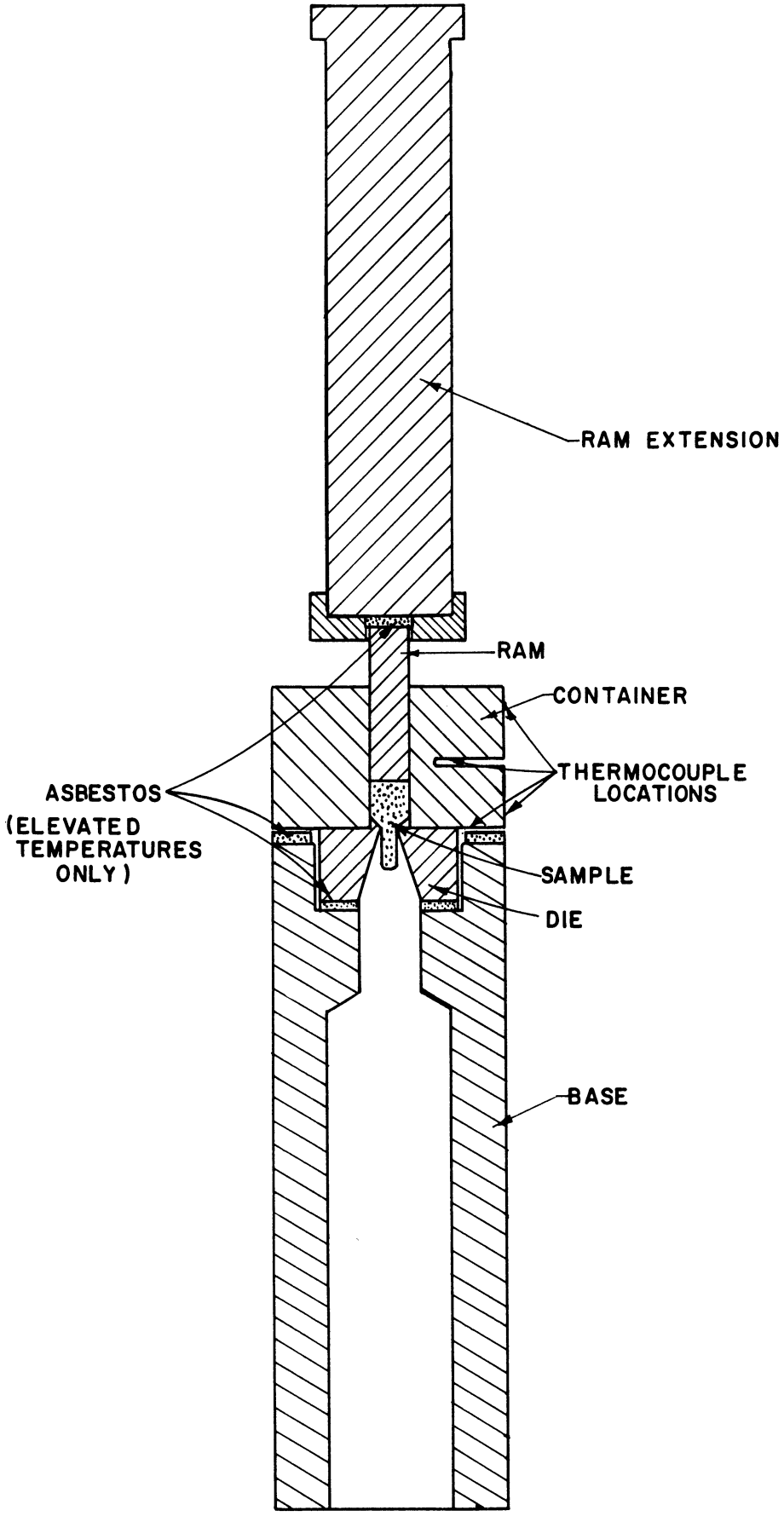

Figure 11. Extrusion Equipment.

The reported extrusion temperature is the average temperature for the two internal couples.

TABLE VI

EXTRUSION DIE GEOMETRIES

Die No.	Initial Diameter, (inches)	Final Diameter, (inches)	Actual Reduction in Area, (%)	Nominal Reduction in Area, (%)	Included Die Angle (degrees)
1	0.375	0.1885	74.73	75.00	60
2	0.375	0.1930	73.51	75.00	90
3	0.375	0.1885	74.73	75.00	135
4	0.375	0.1887	74.68	75.00	180
5	0.375	0.3118	30.87	30.56	90
6	0.375	0.2500	55.55	55.55	90
7	0.375	0.1276	88.45	88.89	90

A Baldwin-Southwark tensile machine (60,000 lb. maximum load) was used in compression to extrude the samples. Prior to each run, the table speed (and thus the ram velocity) was calibrated. A ram velocity of 0.10 inches per minute was used for all but the strain rate study samples. A Baldwin-Microformer-Recorder was used to record ram load as a function of time. The ram load-time curve and the ram velocity calibration were used to construct ram pressure-ram displacement curves.

All die parts in contact with the sample were coated with a stearic acid-graphite lubricant. Ether was used as the lubricant vehicle.

2. Metallographic Techniques

Data measurements were made along a symmetry plane parallel to the extrusion direction. The final polished section was less than $\pm$ 0.0015 inches from the centerline of the extrusion. The tolerance was generally less than $\pm$ 0.0005 inches.

The inclusion materials are highly water soluble. Consequently, ethyl alcohol was used instead of water for wet grinding all samples containing inclusions. With this exception, standard metallographic techniques were used. Diamond paste was used for the final polishing.

3. Hardness Measurements

a. Room Temperature Measurements-A standard 136° diamond pyramid indentor was used with a Tukon microhardness testing instrument for all room temperature hardness measurements. A 10 gram load was used for inclusion hardness measurements in extruded samples while a 500 gram load was used for all other room temperature measurements. Hardness values obtained with a 10 gram load were 1/3 less than those obtained with a 500 gram load for the range from 10 to 210 DPH. Since the 500 gram measurements check with the standard hardness block supplied with the Tukon tester, all 10 gram DPH measurements were corrected by a factor of 1.5.

Inclusion hardnesses in extruded samples were measured within 0.25 mm of the sample centerline. Annealed inclusion hardnesses were measured on (100) faces of single crystals. In both cases, the reported results are the average of six measurements.

To determine matrix hardnesses, three traverses were made perpendicular to the sample centerline. Hardness readings were taken in mirror image positions across the sample centerline with 0.50 mm or less between each indentation in the traverse. The average of the six hardness values from equivalent positions was plotted as a function of sample position (Figure 12). When a single hardness value is reported for a sample, it is the average of the hardness values across the sample. Matrix/inclusion hardness ratios were calculated for hardnesses at the center of the samples.

Strain hardening patterns were determined on partially extruded copper samples. Hardness traverses were run perpendicular to the extrusion direction. These hardness traverses were never more than 1 mm apart and in regions where the hardness values were changing rapidly, they were 0.5 mm or less apart. The same is true for the distance between indentations in each traverse. The data were made symmetric by averaging the mirror image hardness values in each traverse.

Hardness vs. position plots were drawn for lines parallel and perpendicular to the extrusion direction. From these plots, lines of constant hardness were drawn as shown in Figure 13. The experimental constant hardness points are shown in the right half of the figure while smooth curves for the constant hardness profiles are shown on the left. Since the limit of accuracy for the hardness values is approximately two per cent, the curves shown in the right half of the figure are not justified.

b. Elevated Temperature Measurements-Elevated temperature hardness measurements were made on (100) faces of NaCl single crystals. The

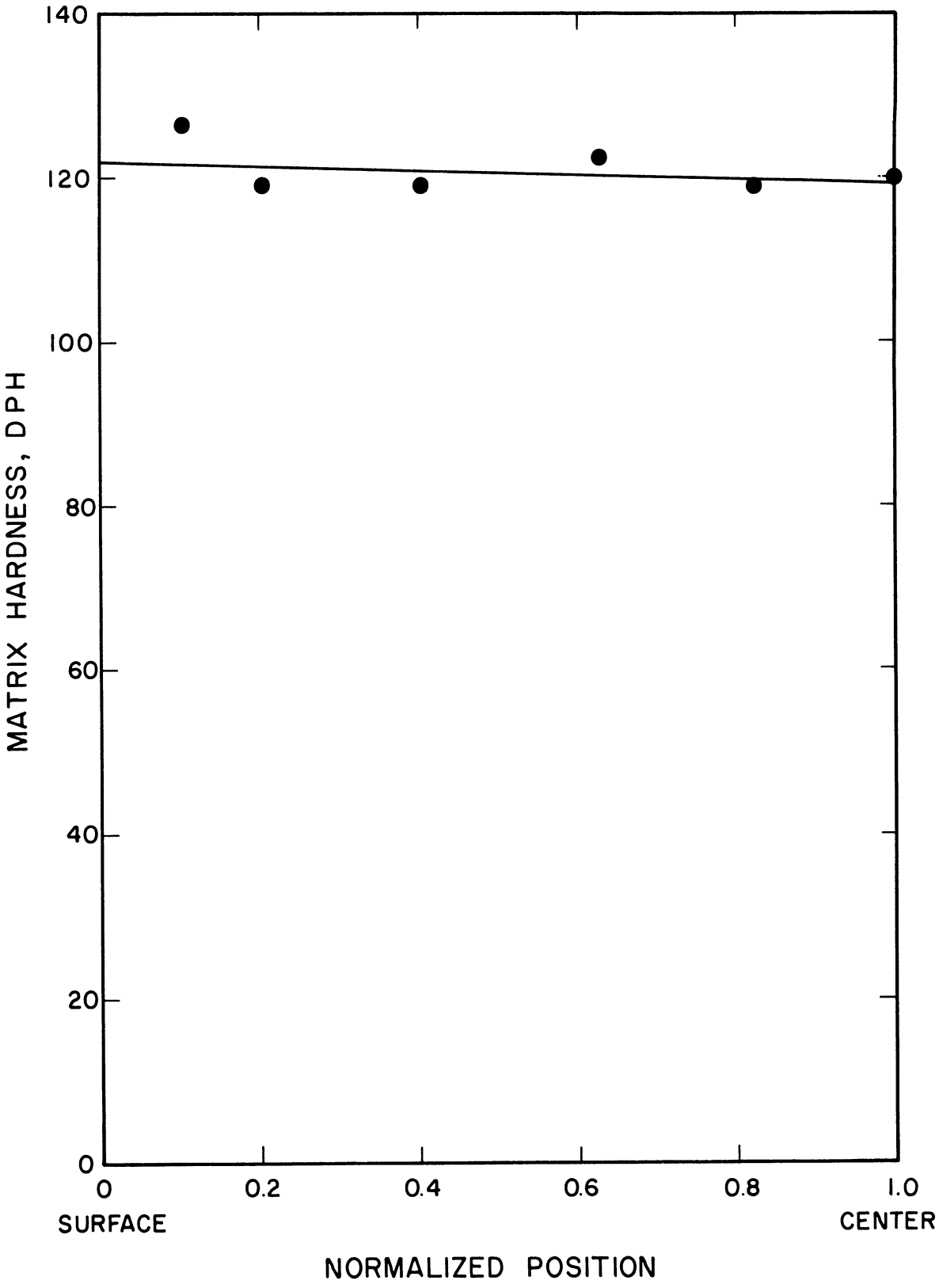

Figure 12. Typical Matrix Hardness Traverse.

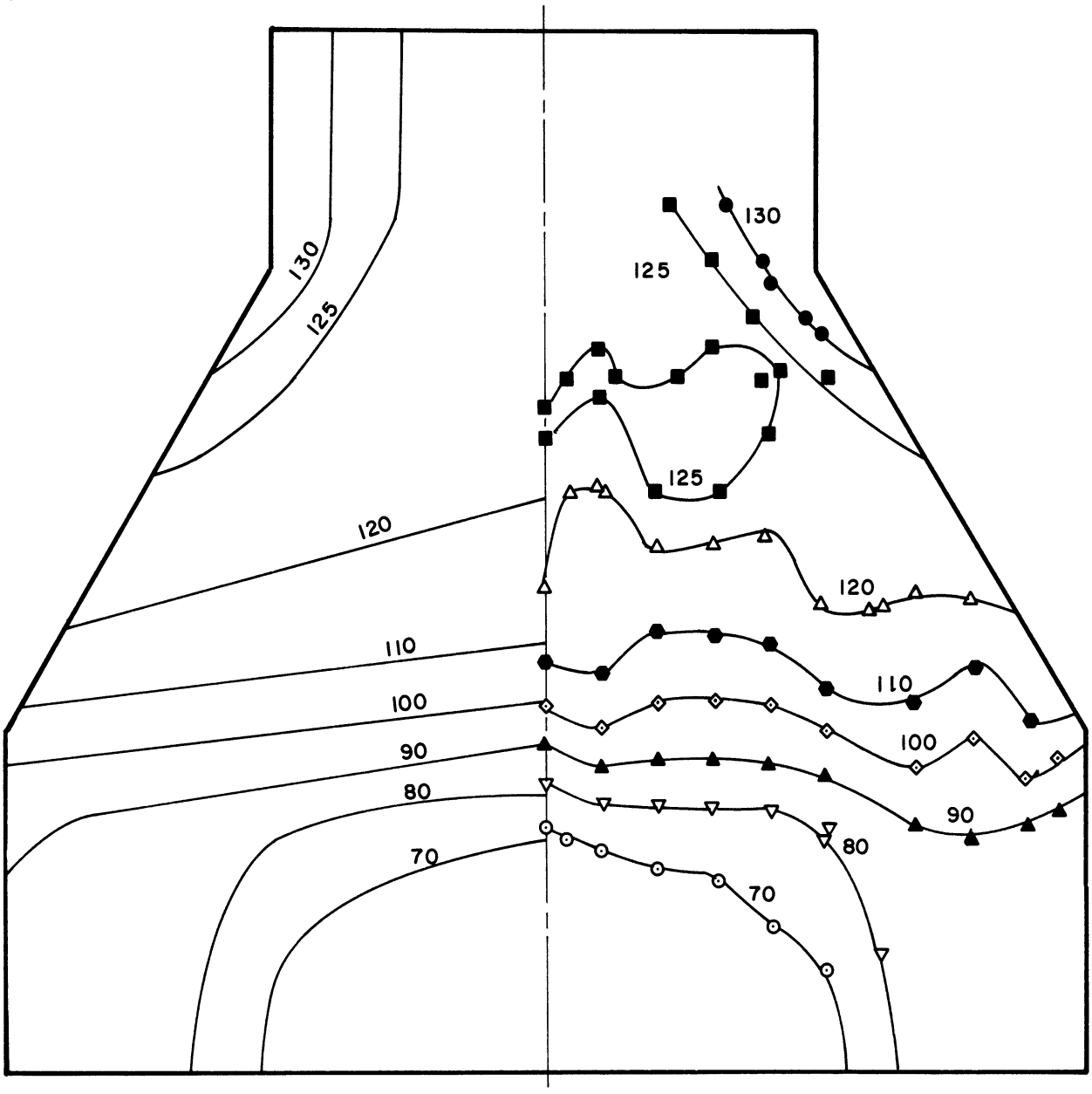

Figure 13. Strain Hardening Pattern for a 60° - 75 Per Cent Reduction Die.

hot hardness device shown in Figure 14 was used with a Vickers hardness tester. The applied load was calibrated by comparing room temperature hardness indentations made with the hot hardness arrangement with those made on the same NaCl crystal with the Tukon tester. A 500 gram load was used with the Tukon hardness machine to obtain the calibration factor. The temperature control was $\pm$ 10°F. The tests were run under a positive helium pressure equivalent to 1.5 inches of mercury. The indentations were measured at room temperature using the Filar eyepiece on the Tukon tester.

4. Yield Strength Determinations

The tensile machine and load recording system used for the extrusion studies (Section B-1-b of this chapter) were also used to determine compressive yield strength data. Parallel pressing surfaces were insured by the use of the compression jig shown in Figure 15. A stearic acid and graphite lubricant was applied to the ends of the sample. The reported yield strengths were determined by the 0.1 per cent offset method.

5. Sample Density Determinations

Sample density calculations were based on the weight and dimensions of as-sintered samples which were weighed to $\pm$ 0.0005 grams and measured to $\pm$ 0.0002 inches. Allowing for scatter between samples, the minimum accuracy for the per cent of theoretical density figures is $\pm$ 0.5 per cent.

The following formula was used to calculate the theoretical density of two phase samples

$$\rho_T = \rho_M f_M + \rho_I f_I \qquad (26)$$

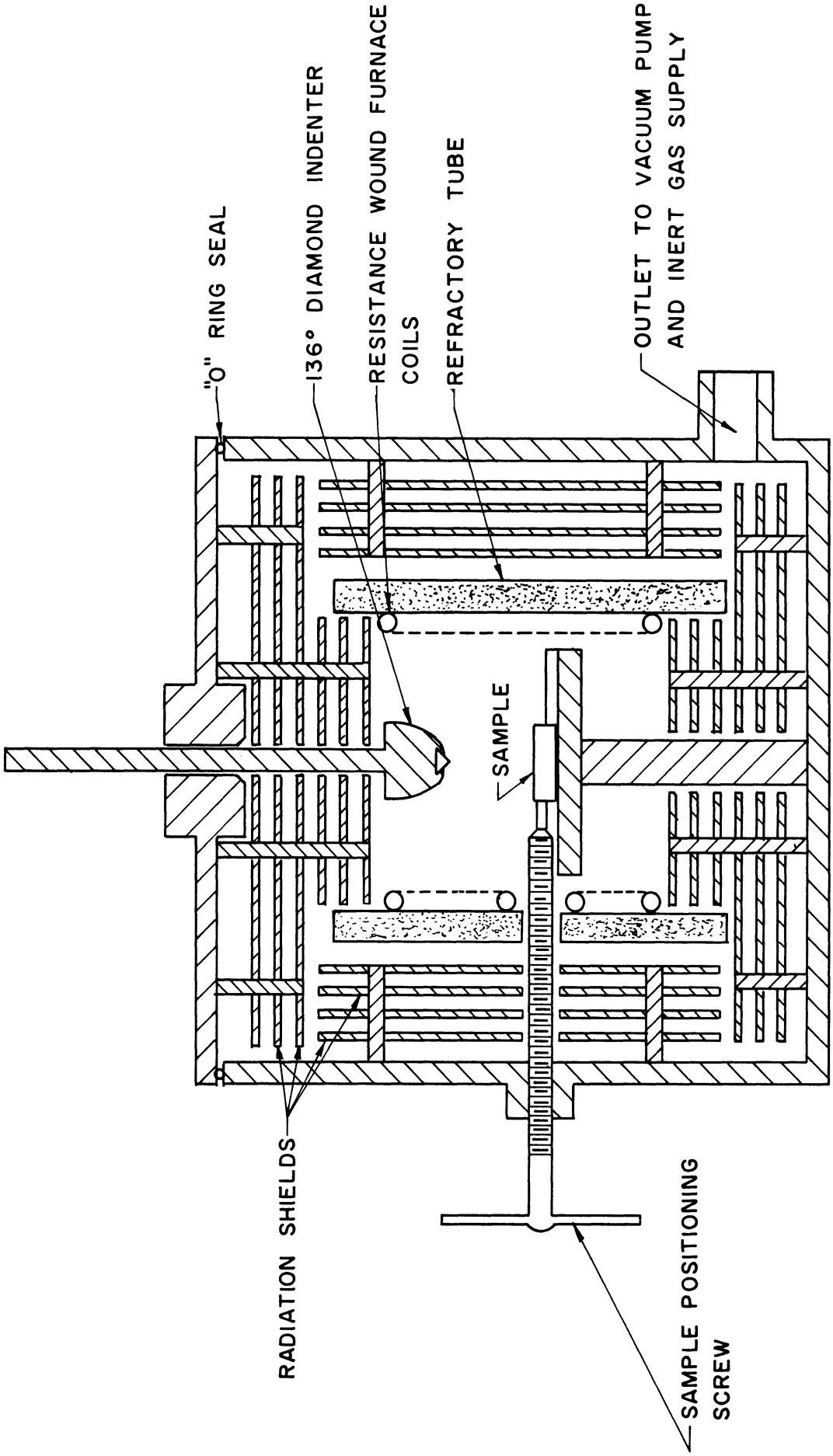

Figure 14. Hot Hardness Testing Equipment.

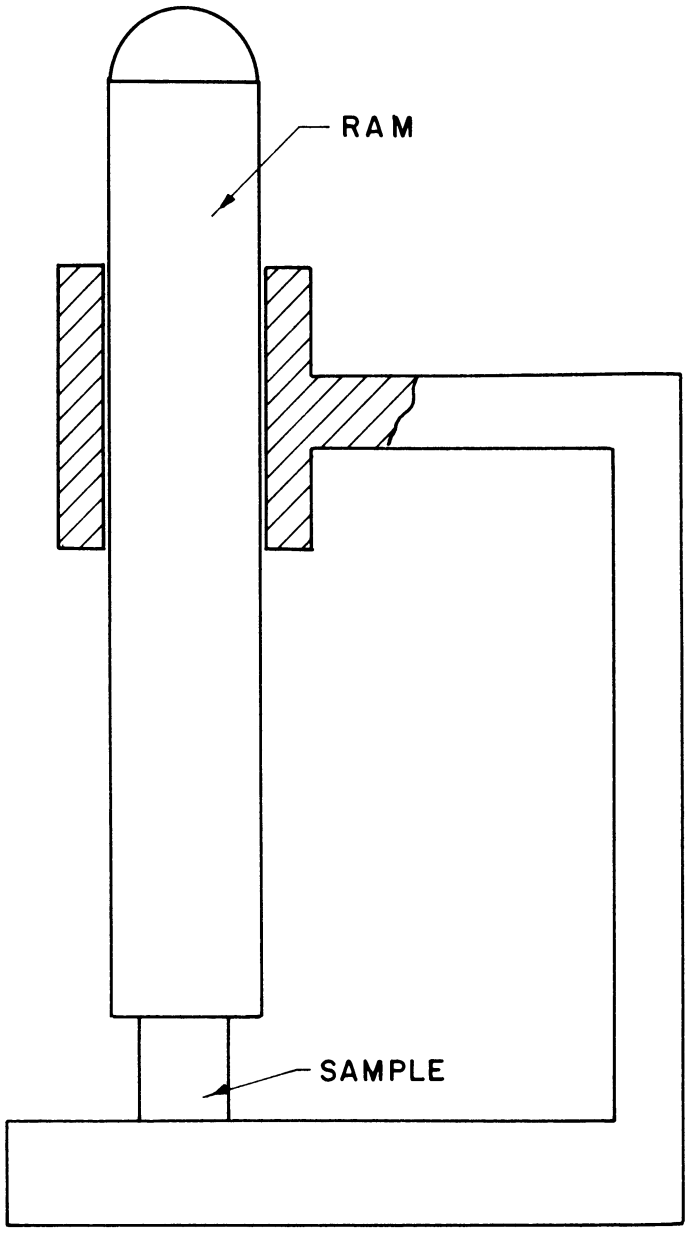

Figure 15. Compression Testing Jig.

where ρ_T is the theoretical density, ρ_M is the metal density, ρ_I is the inclusion density, f_M is the metal volume fraction, and f_I is the inclusion volume fraction.

CHAPTER IV

ANALYSIS OF INCLUSION DEFORMATION

The techniques used for the analysis of inclusion deformation are sufficiently involved to merit a separate chapter. They will be described under the following headings: (A) Strain Analysis of Deformation and (B) Stress Analysis of Deformation.

A. Strain Analysis of Deformation

Analytic techniques were used for strain measurements will be considered under the headings:

1. L/W Measurements.
2. The "Mean L/W Value."
3. L/W Correction for Density.
4. L/W Correction for As-sintered L/W Ratio.

1. L/W Measurements

Strain measurements were made along a symmetry plane parallel to the extrusion direction. The inclusion length/width ratios are used as a measure of the strain (Figure 16). If the inclusions are ellipsoidal, the L/W ratio in the plane of measurement represents the true inclusion L/W ratio as demonstrated in Appendix A.

Inclusion L/W ratios were measured using the Filar eyepiece of a Tukon hardness tester. The micrometer dials on the Tukon are used to determine the position of each inclusion in the sample. The measured L/W ratio is accurate to within $\pm$ 1% of the actual L/W value in the polished surface. To eliminate end effects, inclusions were not measured near either end of the sample.

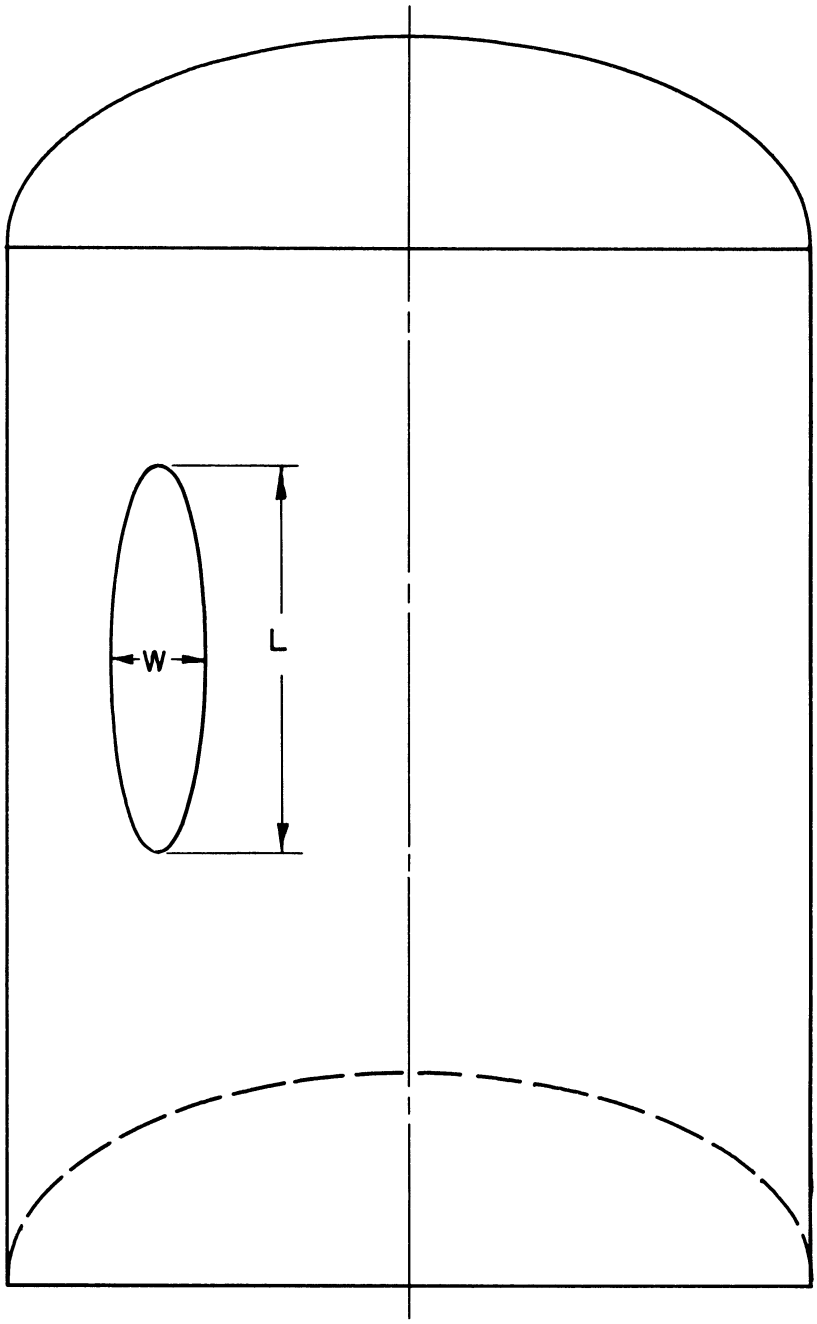

Figure 16. Quantities Measured as an Indication of Strain.

The extruded inclusions were measured in a series of longitudinal bands 0.30 mm. wide with the exception of the 30.9% reduction sample. Band widths of 0.50 mm were used for this sample and all as-sintered samples. To make the data symmetric, bands equidistant from the sample centerline were considered as pairs. An equal number of L/W values (10-15) was taken from each band in the pair. These L/W values are presented in a cumulative plot, as shown in Figure 17 and the 50% point of the cumulative curve is taken as the L/W ratio of the band pair. The L/W ratio of each band pair is plotted as a function of normalized position across the extruded sample, as shown in Figure 18.

2. The "Mean L/W Value"

To illustrate the effects of various parameters on inclusion deformation, a single strain figure would be desirable for each sample. The "mean L/W value" was calculated for this purpose where the "mean L/W value" of a sample is given by the quantity

$$\frac{\sum_{i} (L/W)_i A_i}{A_t} \qquad (27)$$

where $(L/W)_i$ is the L/W ratio of band i, A_i is the cross-sectional area of band i, and A_t is the total cross-sectional area of the sample. This quantity serves as a relative index for the amount of nonmetallic deformation occurring in a sample.

3. L/W Correction for Density

Most of the samples have less than theoretical density prior to extrusion. With the high stresses developed, some densification would be expected during extrusion and if it occurs, the resulting L/W value

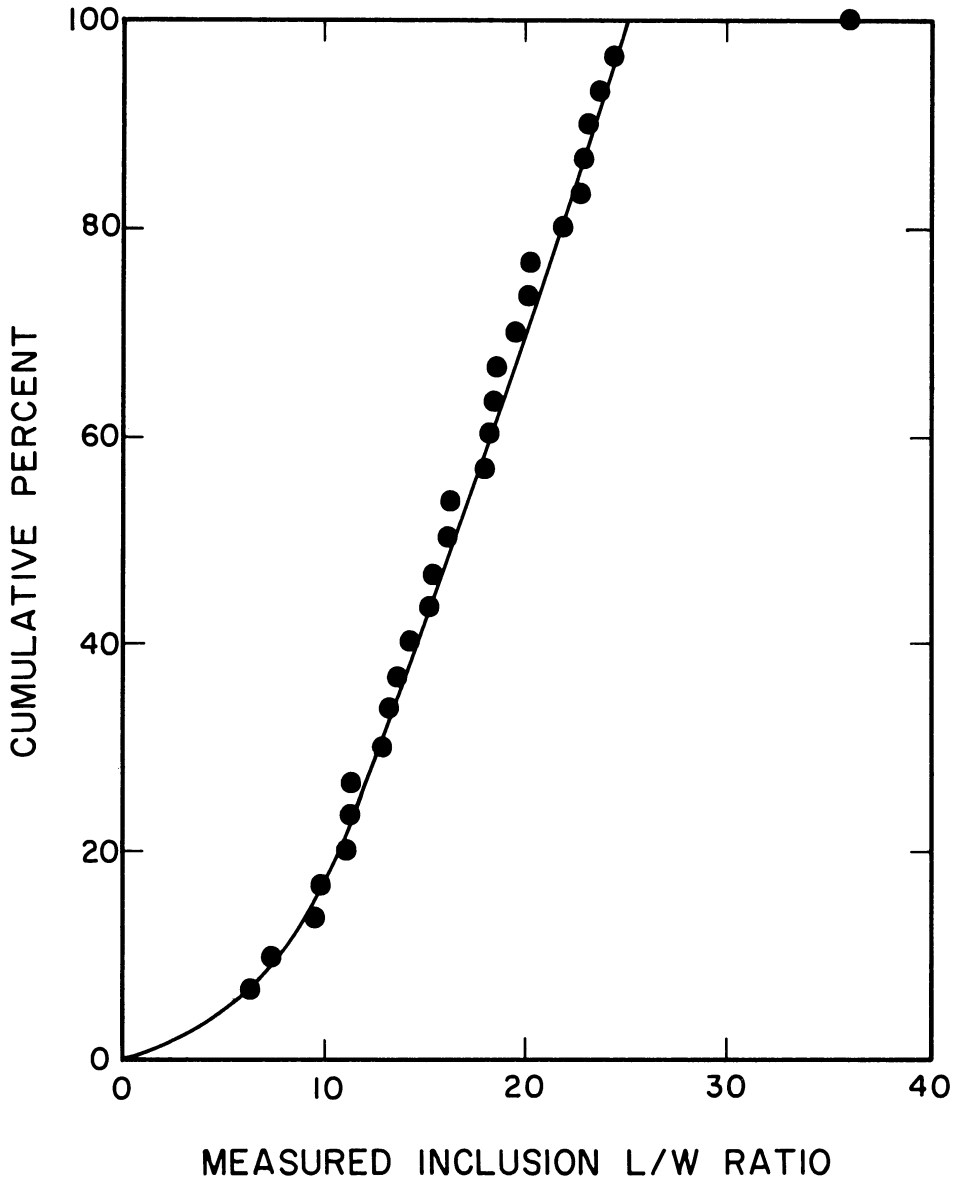

Figure 17. Typical Cumulative L/W Curve.

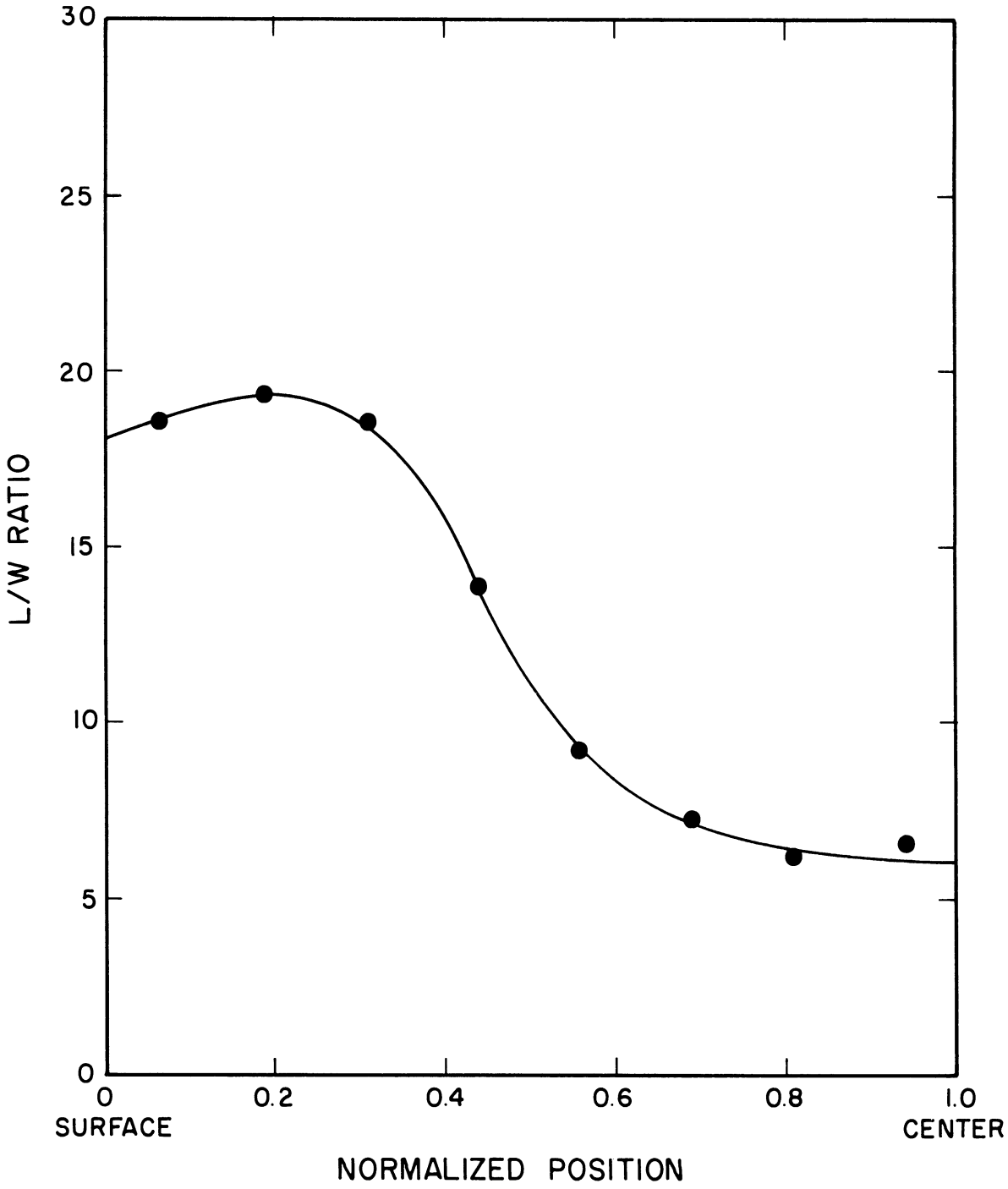

Figure 18. Typical L/W Traverse.

for the bulk sample will be less than the L/W value for a sample having theoretical density.

The initial and final sample weights (Wt) will be the same. Thus,

$$(Wt)_o = (Wt)_f \tag{28}$$

where the subscripts refer to the states before (o) and after (f) extrusion. In terms of density (ρ), sample length (L) and diameter (W), Equation (28) becomes

$$L_o W_o^2 \rho_o = L_f W_f^2 \rho_f \tag{29}$$

or, solving for L_f,

$$L_f = \frac{L_o W_o^2 \rho_o}{W_f^2 \rho_f} \tag{30}$$

For no density change ($\rho_o = \rho_f$), the final sample length (L_f') would be

$$L_f' = \frac{L_o W_o^2}{W_f^2} \tag{31}$$

For the bulk sample, W_f is fixed by the die opening. Consequently, dividing Equation (31) by Equation (30) we have

$$\frac{L_f'}{L_f} = \frac{\rho_f}{\rho_o} \tag{32}$$

The corrected L/W value (L_f'/W_f) given by

$$\frac{L_f'}{W_f} = \left(\frac{\rho_f}{\rho_o}\right)\left(\frac{L_f}{W_f}\right) \tag{33}$$

where (L_f/W_f) is the measured L/W value.

The maximum L/W correction for densification would result when ρ_f is the theoretical density (ρ_T). Consequently, the maximum correction

for the bulk sample is given by

$$\left(\frac{L}{W}\right)_{CORRECTED} = \left(\frac{\rho_T}{\rho_o}\right)\left(\frac{L}{W}\right)_{MEASURED} \tag{34}$$

The correction for the bulk sample is assumed to apply to the inclusions. Since theoretical density would not be expected during extrusion, Equation (34) probably yields the maximum correction needed.

Unless specifically indicated, this correction factor will not be applied to the data presented in the thesis. Maximum corrected L/W values are less than 10% greater than the measured values.

4. L/W Correction for As-sintered L/W Ratio

The inclusions in the as-sintered samples have a L/W ratio less than one and should thus be corrected for an equivalent original L/W ratio of one. Consider the model shown in Figure 19(a). The shaded area in the as-sintered inclusion has a L/W ratio of one, while the extruded L/W ratio for the shaded area is L_f/δ. The quantity L_f/δ is the corrected L/W ratio. The ratio of the width of the shaded area to the total inclusion width (L_o/W_o) would be the same before and after extrusion. Therefore, δ is given by

$$\delta = W_f\left(\frac{L_o}{W_o}\right) \tag{35}$$

and the corrected L/W ratio is

$$\left(\frac{L}{W}\right)_{CORRECTED} = \frac{L_f}{\delta} = \frac{\left(\frac{L_f}{W_f}\right)}{\left(\frac{L_o}{W_o}\right)} \tag{36}$$

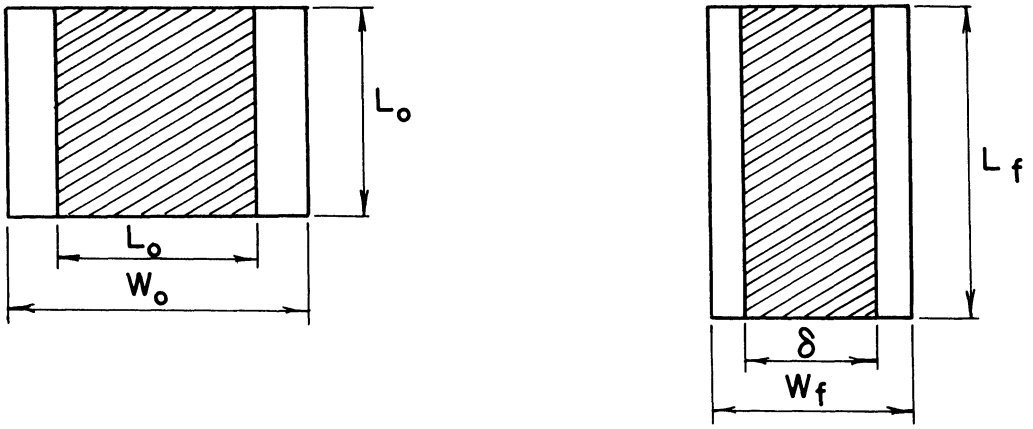

Before extrusion After extrusion

a) Inclusion deformation near the center of the sample.

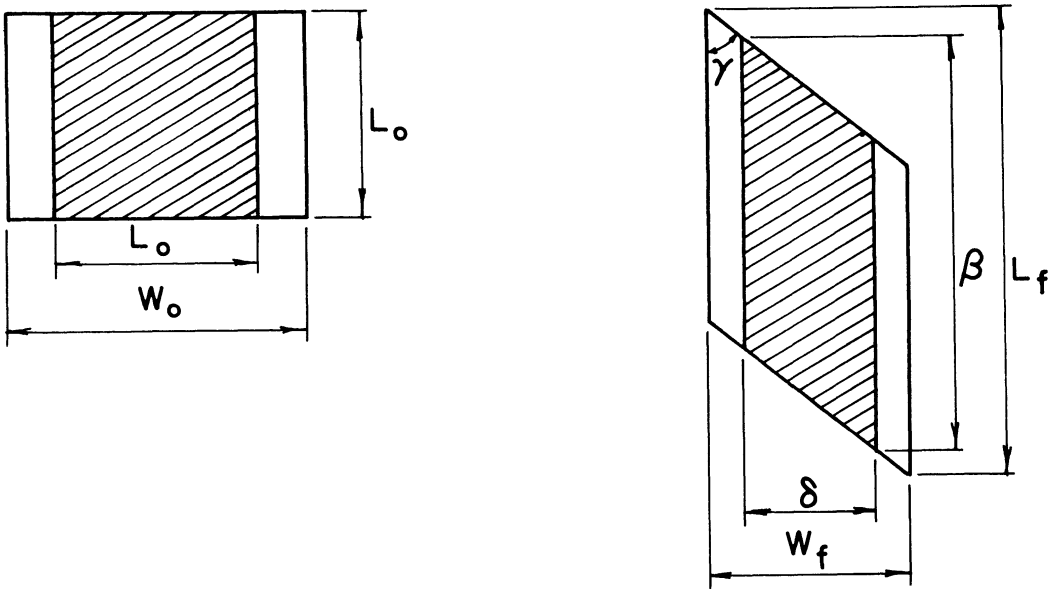

Before extrusion After extrusion

b) Inclusion deformation near the surface of the sample.

Figure 19. Schematic Figures Used for the L/W Correction for As-Sintered L/W Ratio.

The corrected L/W ratio is simply the measured L/W ratio for the extruded sample divided by the L/W ratio for the as-sintered sample.

Sachs and Eisbein's[95] results for grid distortion during extrusion indicate that Equation (36) would give a valid correction for inclusions near the center of the sample. As the sample surface is approached, however, an originally rectangular region is deformed as shown in Figure 19(b). Higher shear stresses near the sample surface cause the change in the flow pattern.

For the case shown in Figure 19(b), the corrected L/W ratio is β/δ where δ is given by Equation (35). Since $\beta < L_f$, the corrected L/W value for this case is given by

$$\left(\frac{L}{W}\right)_{CORRECTED} = \frac{\beta}{\delta} = \frac{\left(\frac{\beta}{W_f}\right)}{\left(\frac{L_o}{W_o}\right)} < \frac{\left(\frac{L_f}{W_f}\right)}{\left(\frac{L_o}{W_o}\right)} \qquad (37)$$

Since L_o/W_o is less than one, the correction given by Equation (36) is too large as the sample surface is approached.

In general, measured L/W values are presented in this thesis. The measured data accurately indicate trends where the sample type is held constant. It should be realized, however, that corrected L/W values will be somewhat greater than the measured values. Where data for several sample types are considered, a curve for the center L/W values will be presented. These center L/W values will be corrected for the original L/W ratio by use of Equation (36).

B. Stress Analysis of Deformation

Stress analyses were considered to see if the stress levels acting on the inclusions could be determined. If the inclusion stress state could be determined, a stress-strain correlation could be attempted.

1. Extrusion Theory Selection

The extrusion stress analyses presented in the literature are listed below:

1. Homogeneous deformation.
2. Plane strain extrusion without friction.
3. Plane strain extrusion with friction.
4. Slip line theories.
5. Axially symmetric extrusion.
6. Stress determination from gridded samples.

These methods will be referred to by number in the ensuing discussion. The extrusions theories associated with these methods are discussed in Chapter II.

The experimental data available for use with the extrusion theories are:

1. Die angle.
2. Per cent reduction.
3. Sample yield strength.
4. Ram pressure.
5. Strain hardening patterns.

The extrusion theory selected should be able to predict stress levels on the basis of these boundary conditions. The coefficient of friction between the billet and the die wall is unknown.

Method six was eliminated since (1) incremental deformation would introduce extraneous variables for elevated temperature studies and since (2) it is unduly cumbersome for the number of samples to be

considered. The other extrusion theories are developed for isotropic, rigid-plastic, incompressible, non-strain hardening materials. Consequently, consideration of these factors would not lead to the selection of one theory over another.

The following reasoning was used in selecting an extrusion theory from methods one through five. Methods one and two were eliminated (1) since they do not consider frictional forces and (2) since ram pressures predicted from them are significantly low. Method three was eliminated since (1) the stress components are independent of the angle φ (Figure 4(b)), which would not be expected, and (2) the analysis is for the plane strain case. Shield's[111] axially symmetric analysis (method f) was selected over the slip line theory (method 4) since it can be readily programmed for use with a computer.

2. Application of Shield's Analysis

Shield[111] applied his analysis for plastic flow in a converging conical channel to the case of drawing. The mathematic modification of his analysis for extrusion is presented in Appendix B. The method and assumptions used in applying the modified analysis are presented in this section.

Shield's[111] analysis assumes an isotropic, non-strain hardening material and does not account for the stress required to change the direction of material flow at the die entry and exit sections. For the modified analysis, the samples are assumed to behave isotropically in the bulk. Since the relative amount of stress required to change the direction of material flow decreases as the sample reduction increases, this

stress was assumed to be a negligible portion of the stress required for extrusion (ram pressure).

Since strain hardening during extrusion can not be neglected, hardness measurements were used to determine strain hardening patterns for the various die geometries (Figure 13). The compressive yield strength of 90 Cu - 10 NaCl samples was determined as a function of matrix hardness (Figure 20). Based on these two types of data, yield strength can be determined as a function of position in the extrusion.

The yield strength-sample position data can not be readily analyzed mathematically. Consequently, an average yield strength value was used for the calculations. The stress profiles plotted in the results section are for the stress component divided by the average yield strength. The actual stress could be obtained by multiplying the plotted values by the actual yield stress for the position being considered. However, this correction was not made since the stress profiles were not believed to be accurate.

The ram pressure value used for the calculations was the extrapolated ram pressure (Chapter II - Section D-2). The extrapolation was made to eliminate the effects of sliding wall friction between the billet and chamber.

3. Ram Pressure as a Stress Index

Since an accurate determination of the stress components was not obtained, ram pressure was used as a stress level index. As the ram pressure increases, the magnitude of the stress components increases.

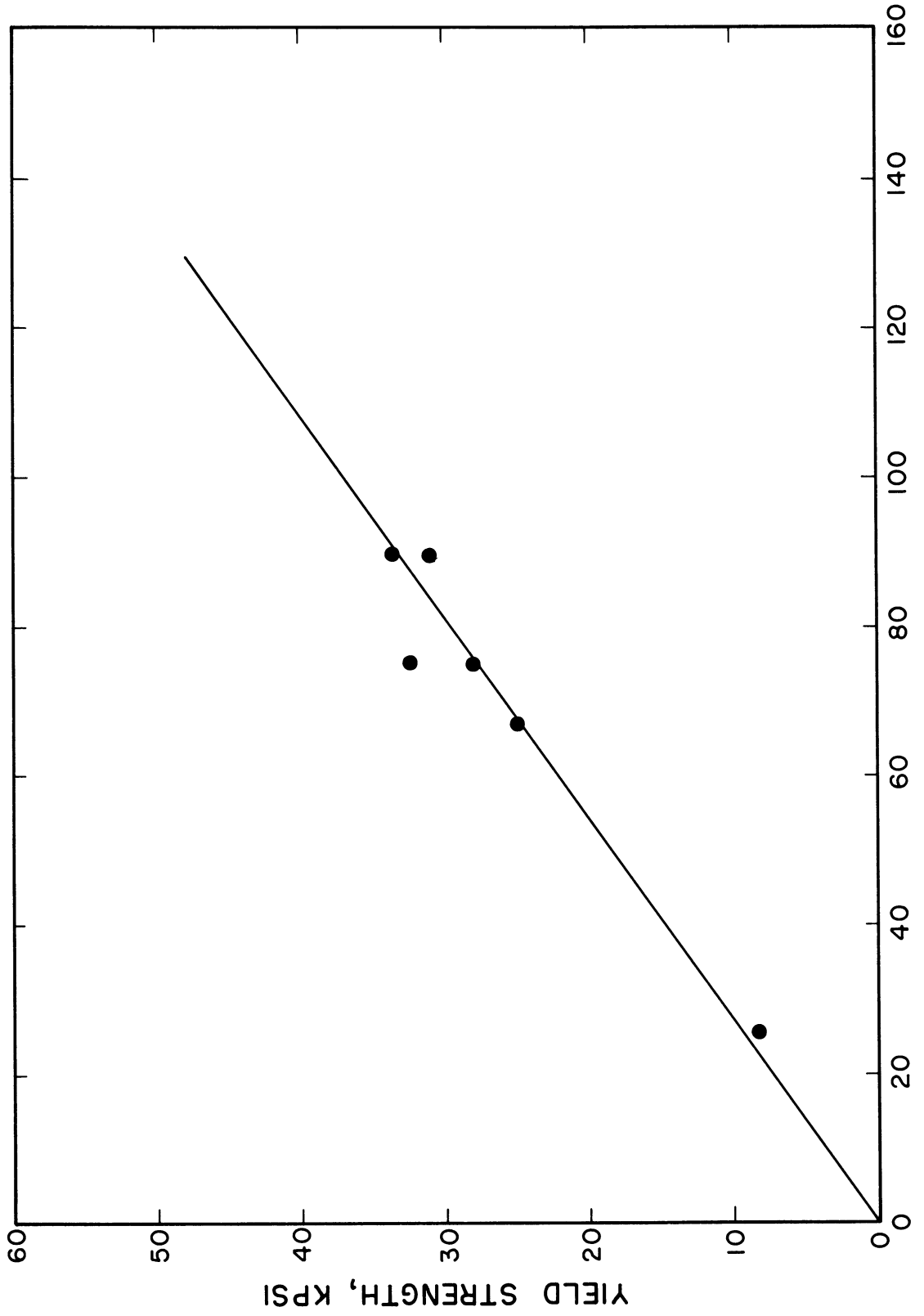

Figure 20. Compressive Yield Strength versus Matrix Hardness for 90 Cu - 10 NaCl Samples.

However, for a fixed die and coefficient of friction, the stress distribution would be unchanged. Consequently, ram pressure is a good index of the relative stress levels acting on the inclusions.

CHAPTER V

EXPERIMENTAL RESULTS

The experimental results will be discussed under the following headings:

A. Strain Hardening Patterns.

B. Flow Patterns.

C. Calculated Stress Distributions.

D. Plastic Deformation and Fracture.

E. Effects of Parameters on Inclusion Deformation.

A. Strain Hardening Patterns

Strain hardening patterns for various reductions and included die angles are presented in Figures 21 and 22. The lines of constant hardness were determined for low oxygen copper. Rates of strain hardening can be estimated from the distance between the various constant hardness lines. The right side of each figure shows lines through the experimentally determined points while the left side of each figure has the lines smoothed out to show the more probable constant hardness profiles.

The following observations can be made from the strain hardening patterns:

1. As the die angle increases, (a) the strain hardening patterns become more complex, (b) regions of softer material begin to occur near the die-container junction, and (c) the maximum hardness increases in the region of the die lips.
2. Most of the strain hardening occurs before the sample enters the die.
3. Some strain hardening occurs near the container walls.

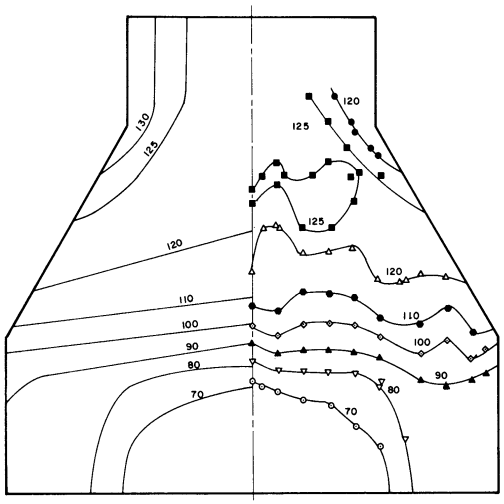

a) 60° die

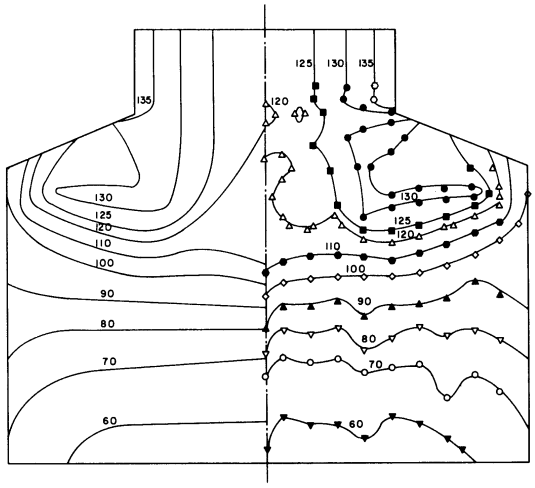

b) 135° die

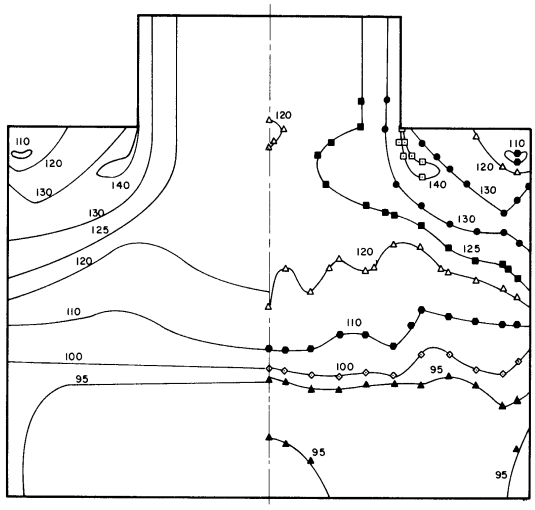

c) 180° die

Figure 21. Strain Hardening Patterns for 75 Per Cent Reduction Dies.

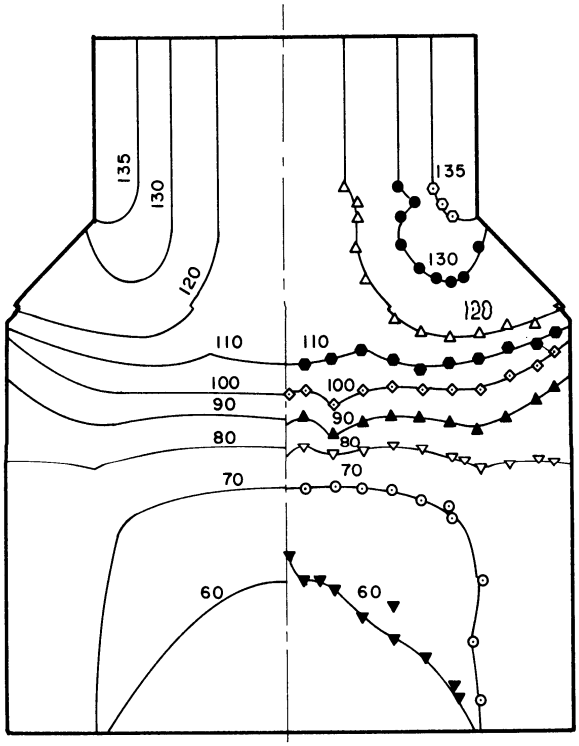

a) 55.6 per cent reduction die

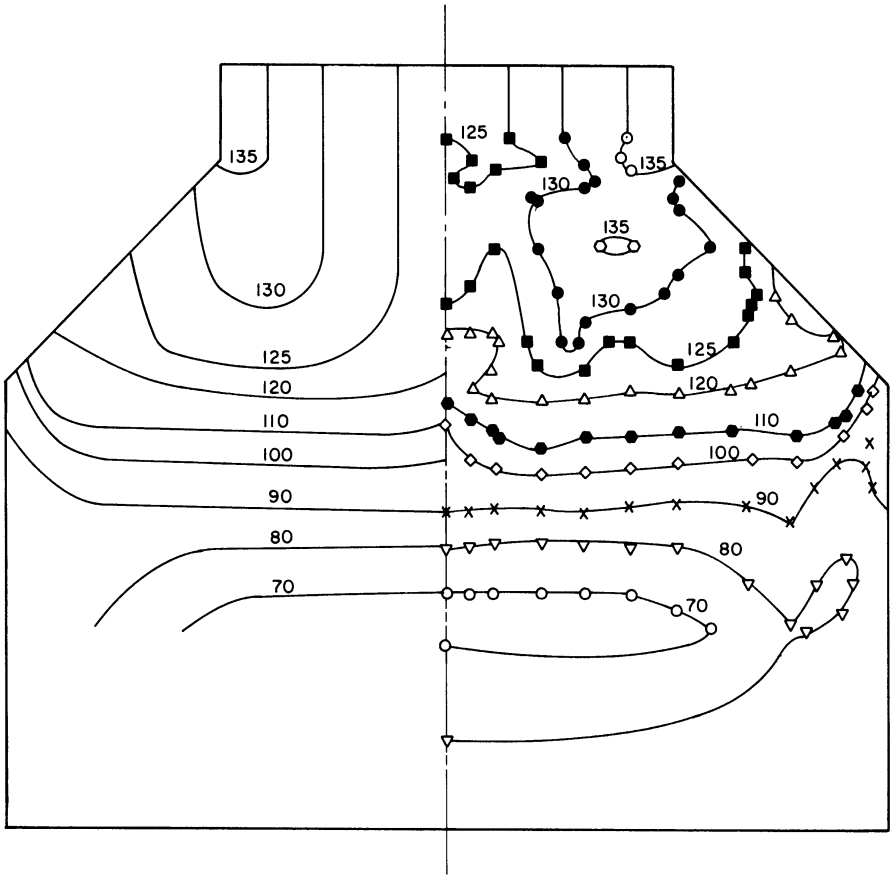

b) 75 per cent reduction die

Figure 22. Strain Hardening Patterns. 90° dies were used.

B. Flow Patterns

Photomicrographs illustrating inclusion deformation between the die lips are presented in Figure 23. These results are for 90 Cu - 10 NaCl samples which were extruded through a 90° included angle -75 per cent reduction die. The following observations can be made on the basis of these photomicrographs:

1. The inclusions are flattened somewhat before they enter the die. (The L/W ratio in the as-sintered samples was 0.536.)
2. Most of the deformation occurs in the region of a line normal to the die wall and originating at the die lips (line AB).
3. Lines drawn parallel to the long axes of the inclusions are not directed toward the virtual apex of the cone formed by extending the die lips.

Inclusion shapes in an extruded 90 Al - 10 NaCl sample are shown in Figure 24. A 180° included angle -75 per cent reduction die was used. A longitudinal sample along a symmetry plane is shown in Figure 24(a). As the sample surface is approached, the inclusion L/W ratio is observed to increase. Numerical data illustrating L/W profiles across various samples will be presented in section E of this chapter. A section normal to the extrusion direction is shown in Figure 24(b). As the sample is traversed from surface to center, the inclusion length in the circumferential direction does not change appreciably.

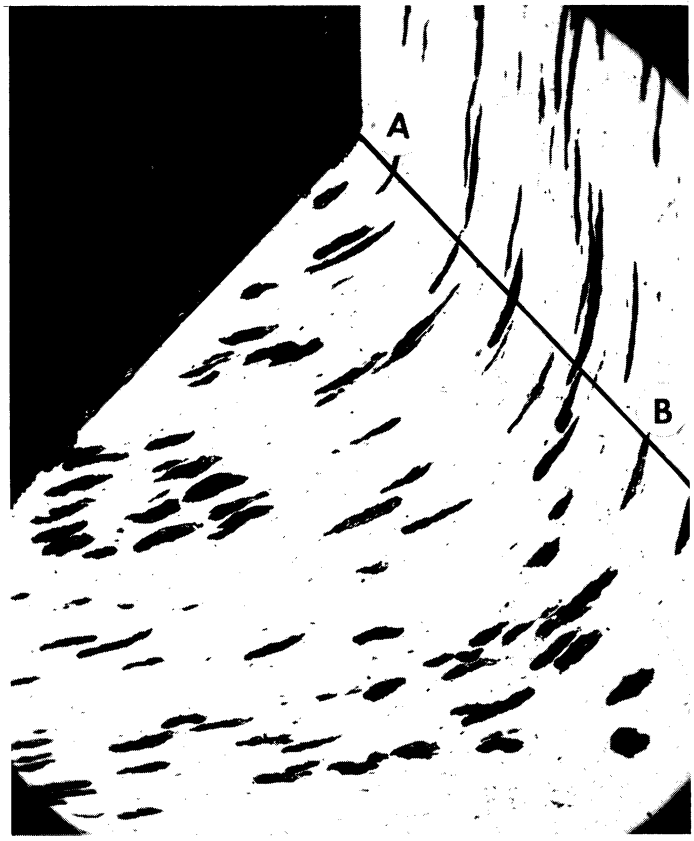

a) 0.081 mm inclusions in a copper matrix.

b) 0.214 mm inclusions in a copper matrix.

Figure 23. Microsturctures Illustrating Inclusion Flow between the Die Lips. 90° -75% reduction dies were used. 37.5X.

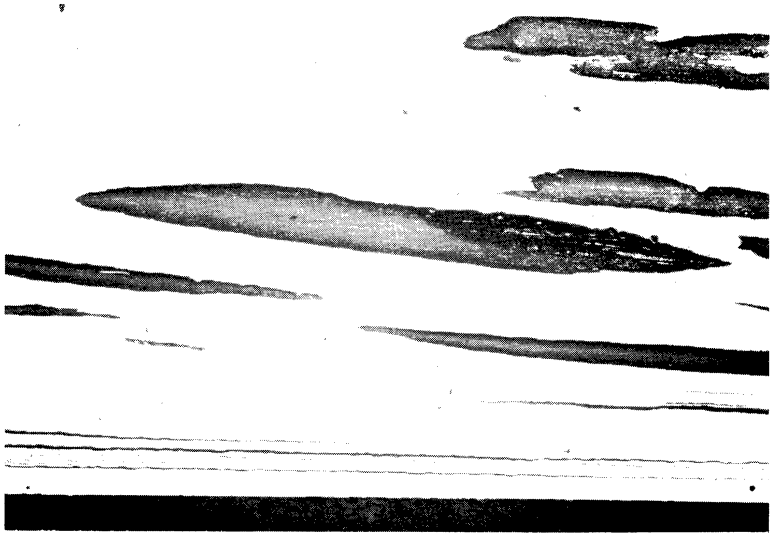

a) Section parallel to the extrusion direction.

b) Section normal to the extrusion direction.

Figure 24. Microstructures Illustrating Inclusion Deformation in an Extruded Sample.

C. Calculated Stress Distribution

Stress distributions calculated from the modified stress analysis are presented in Figures 25 through 29. The yield strength values used for the calculations are listed with each figure.

Figure 25 shows the results obtained for the extrusion of a 90 Pb - 10 NaCl sample through a 90° - 75 per cent reduction die. These results are significant since this sample does not strain harden during extrusion. Figure 26 shows the results obtained for a 90 Cu - 10 NaCl sample extruded through the same die where the average value of the initial and final yield strengths was used in the calculations. The results obtained from these two calculations are almost identical.

The effect of die angle on stress distribution can be observed in Figures 26 through 28. An average yield strength value was used for these calculations. As the die angle increases, the difference between the surface and center values of the stress components increases. The effect of using the final value of the yield strength for the calculations is shown in Figure 29. For all of the calculations, the shear stress reaches $\sigma_o/\sqrt{3}$ well inside the samples.

D. Plastic Deformation and Fracture

Plastically deformed and fractured inclusions are shown in Figure 30. Typical plastically deformed inclusions are shown in Figure 30(a). Regions where local sections of the inclusion have slipped over each other can be observed. When fracture occurs during deformation, the inclusions have the appearance shown in Figure 30(b). Crystallographic

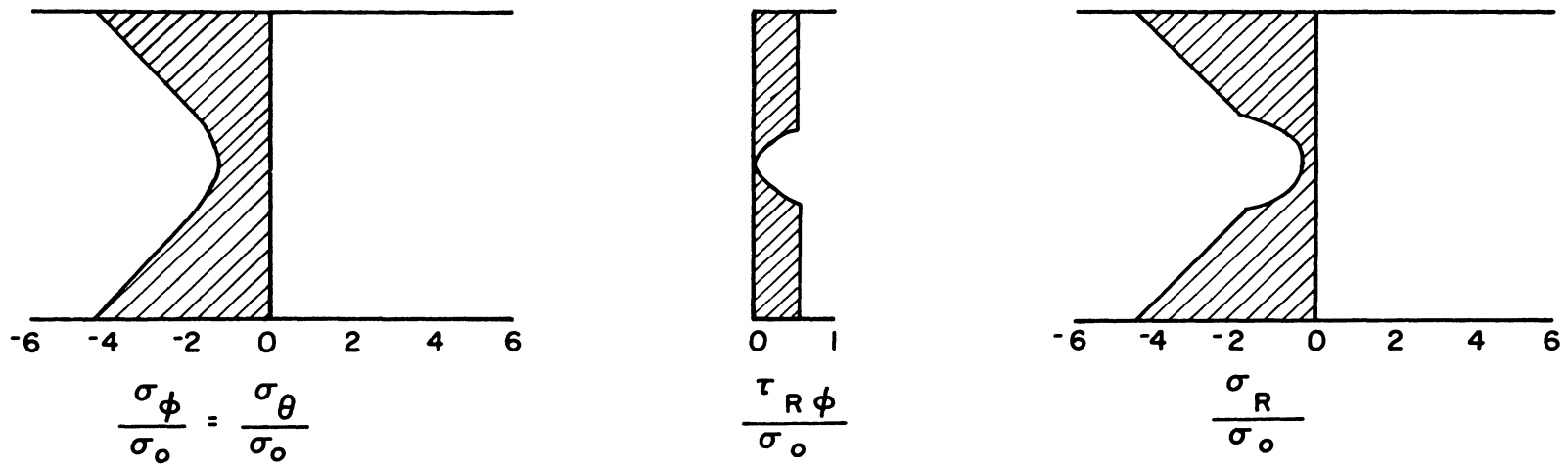

a) Stress distribution at the die entrance

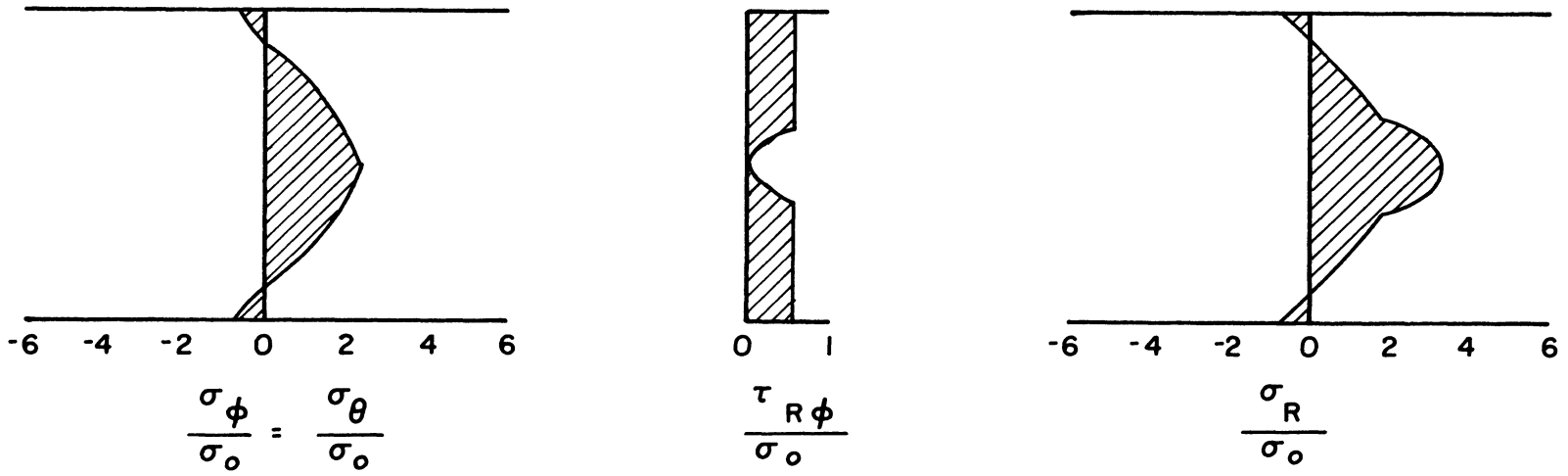

b) Stress distribution at the die exit

Figure 25. Calculated Stress Distribution for a 90 Pb - 10 NaCl Sample Extruded through a 90° - 75 Per Cent Reduction Die. $\bar{\sigma}_o$ = 1,245 psi.

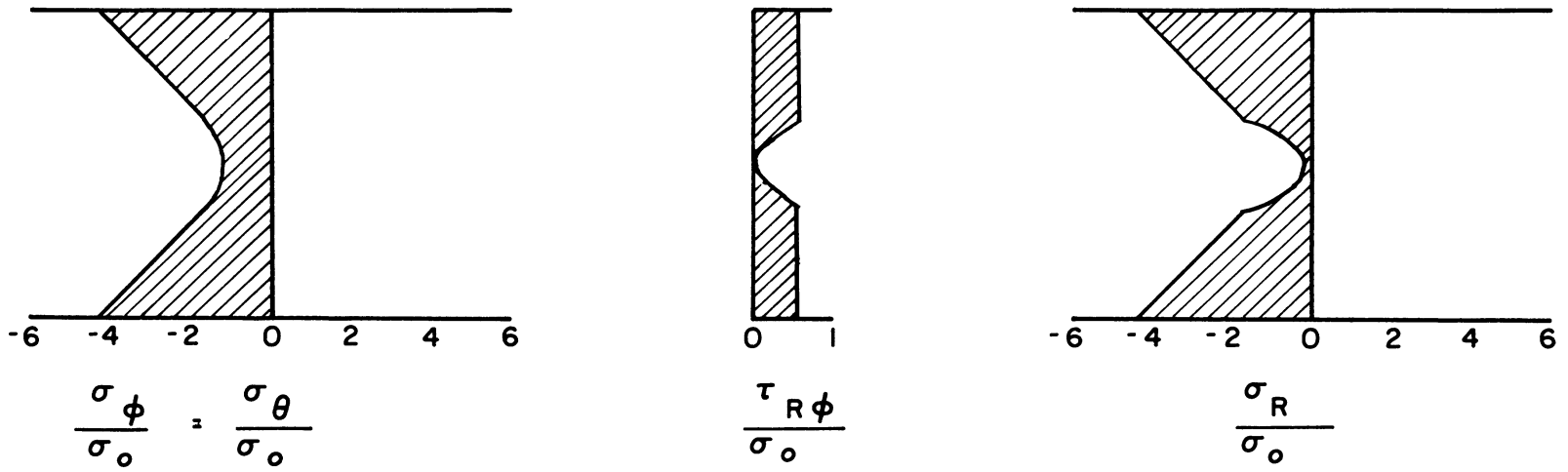

a) Stress distribution at the die entrance

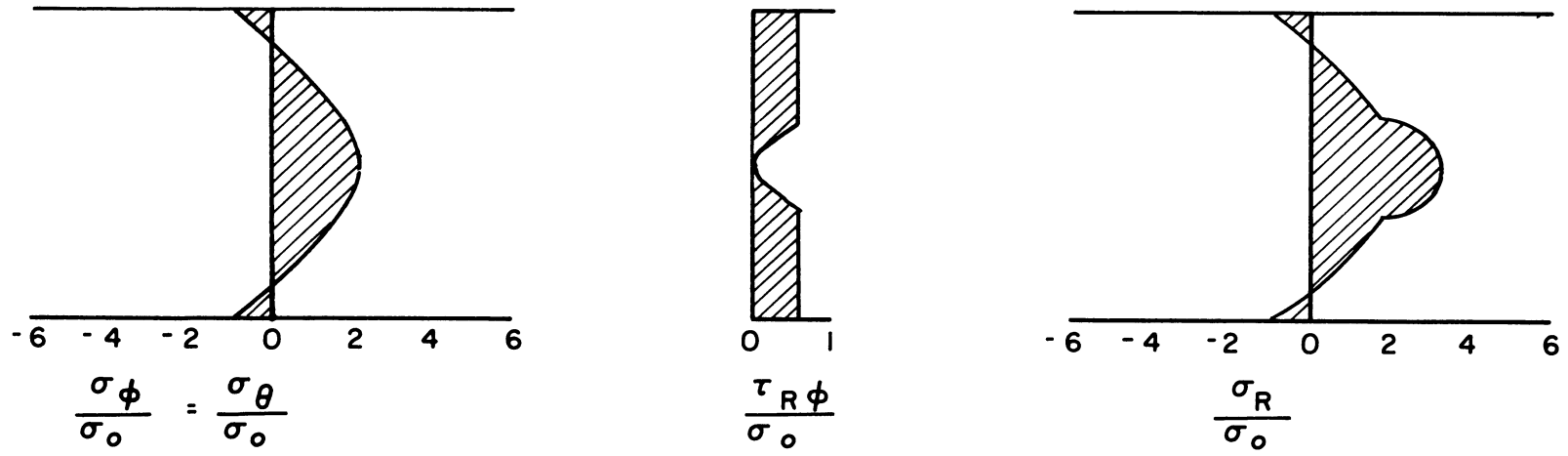

b) Stress distribution at the die exit

Figure 26. Calculated Stress Distribution for a 90 Cu - 10 NaCl Sample Extruded through a 90° - 75 Per Cent Reduction Die. $\overline{\sigma}_o$ = 27,150 psi.

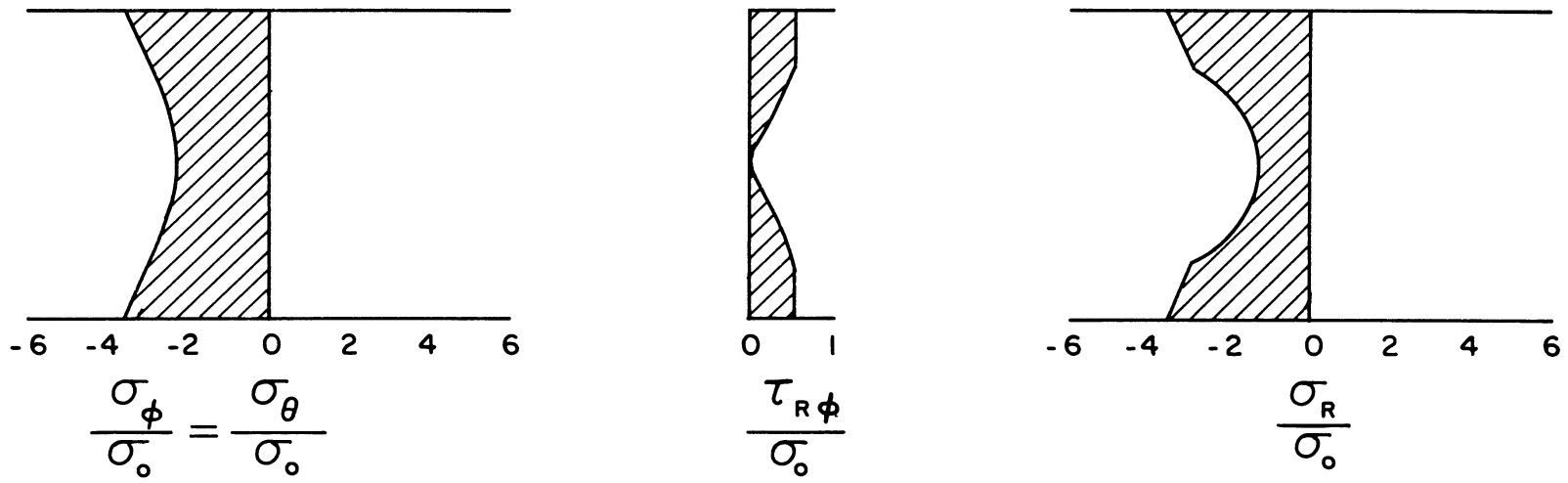

a) Stress distribution at the die entrance

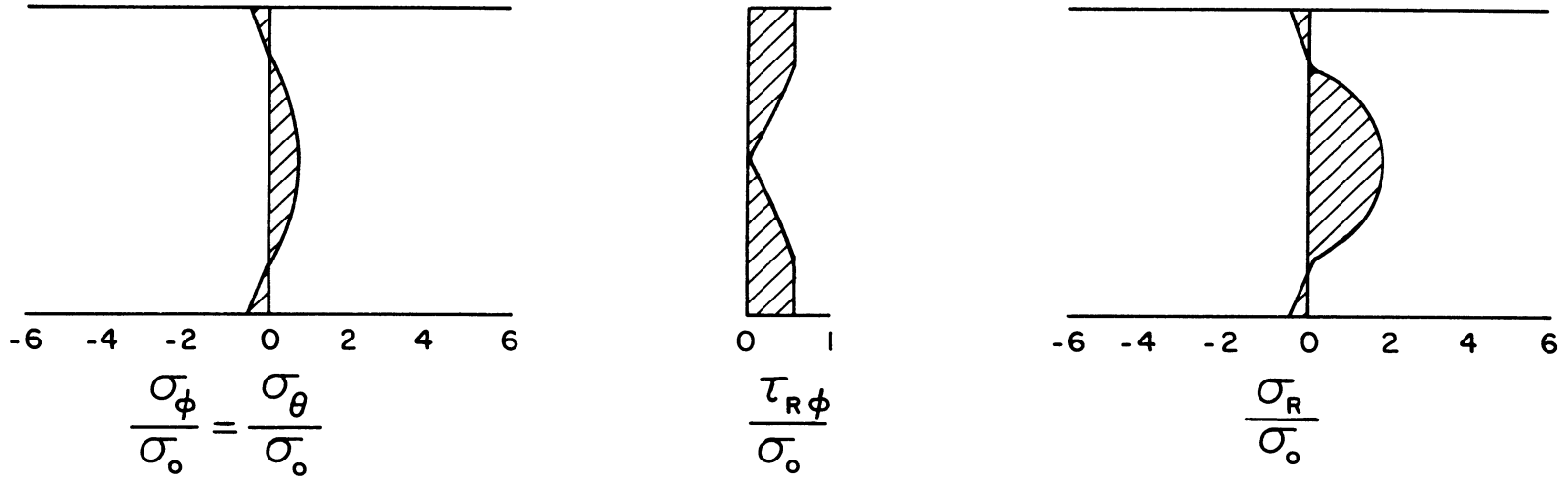

b) Stress distribution at the die exit

Figure 27. Calculated Stress Distribution for a 90 Cu - 10 NaCl Sample Extruded through a 60° - 75 Per Cent Reduction Die. $\bar{\sigma}_o$ = 26,980 psi.

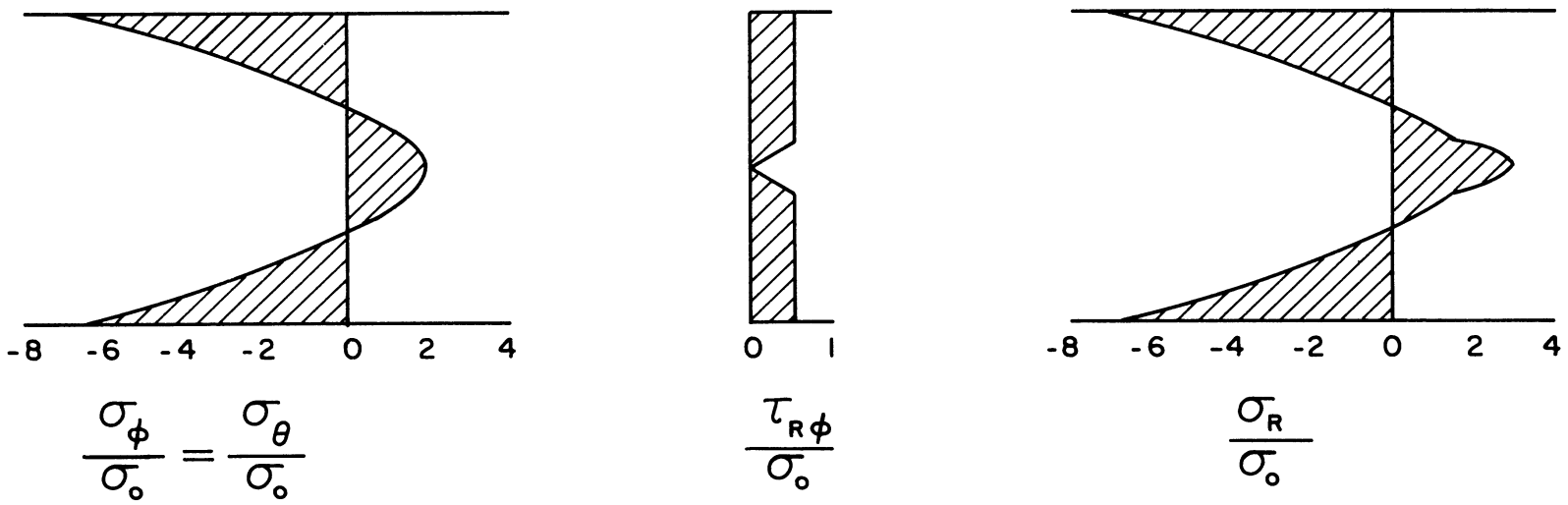

a) Stress distribution at the die entrance

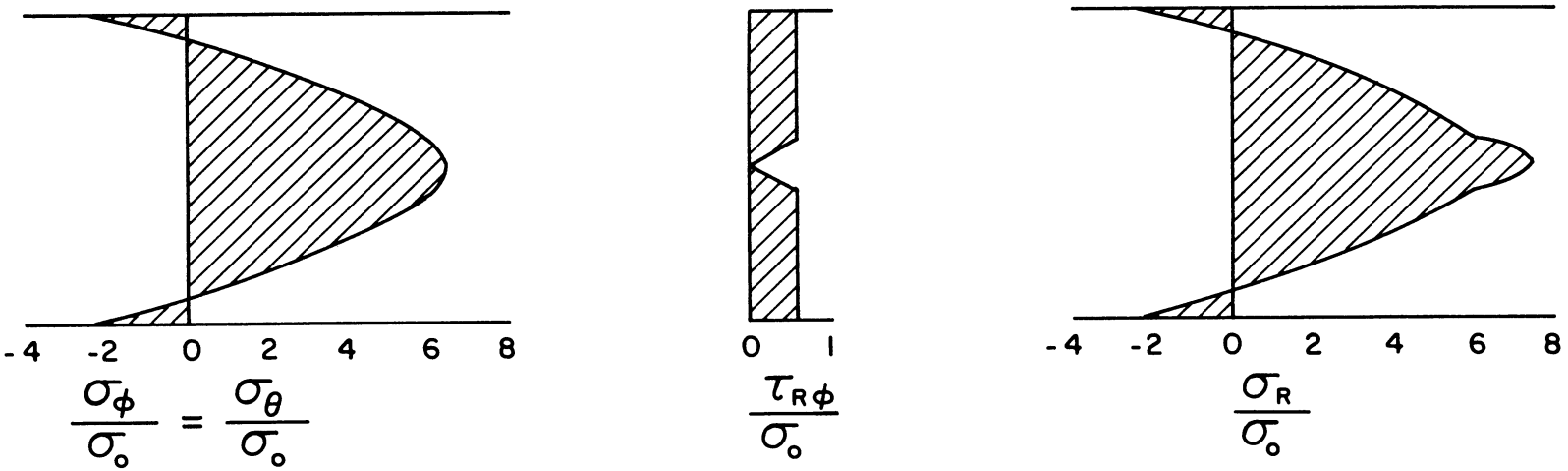

b) Stress distribution at the die exit

Figure 28. Calculated Stress Distribution for a 90 Cu - 10 NaCl Sample Extruded through a 135° - 75 Per Cent Reduction Die. $\bar{\sigma}_o$ = 25,950 psi.

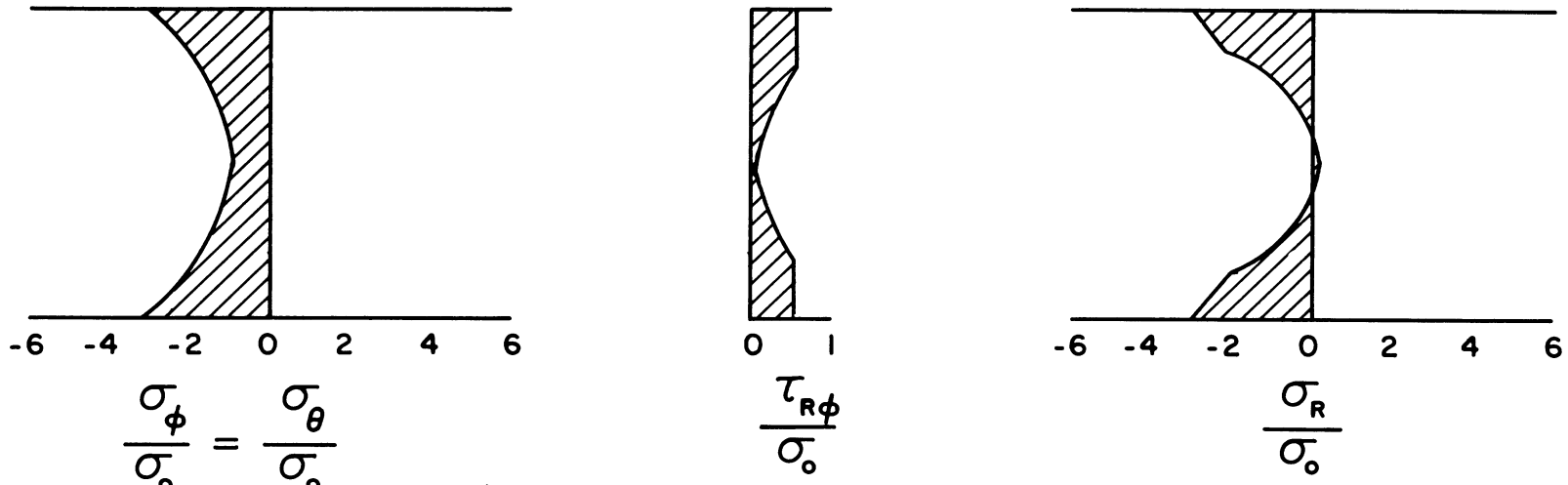

a) Stress distribution at the die entrance.

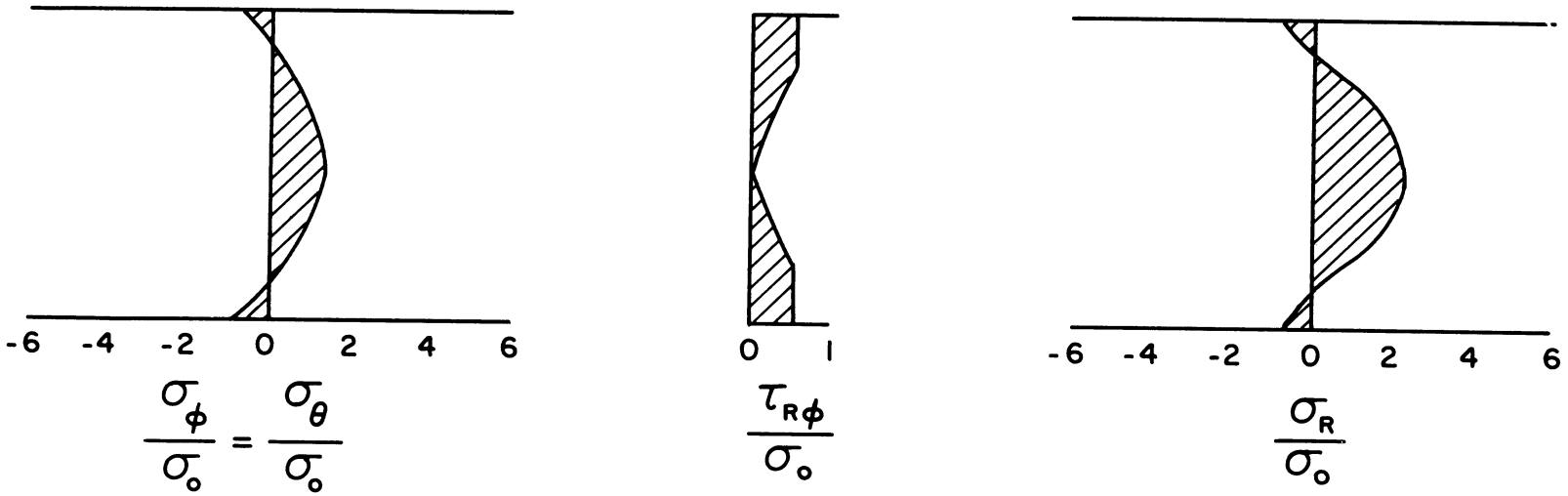

b) Stress distribution at the die exit

Figure 29. Calculated Stress Distribution for a 90 Cu - NaCl Sample Extruded through a 90° - 75 Per Cent Reduction Die. $\bar{\sigma}_o$ = 44,700 psi.

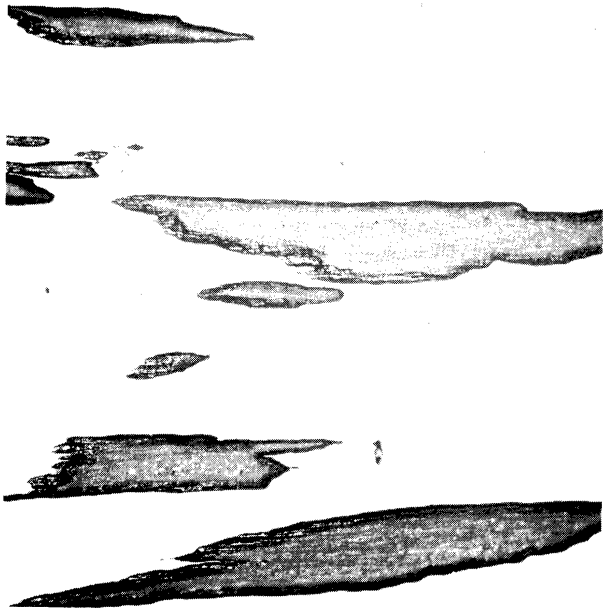

a) Plastic deformation of inclusions in a 90 Al - 10 Cu sample. 37.5X.

b) Inclusion fracture during extrusion in a 90 Cu - 10 LiF sample. 37.5X.

Figure 30. Microstructures Illustrating Plastically Deformed and Fractured Inclusions. All samples were extruded through a 90° -75% reduction die.

fracture planes are observed, metal is occasionally forced between the fractured pieces of the inclusion, and some inclusion dispersion occurs. Internal cracks in the inclusions are rapidly etched by the alcohol used in polishing. Consequently, cracks can be readily observed when they occur.

It was felt desirable to investigate the effect of initial inclusion orientation on the final shape of the inclusion. To do this, cubic NaCl single crystals with known orientations were placed at the center of copper samples. The inclusions were oriented so that a [111], [110], or [100] inclusion direction was in the extrusion direction. Radiographs of the samples before and after room temperature extrusion are shown in Figure 31. The sample having the [100] orientation was not fully extruded and it cracked near the die entrance on removal from the die.

The original inclusion orientation is preserved during extrusion for the [111] and [110] samples while the [100] sample tends to rotate so that a [110] direction lines up with the extrusion direction. The amount of deformation for the [111] and [110] samples is about the same.

E. Effects of Extrusion Parameters on Inclusion Deformation

In this section, the experimental data obtained as a function of various extrusion parameters will be presented graphically. The experimental ram pressure and L/W data are listed in tabular form in Appendix C while the experimental hardness data are listed in tabular form in Appendix D. The following plots are used to illustrate the

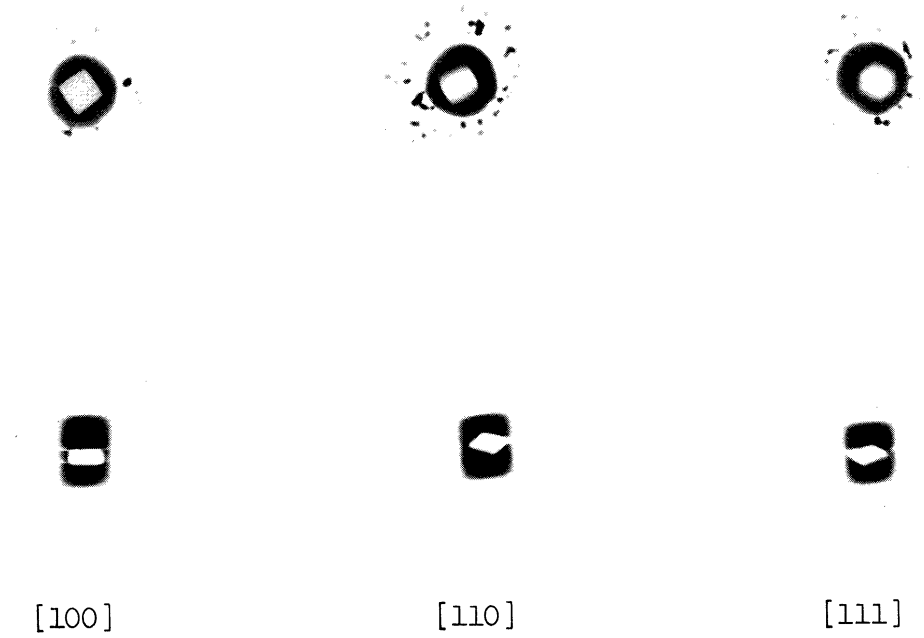

[100] [110] [111]

a) Before extrusion.

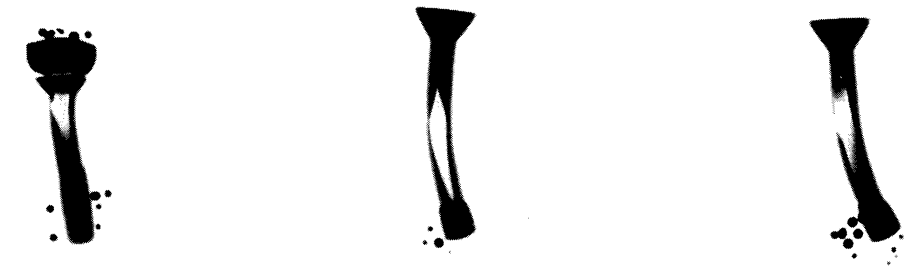

[100] [110] [111]

b) After extrusion.

Figure 31. Radiographs Illustrating the Effect of Inclusion Orientation in Inclusion Deformation. The black dots were caused by lead shot in the clay used to position the samples.

effects of the parameters:

1. L/W ratio vs. variable.

2. $\frac{\sum_{i}(L/W)_i A_i}{A_t}$ vs. variable.

3. Ram pressure vs. variable.

4. $\frac{\sum_{i}(L/W)_i A_i}{A_t}$ vs. ram pressure.

In general, the fourth type of curve is a consequence of the factors governing the second and third types of curves.

1. Effect of Die Angle

(Data and figures: 75 per cent reduction-variable angle dies, 90 Cu - 10 NaCl samples, Figures 32 through 36.)

As the die cone angle increases, the following effects are observed:

1. There is a rapid increase in the L/W ratio near the surface of the sample. The L/W ratio near the center of the samples does not change significantly (Figure 32).
2. The amount of inclusion deformation increases (Figure 33).
3. The ram pressure increases (Figure 34).

The bulk L/W value for the sample is approximately 8/1. With the L/W correction for density and original L/W ratio, the inclusion L/W ratios are above 8/1 for all positions and die cone angles. Consequently, the NaCl inclusions are the more ductile phase.

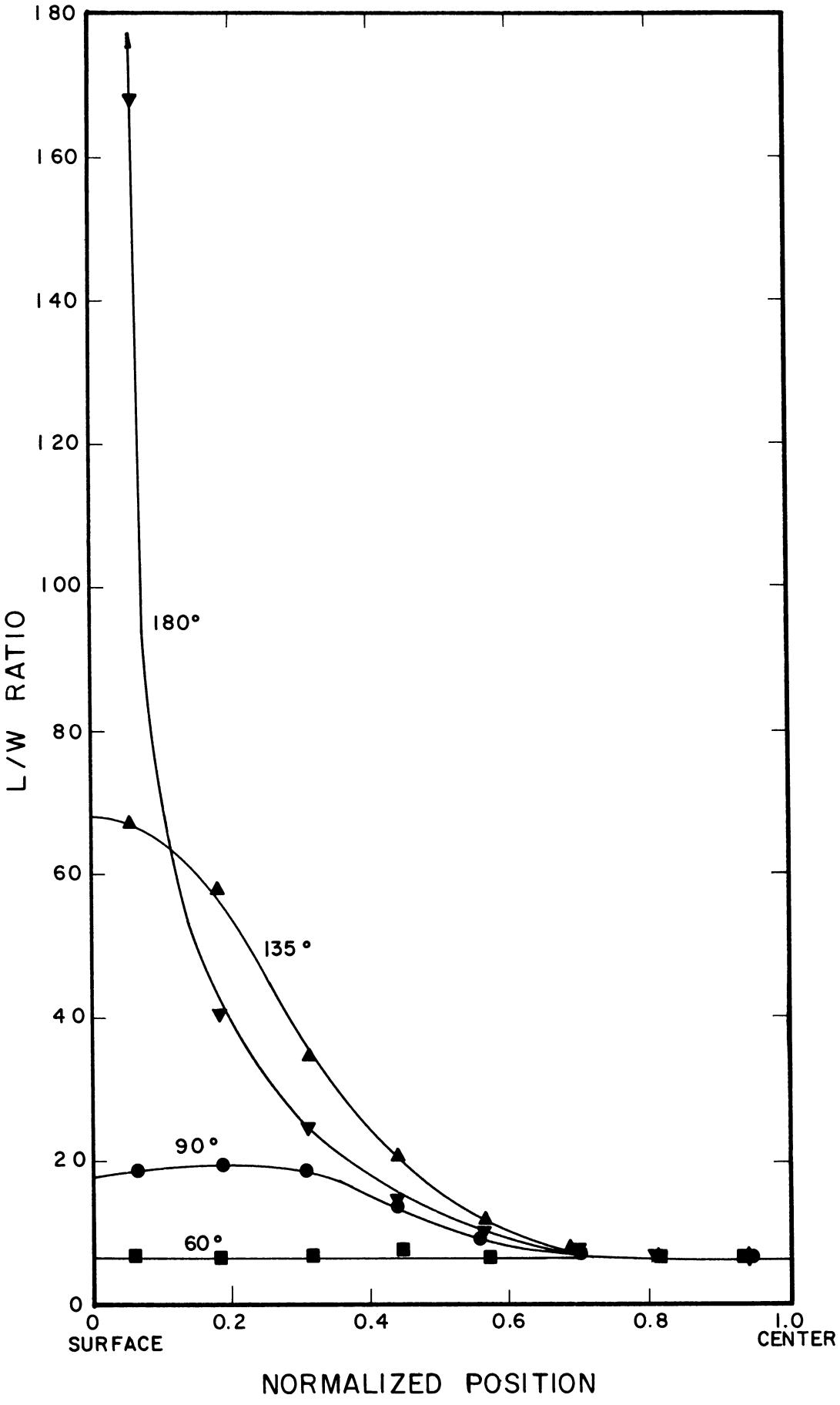

Figure 32. L/W Traverses for Die Angle Study Samples.

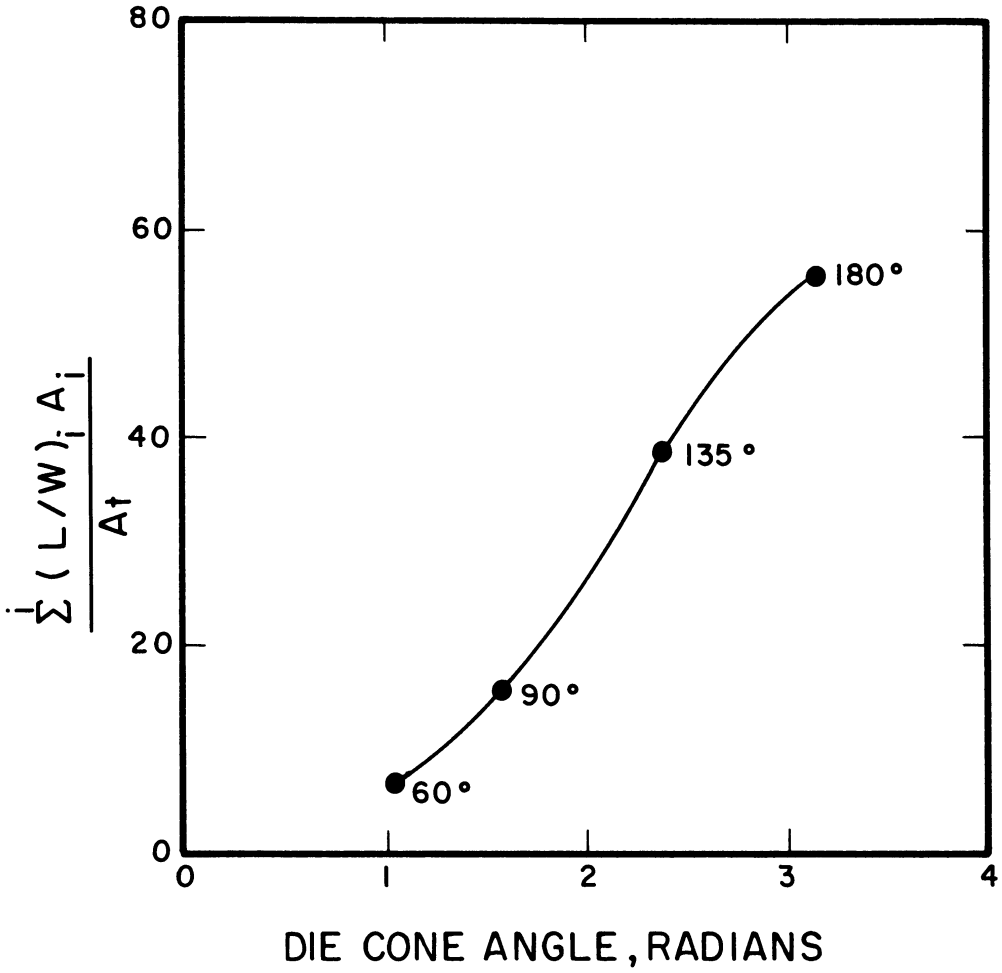

Figure 33. Inclusion Deformation versus Die Angle.

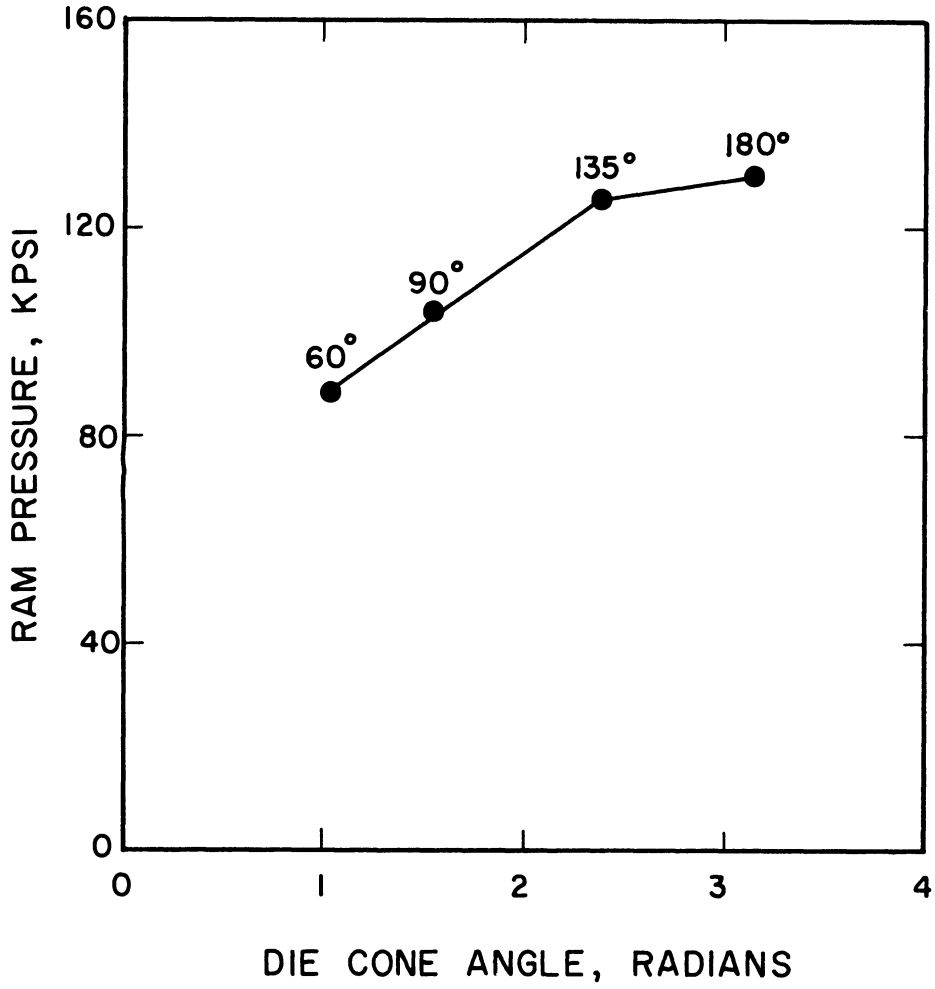

Figure 34. Ram Pressure versus Included Die Angle.

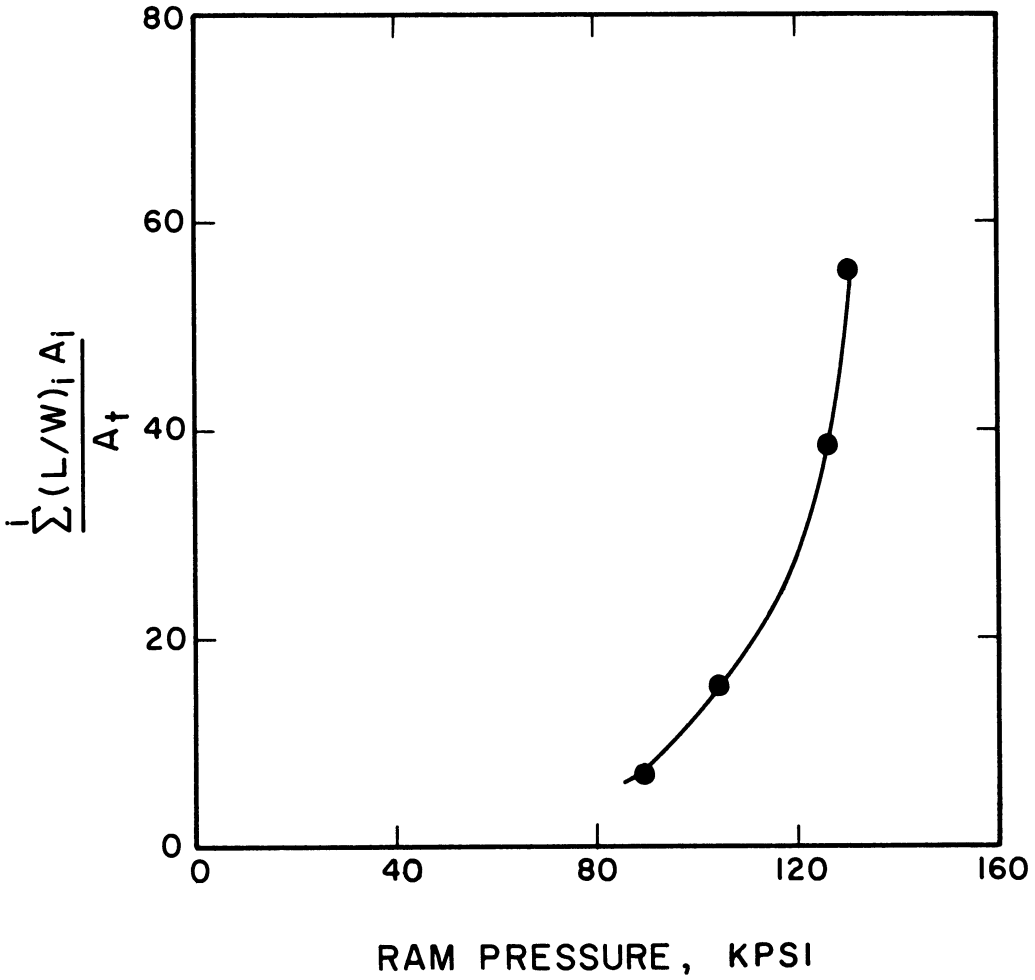

Figure 35. Inclusion Deformation - Ram Pressure Relationship for Die Angle Study Samples.

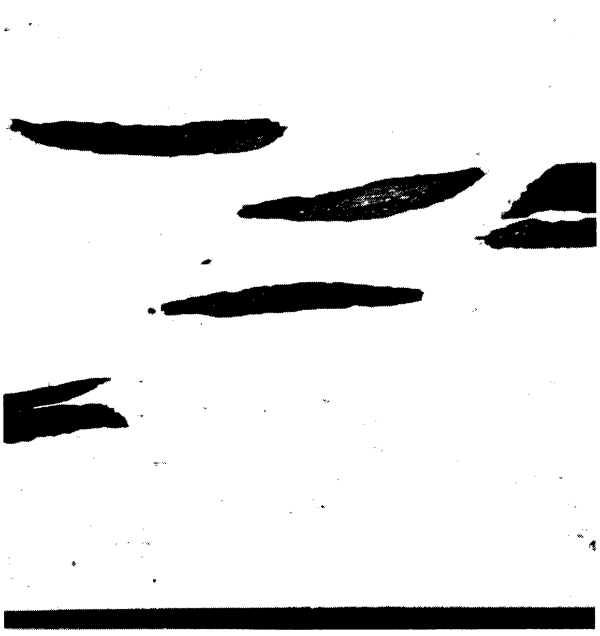

a) Die angle: 60°.

b) Die angle: 90°.

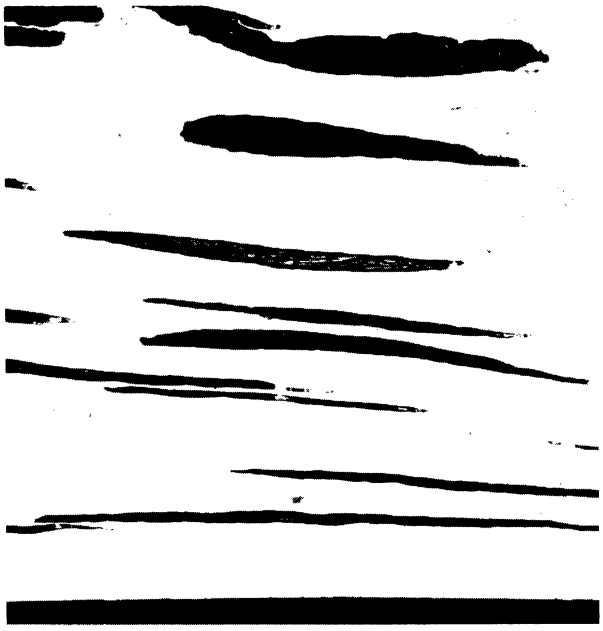

c) Die angle: 135°.

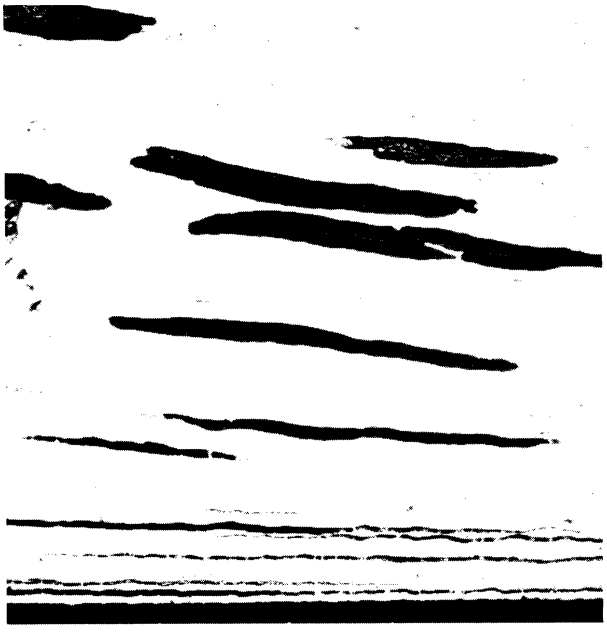

d) Die angle: 180°.

Figure 36. Microstructures Illustrating the Effect of Die Angle on Inclusion Deformation. Samples: 90 Cu - 10 NaCl. Die: 75% reduction. 37.5X.

2. Effect of Per Cent Reduction in Area

(Data and figures: 90° - variable reduction dies, 90 Cu - 10 NaCl samples, Figures 37 through 41)

As the per cent reduction in area increases, the following effects are observed:

1. The inclusion L/W ratio increases for all positions across the sample (Figure 37).
2. Both the amount of sample deformation and the amount of inclusion deformation increase. The curves for inclusion deformation and bulk sample deformation have the same general shape (Figure 38).
3. The NaCl inclusions undergo more deformation than the matrix (Figure 38).
4. The ram pressure increases (Figure 39(a)).
5. The plot of ram pressure vs. log (A_i/A_f) is linear (Figure 39(b)).

3. Effect of Strain Rate

(Data and figures: 90° - 75 per cent reduction dies, 90 Cu - 10 NaCl samples, Figures 42 through 46)

As the strain rate (ram velocity) increases, the following effects are observed:

1. The amount of NaCl deformation increases (Figures 42 and 43).
2. Ram pressure increases (Figure 44(a)).
3. Log (ram pressure) is a linear function of log (ram velocity) (Figure 44(b)).

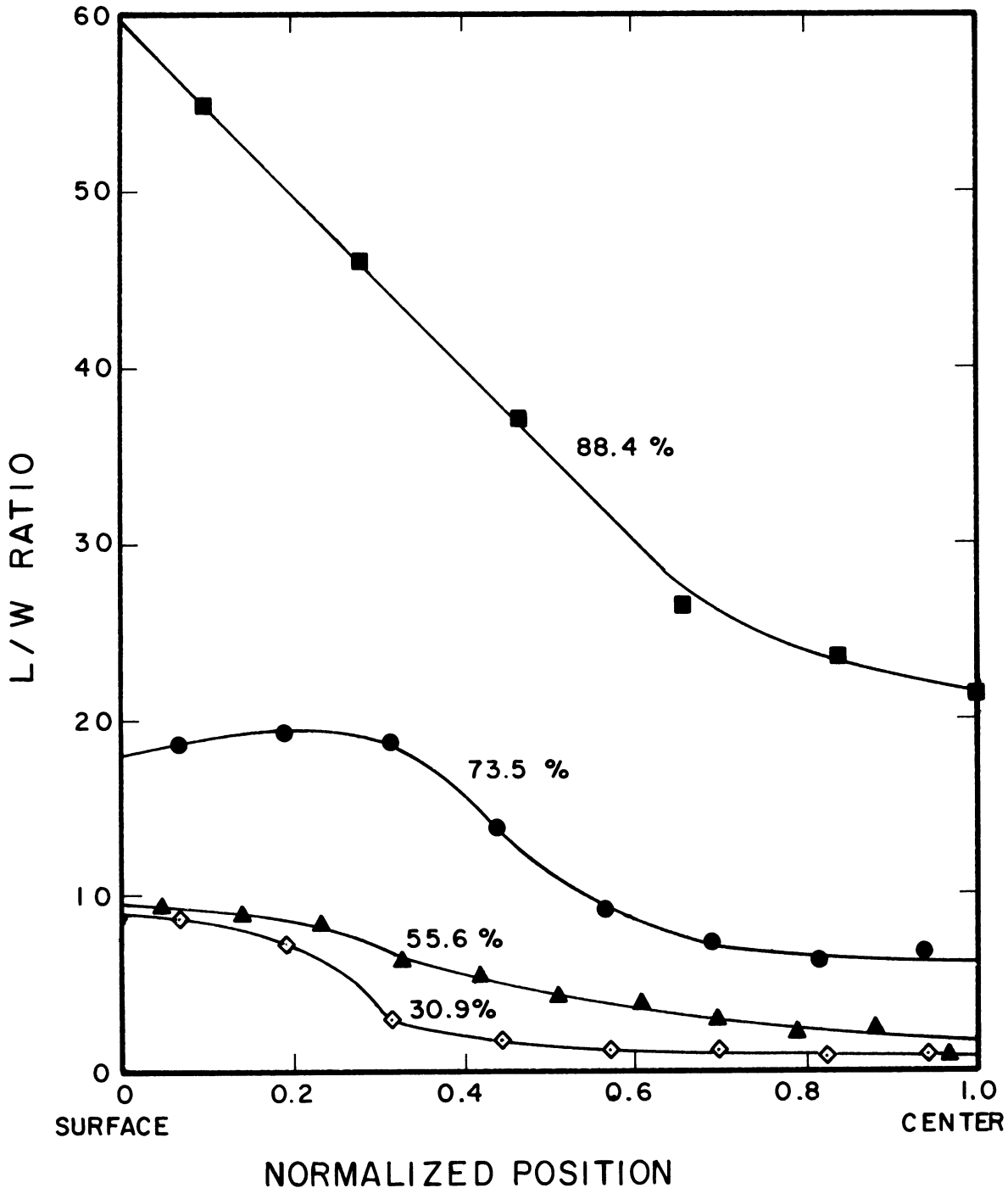

Figure 37. L/W Traverses for Per Cent Reduction in Area Study Samples.

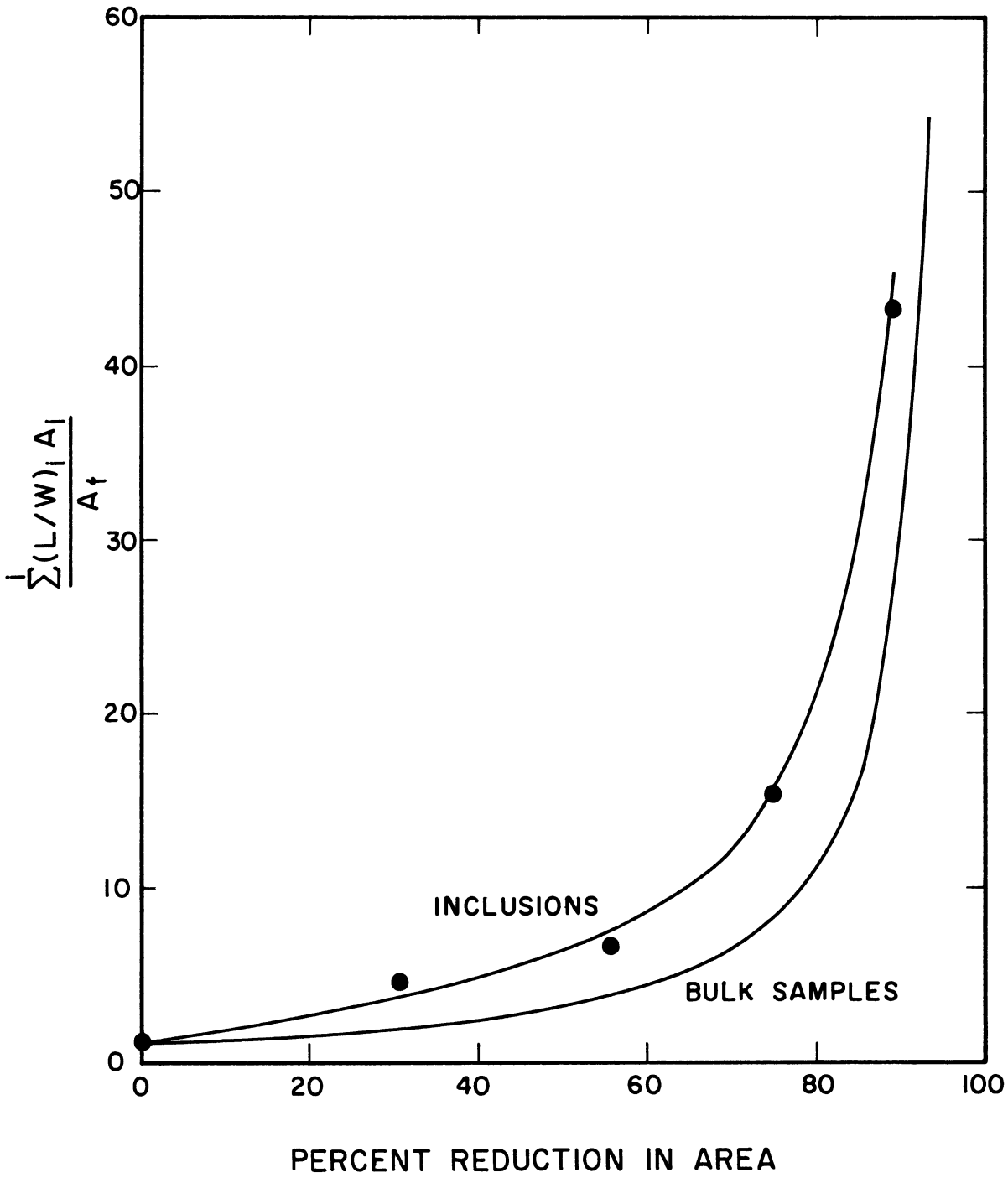

Figure 38. Inclusion Deformation versus Per Cent Reduction in Area.

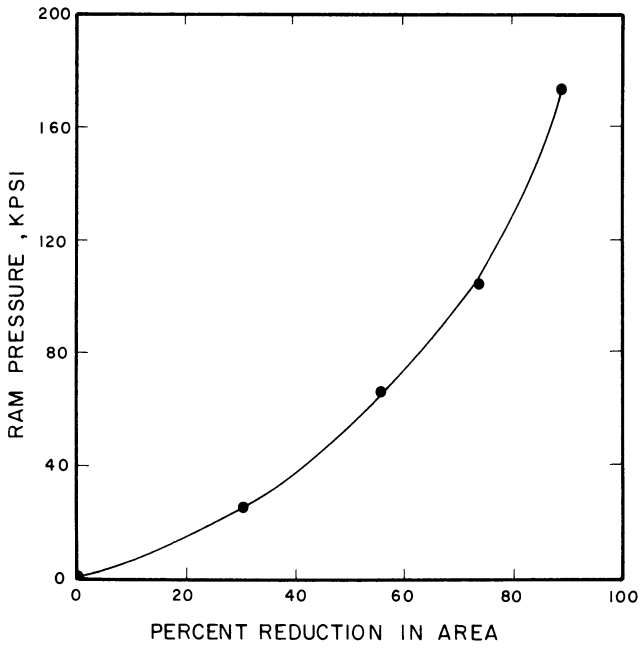

a) Ram pressure vs. per cent reduction in area

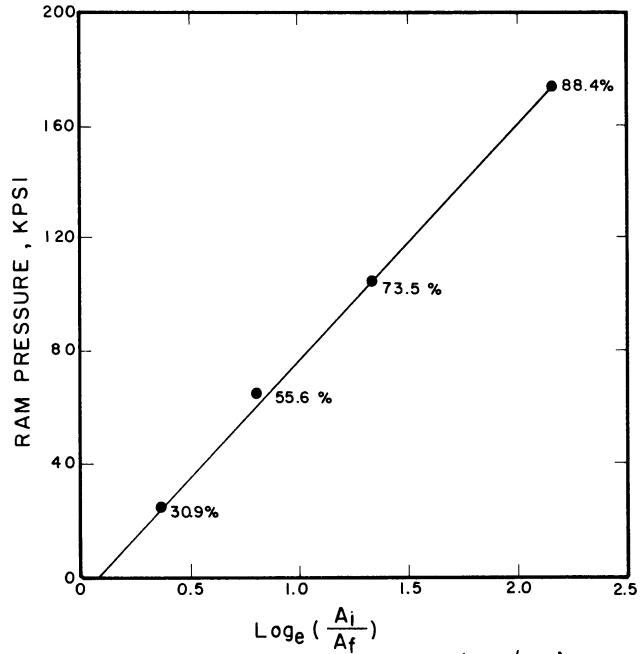

b) Ram pressure vs. $\log_e(A_i/A_f)$

Figure 39. Ram Pressure versus Per Cent Reduction in Area.

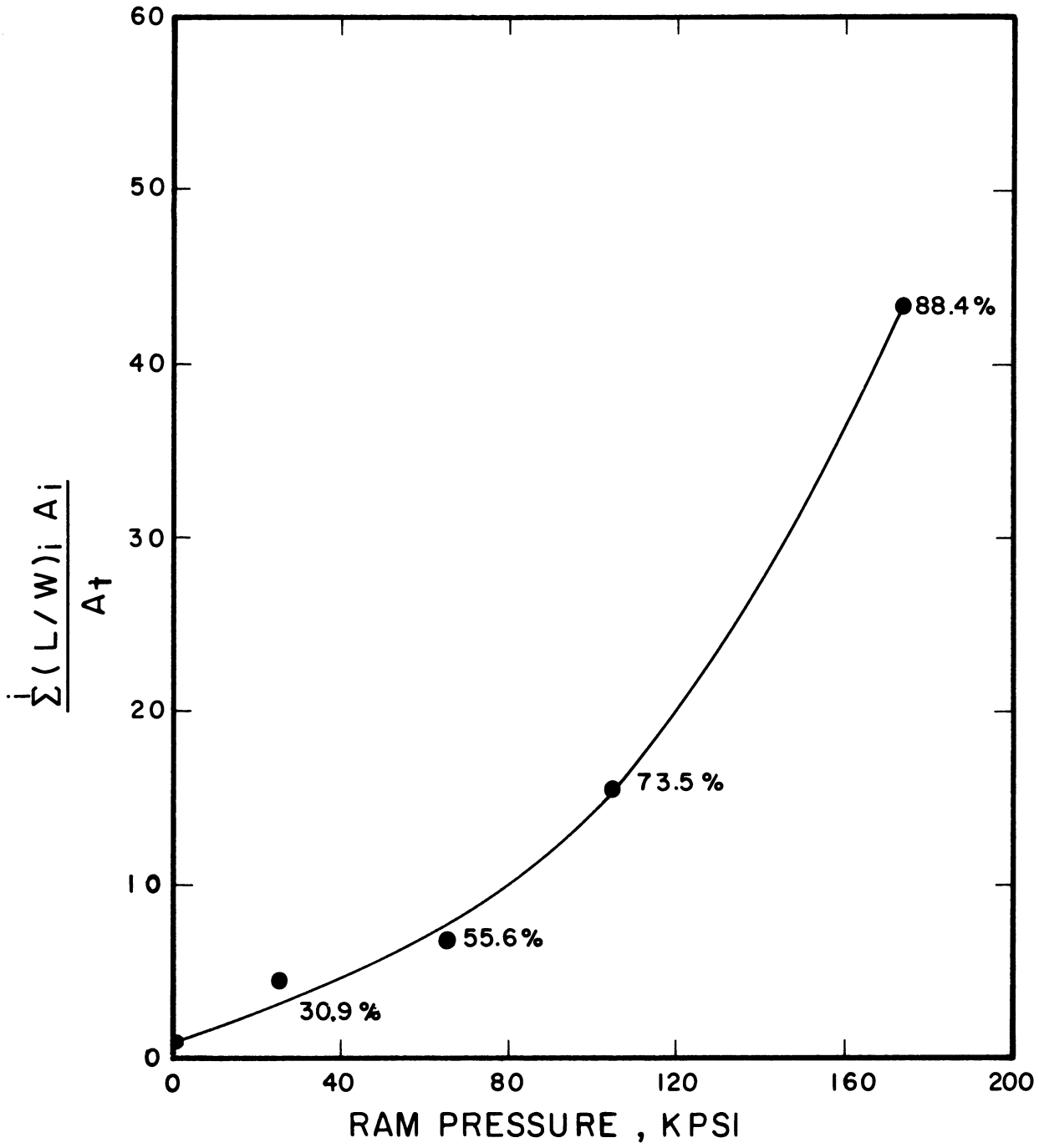

Figure 40. Inclusion Deformation - Ram Pressure Relationship for Per Cent Reduction in Area Samples.

a) Reduction in area: 30.9%.

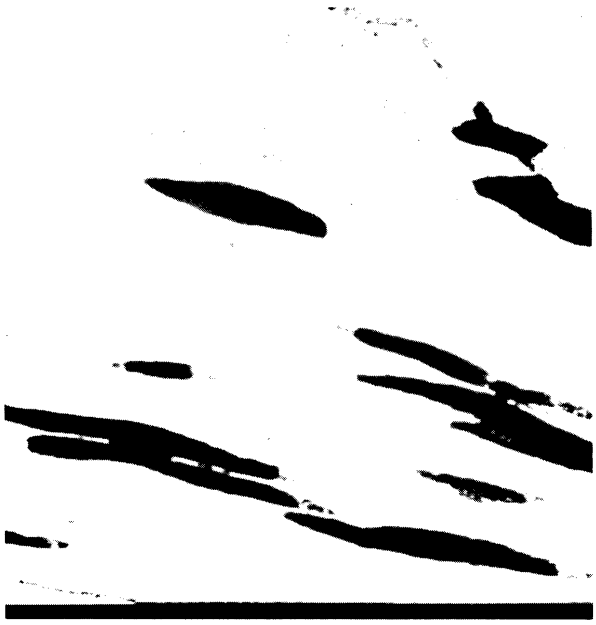

b) Reduction in area: 55.6%.

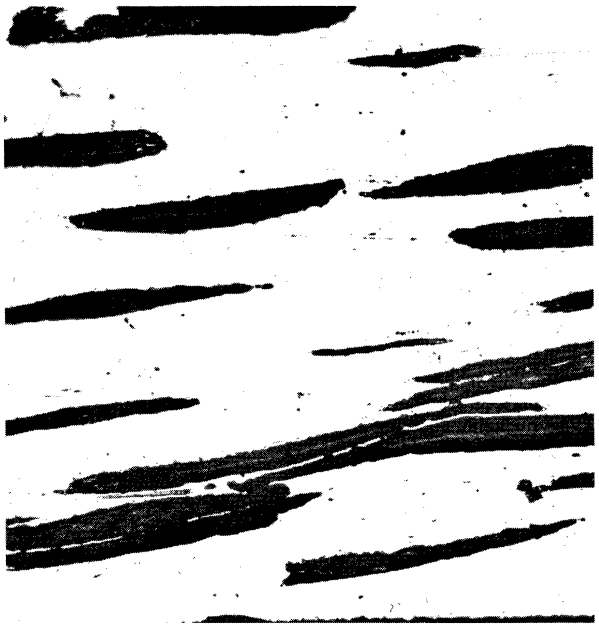

c) Reduction in area: 73.5%.

d) Reduction in area: 88.5%.

Figure 41. Microstructures Illustrating the Effect of Per Cent Reduction in Area on Inclusion Deformation. Samples: 90 Cu - 10 NaCl. Dies: 90°. 37.5X.

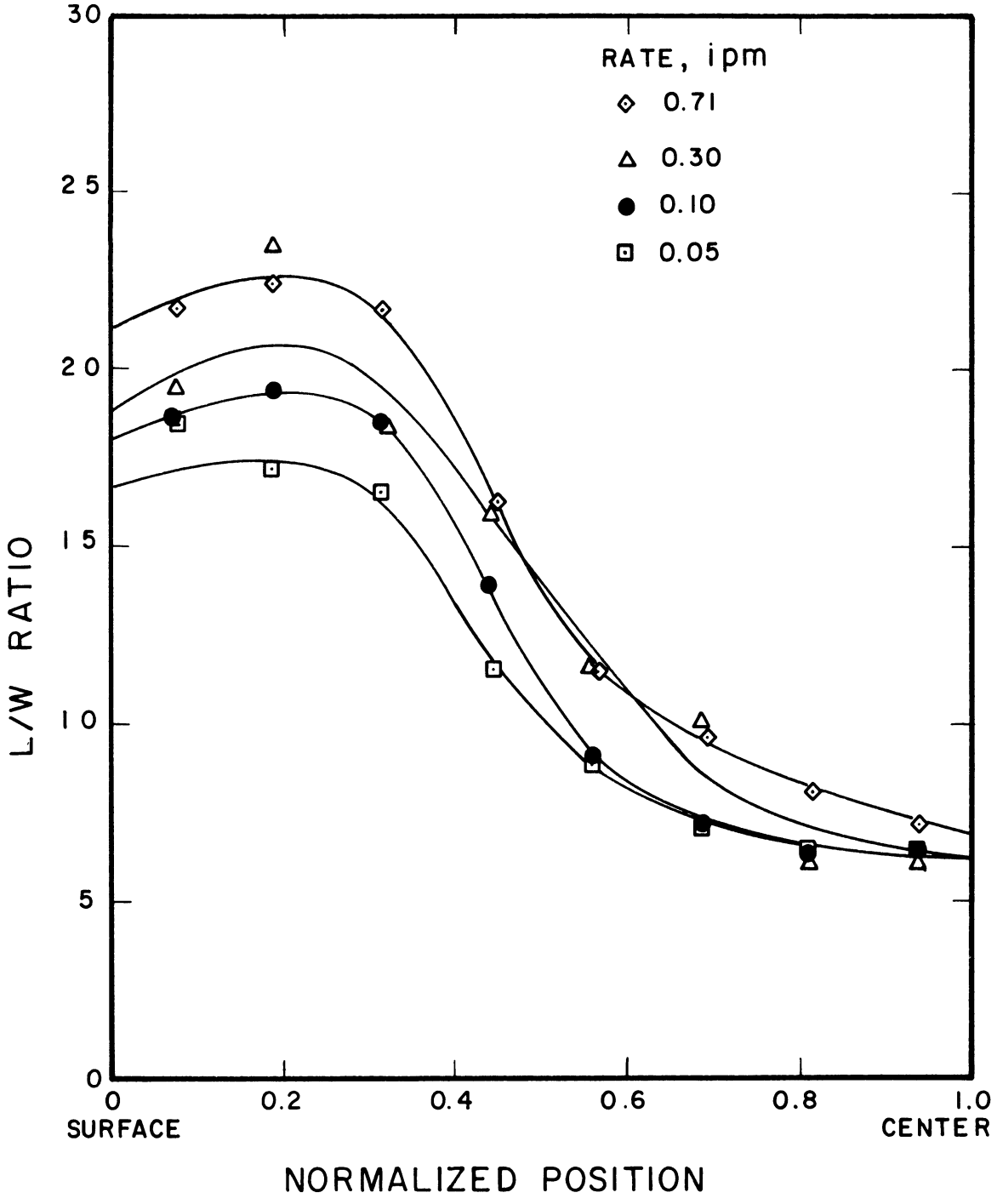

Figure 42. L/W Traverses for Strain Rate Study Samples.

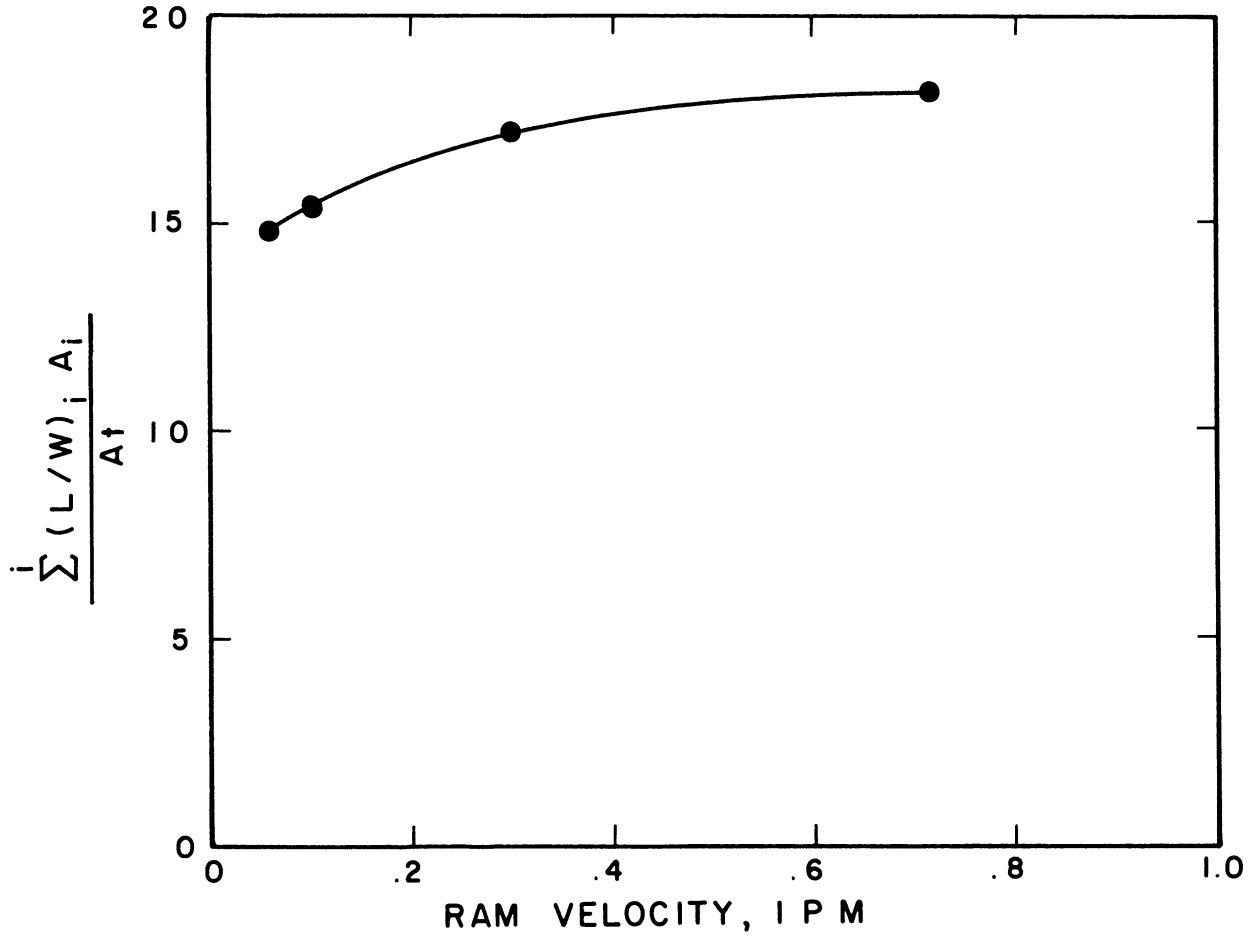

Figure 43. Inclusion Deformation versus Ram Velocity.

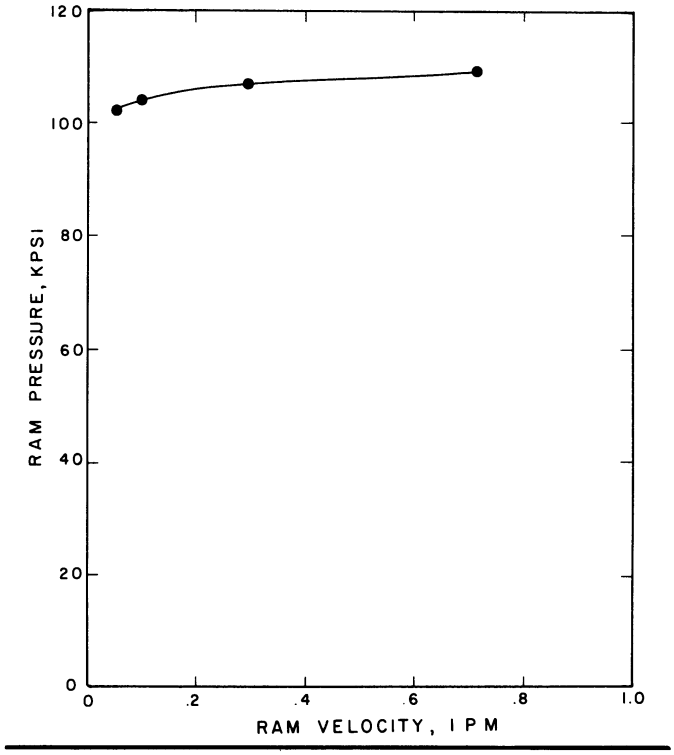

a) Ram pressure vs. ram velocity

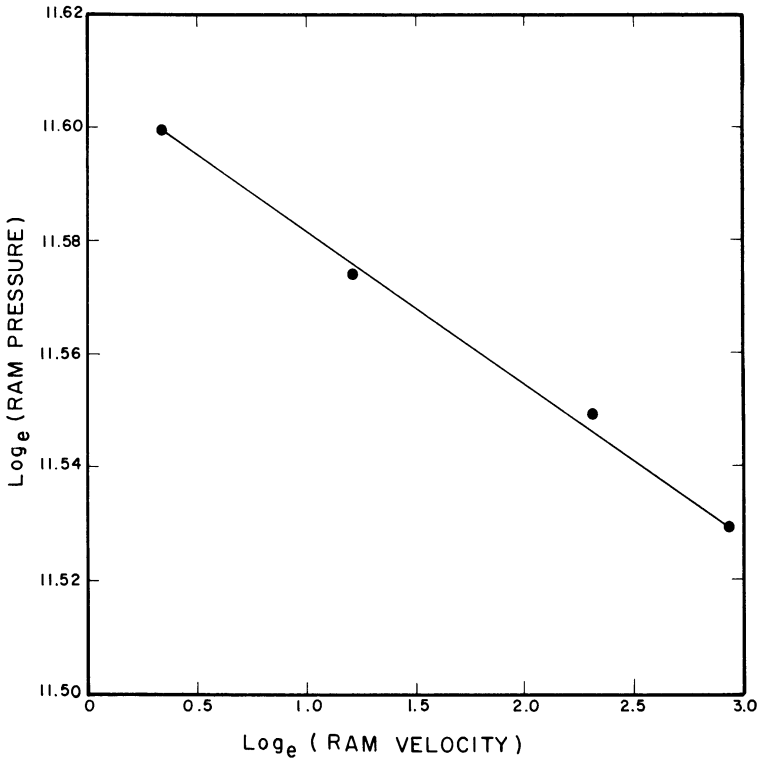

b) Log_e (ram pressure) vs. log_e (ram velocity)

Figure 44. Ram Pressure versus Ram Velocity.

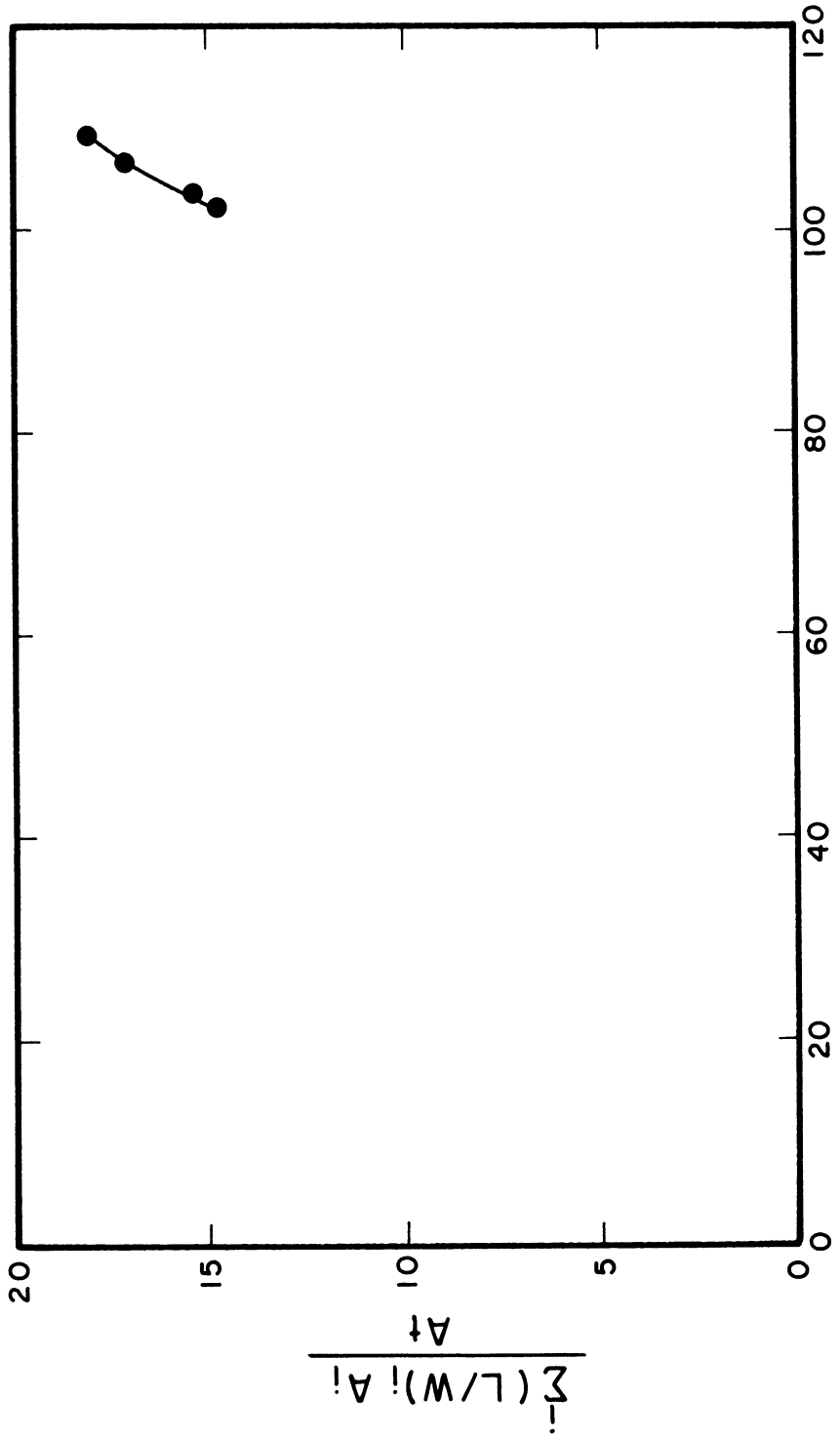

Figure 45. Inclusion Deformation - Ram Pressure Relationship for Strain Rate Study Samples.

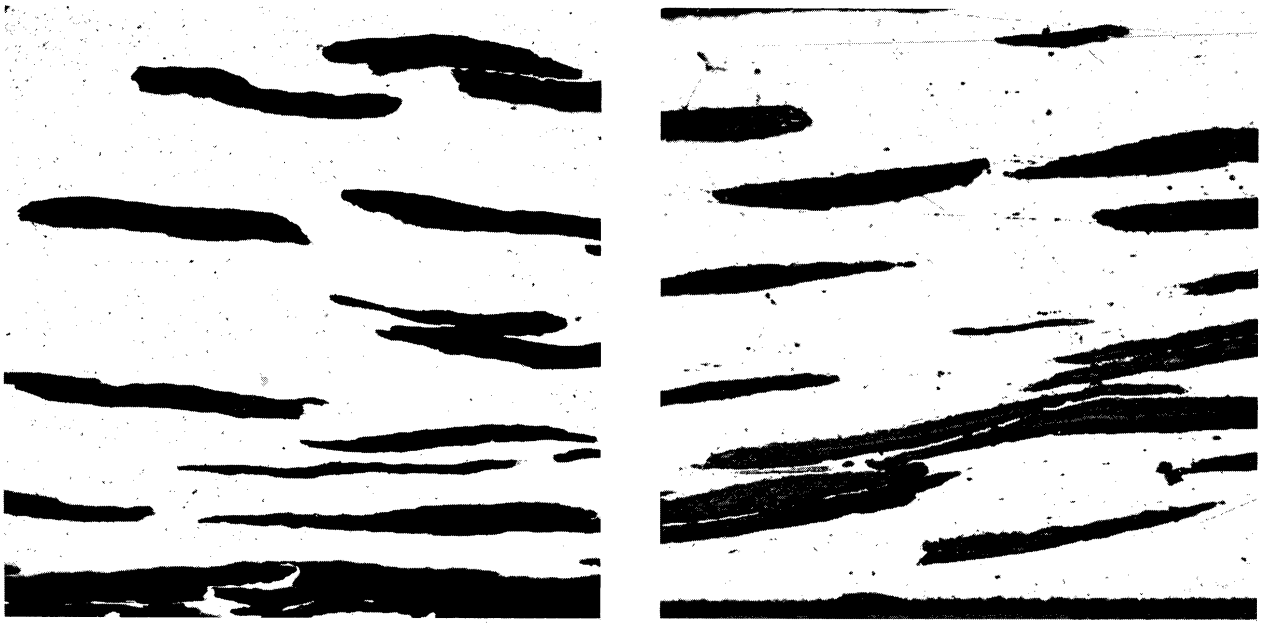

a) Ram velocity: 0.05 ipm.

b) Ram velocity: 0.10 ipm.

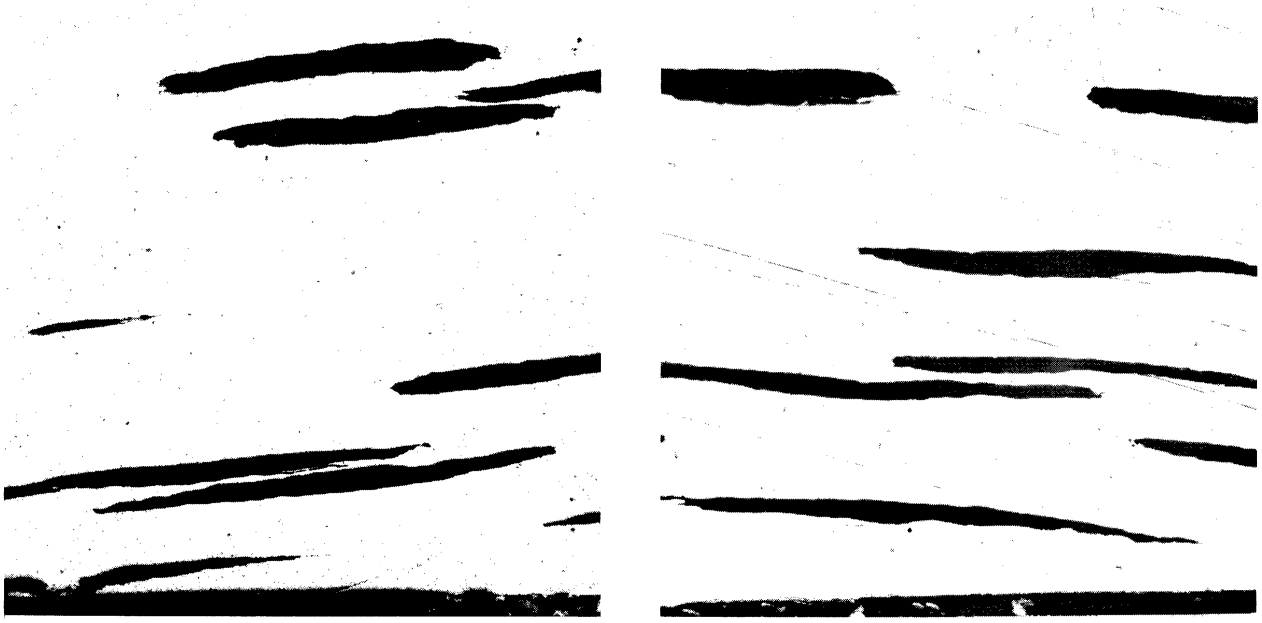

c) Ram velocity: 0.30 ipm.

d) Ram velocity: 0.71 ipm.

Figure 46. Microstructures Illustrating the Effect of Strain Rate on Inclusion Deformation. Samples: 90 Cu - 10 NaCl. Die: 90° -75% reduction. 37.5X.

4. Effect of Temperature

(Data and figures: 90° - 75 per cent reduction dies, copper, NaCl, and 90 Cu - 10 NaCl samples, Figures 47 through 53.)

As an indication of the relative property changes of the individual phases, ram pressure and hardness curves are presented for copper and NaCl samples. Hardness values presented in Figures 50 and 51 were measured at room temperature after the samples were extruded at the indicated temperatures. The inclusion hardness values shown in Figure 51 were measured near the sample centerline. The hardness values described in Figure 52 were measured at temperature on fully annealed materials. The copper and NaCl used for the hot hardness measurements were from a different source than the extrusion materials.

The following temperature effects were observed:

1. The shape of the L/W profile changes above 200°F. Above this temperature, the L/W curves do not tend to level off as the sample surface is approached (Figure 47).
2. A minimum in the amount of inclusion deformation occurs at approximately 300°F (Figures 47 and 48). More inclusions are fractured in the region of this minimum (200 to 500°F) than at higher or lower temperatures. Above 300°F, inclusion deformation increases with increasing temperature.
3. The minimum in the inclusion deformation curve corresponds to a maximum in the inclusion hardness curve (Figures 48 and 51).

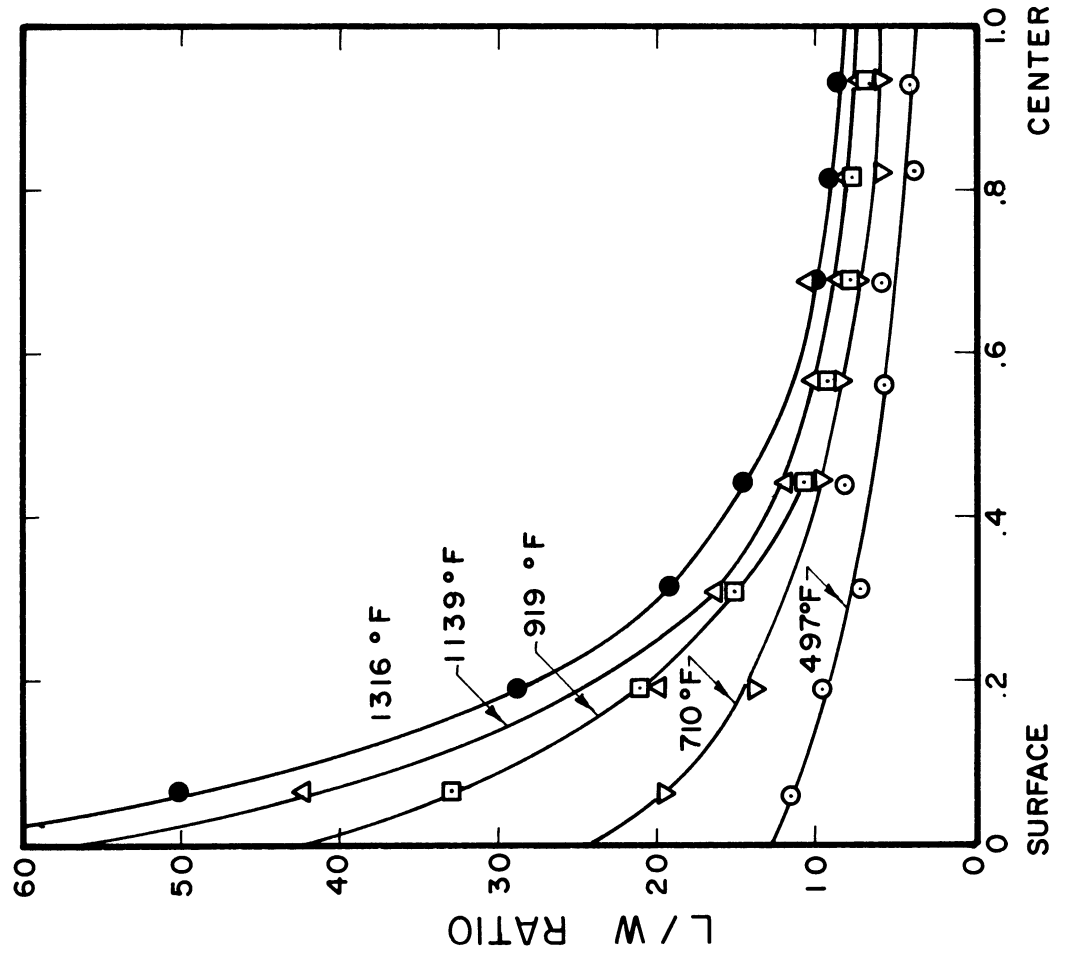

b) Traverses for temperature above 400°F

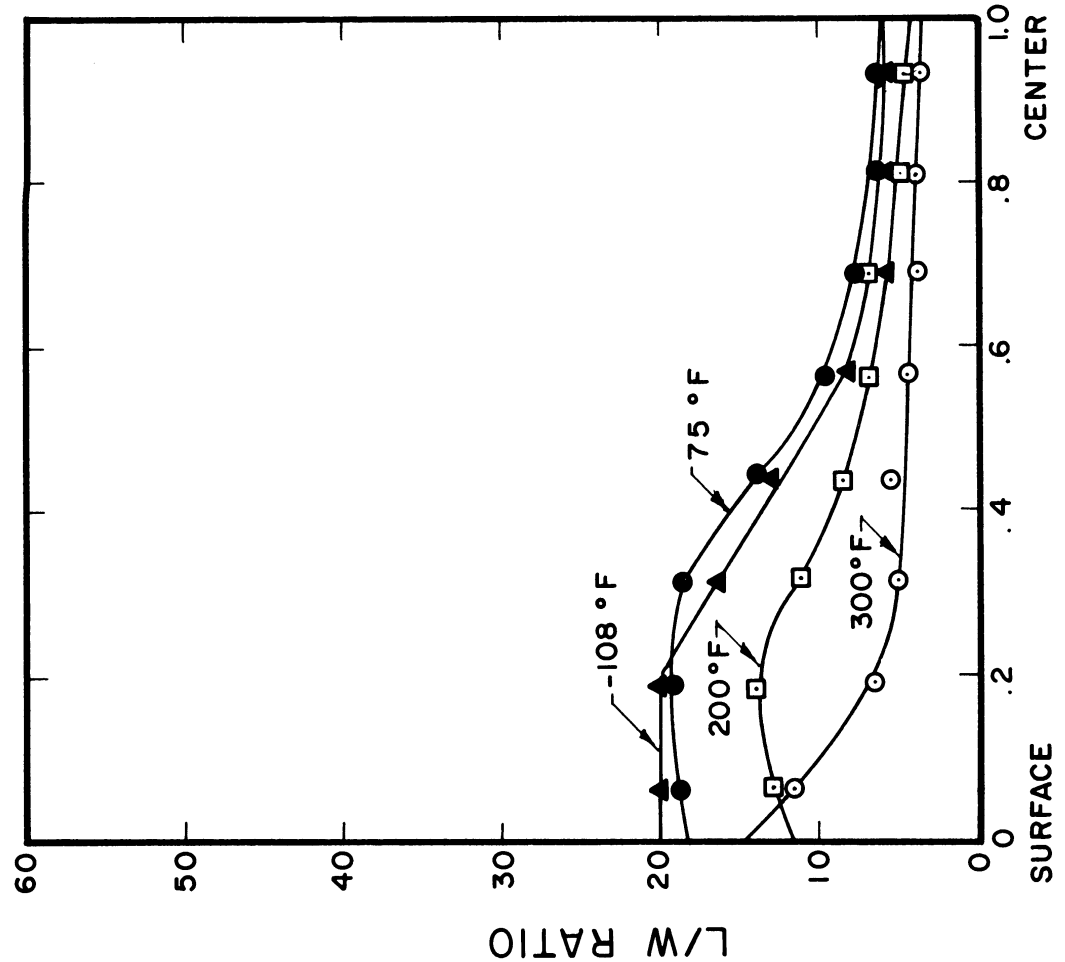

a) Traverses for temperatures below 400°F

Figure 47. L/W Traverses for Temperature Study Samples.

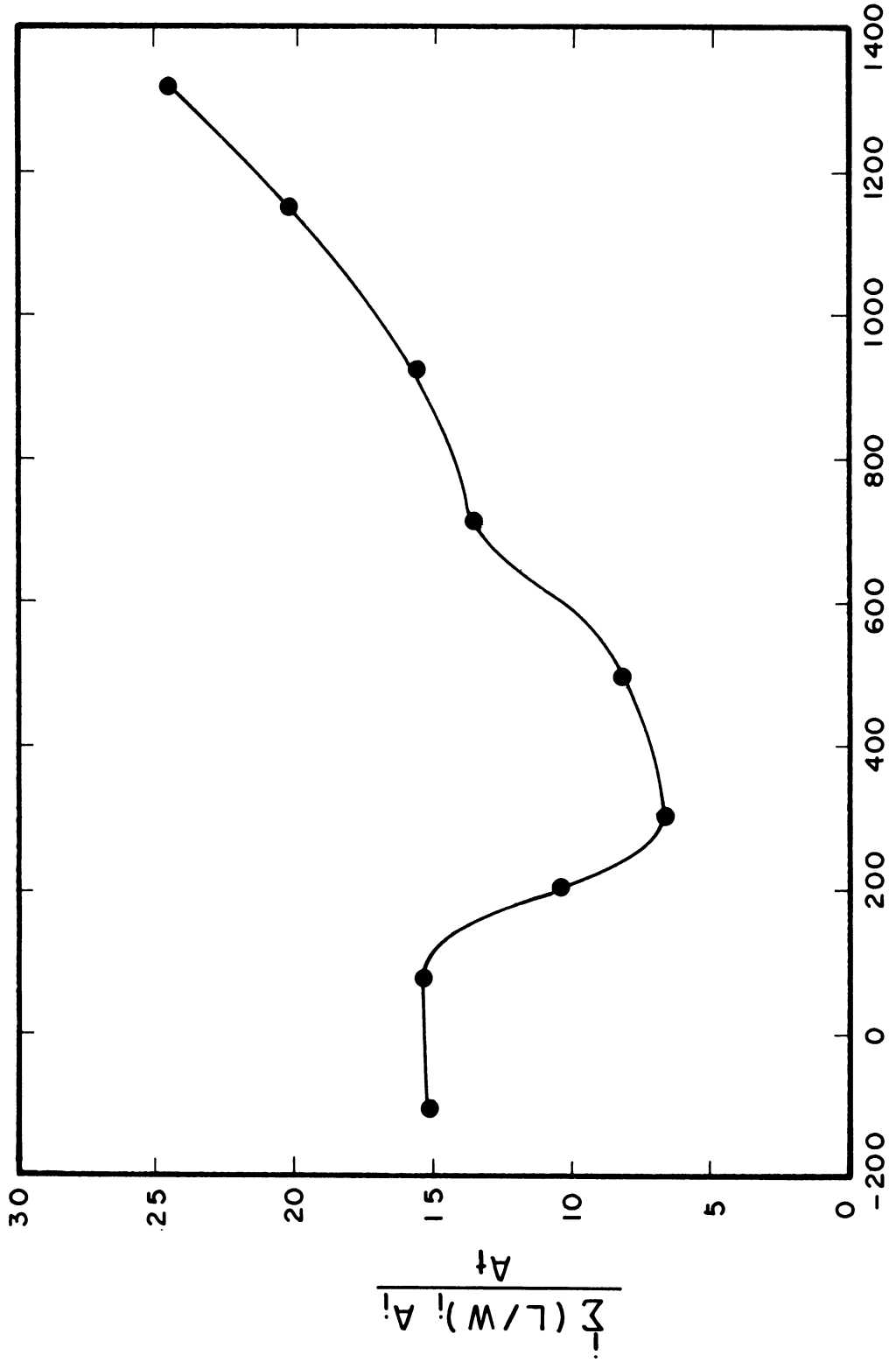

Figure 48. Inclusion Deformation versus Temperature.

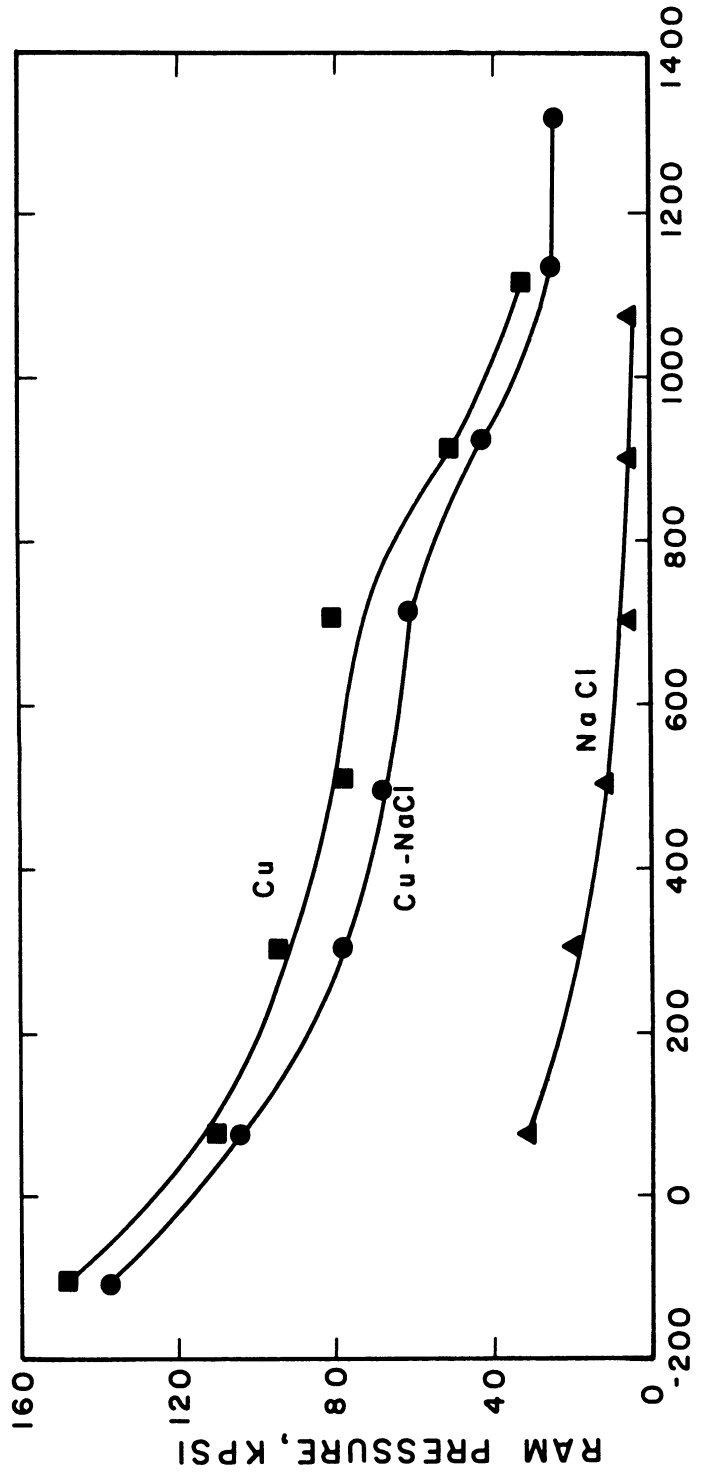

Figure 49. Ram Pressure versus Temperature.
The NaCl curves is after Moore.(121)

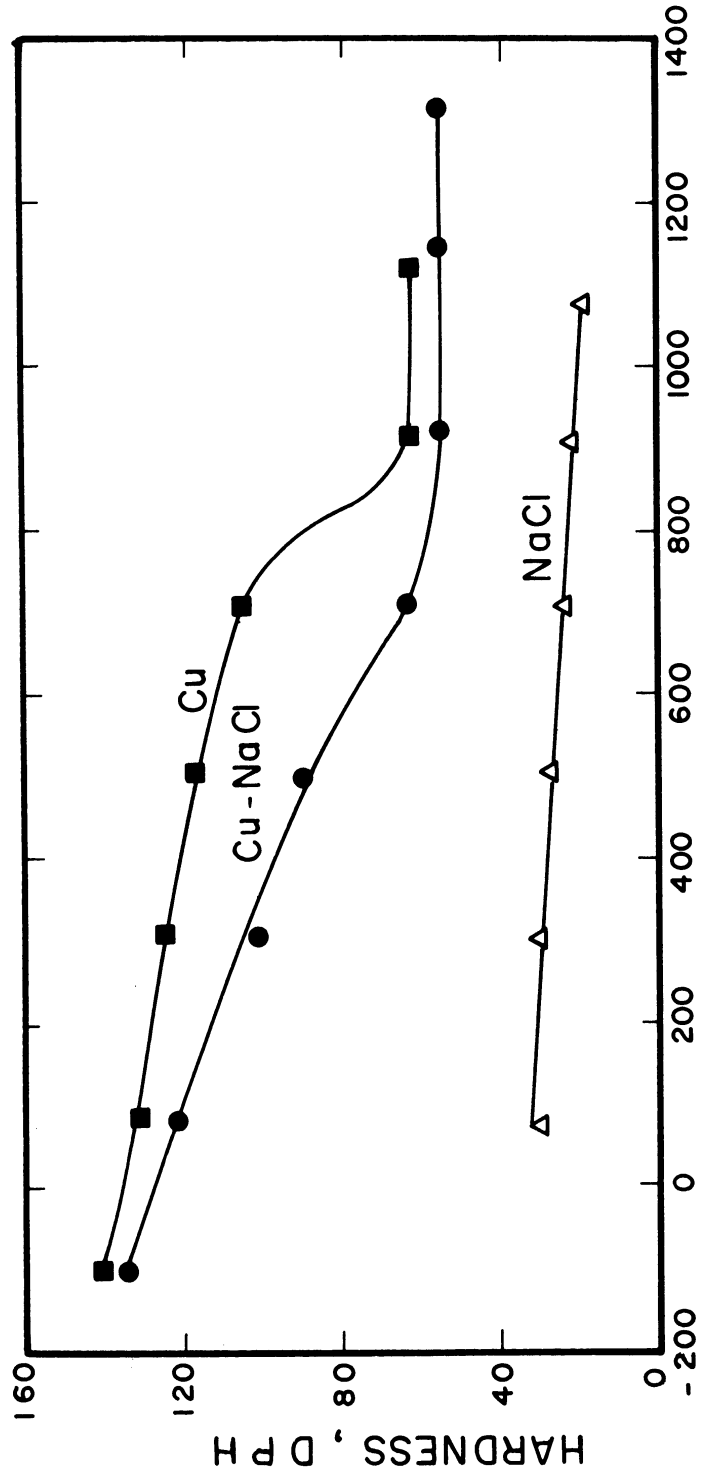

Figure 50. Matrix Hardness versus Temperature. The NaCl curve is after Moore.(121) The hardness values were measured at room temperature after extrusion at the indicated temperatures.

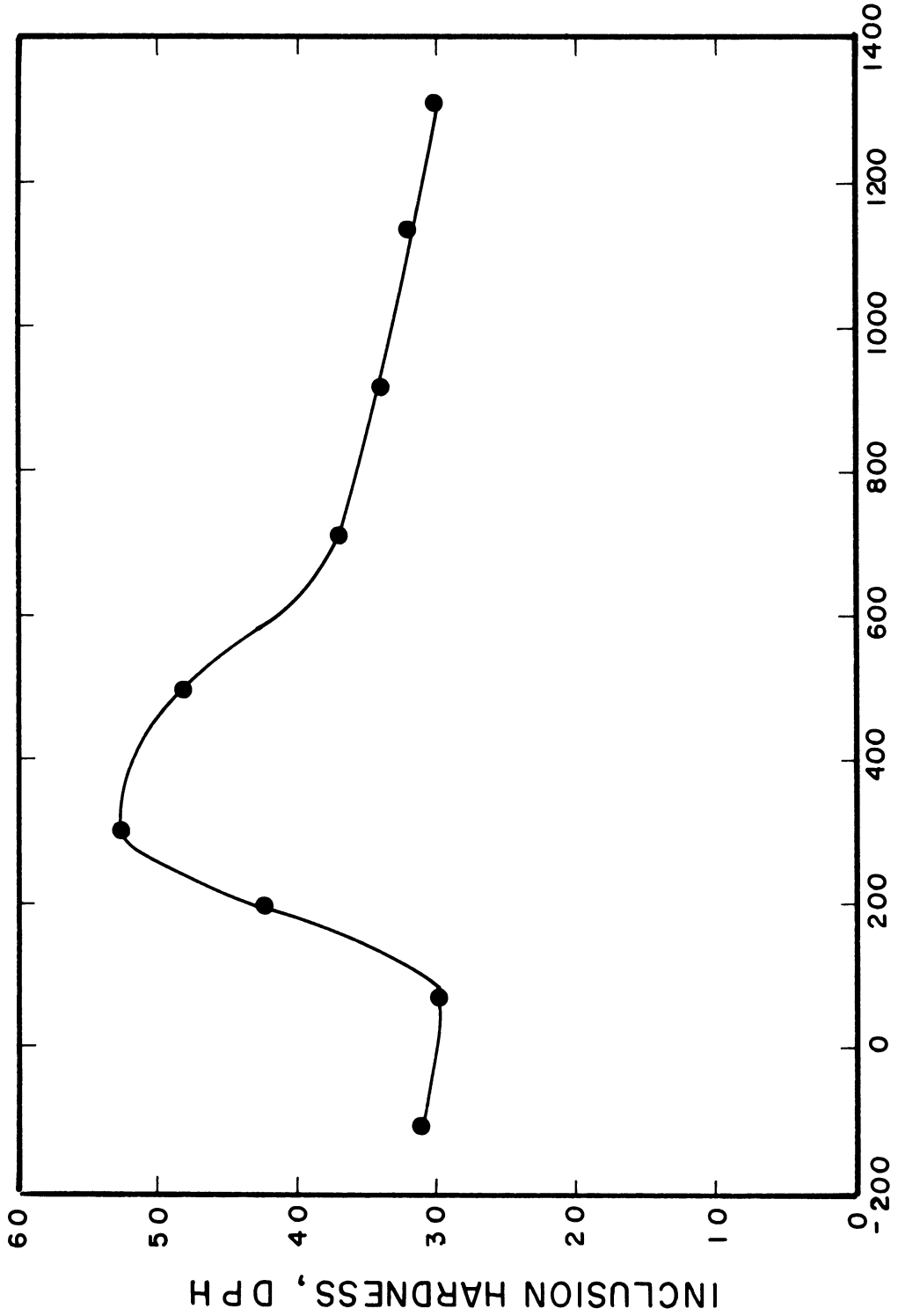

Figure 51. Inclusion Hardness versus Temperature. The hardness values were measured at room temperature after extrusion at the indicated temperatures.

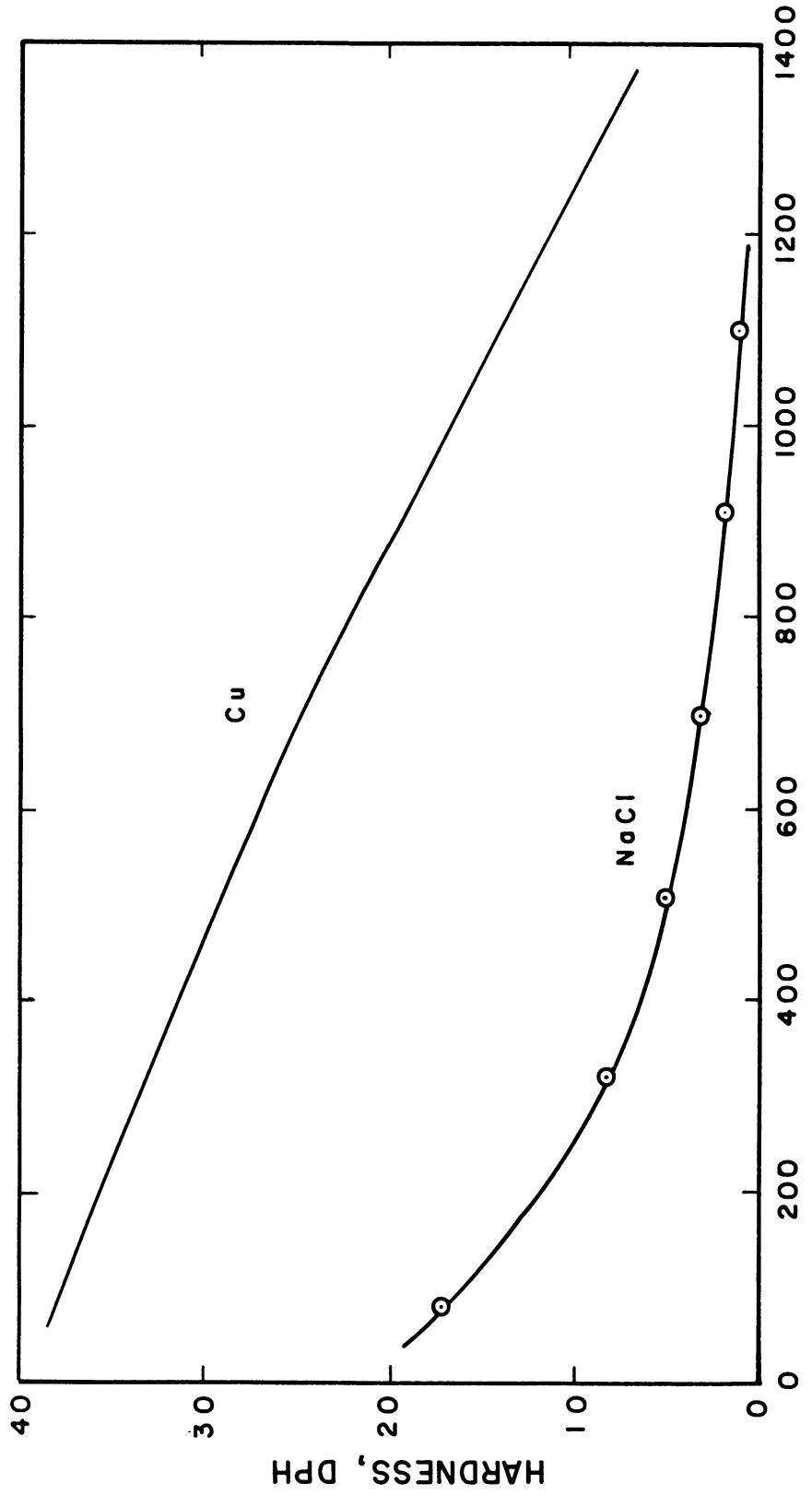

Figure 52. Hot Hardness of Annealed Copper and NaCl. The copper curve is after Chao.(122)

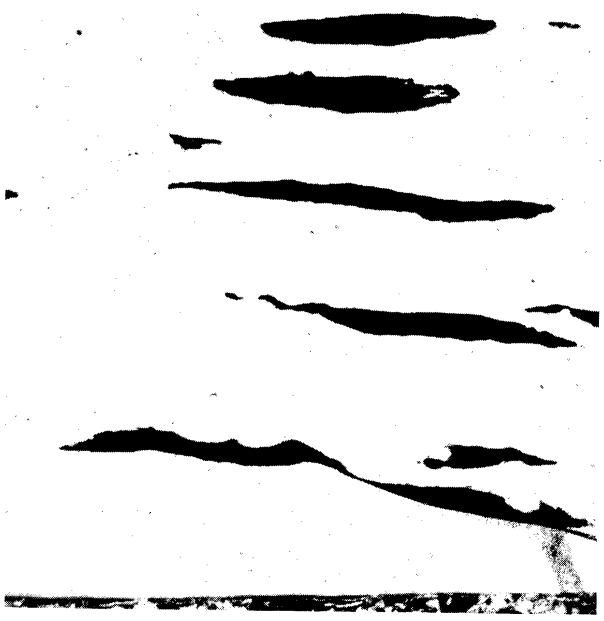

a) Temperature: -108°F.

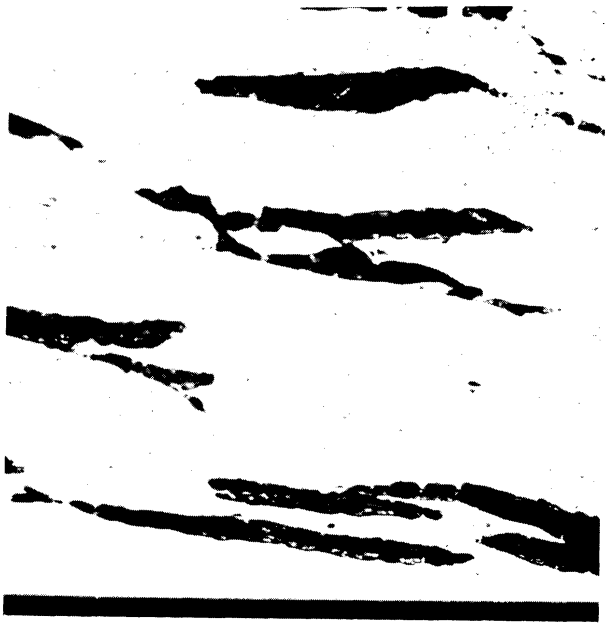

b) Temperature: 300°F.

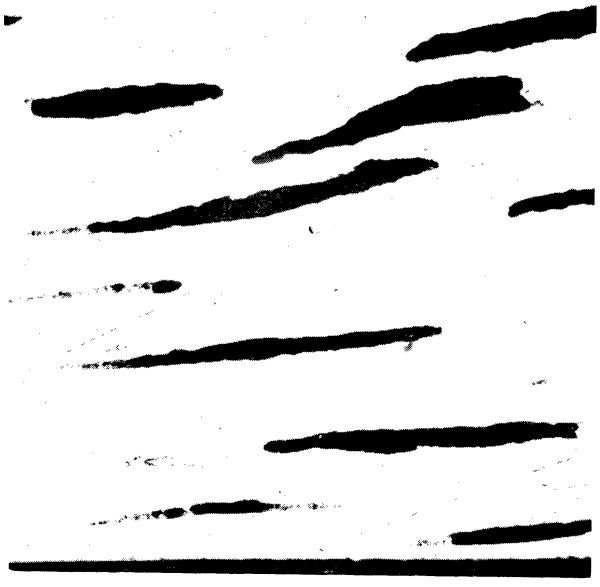

c) Temperature: 710°F.

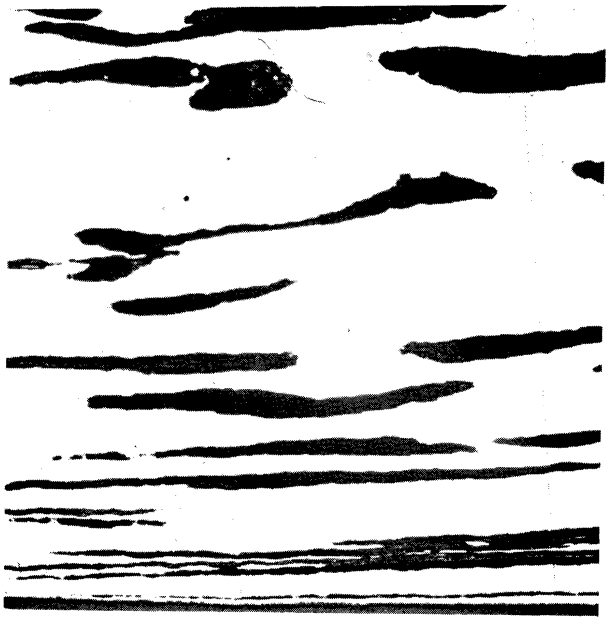

d) Temperature: 1316°F.

Figure 53. Microstructures Illustrating the Effect of Temperature on Inclusion Deformation. Samples: 90 Cu - 10 NaCl. Die: 90° - 75% reduction. 37.5X.

4. Ram pressure decreases with increasing temperature for copper, 90 Cu - 10 NaCl, and NaCl samples (Figure 49).
5. The cold to hot working region change occurs between 700 and 1100°F for pure copper (Figures 49 and 50).
6. The copper in the 90 Cu - 10 NaCl sample strain hardens less than in the pure copper sample during extrusion (Figure 50).
7. For annealed Harshaw NaCl single crystals and high purity copper, hardness decreases smoothly with increasing temperature (Figure 52).

5. Effect of Per Cent Nonmetallic Material

(Data and figures: 90° - 75 per cent reduction dies, copper-NaCl samples, Figures 54 through 58)

As the volume per cent NaCl increases, the following effects were observed:

1. The amount of inclusion deformation decreases (Figures 54 and 55).
2. Ram pressure decreases linearly (Figure 56).

The NaCl inclusions deform more than the copper matrix for all compositions (Figure 55).

6. Effect of Nonmetallic Inclusion Size

(Data and figures: 90° - 75 per cent reduction dies, 90 Cu - 10 NaCl samples, Figures 59 through 62)

The particle size reported is the arithmetic mean for the screened salt fraction used to make up the samples. A "mean L/W value" vs. ram pressure plot was not presented since the data reduce to a point.

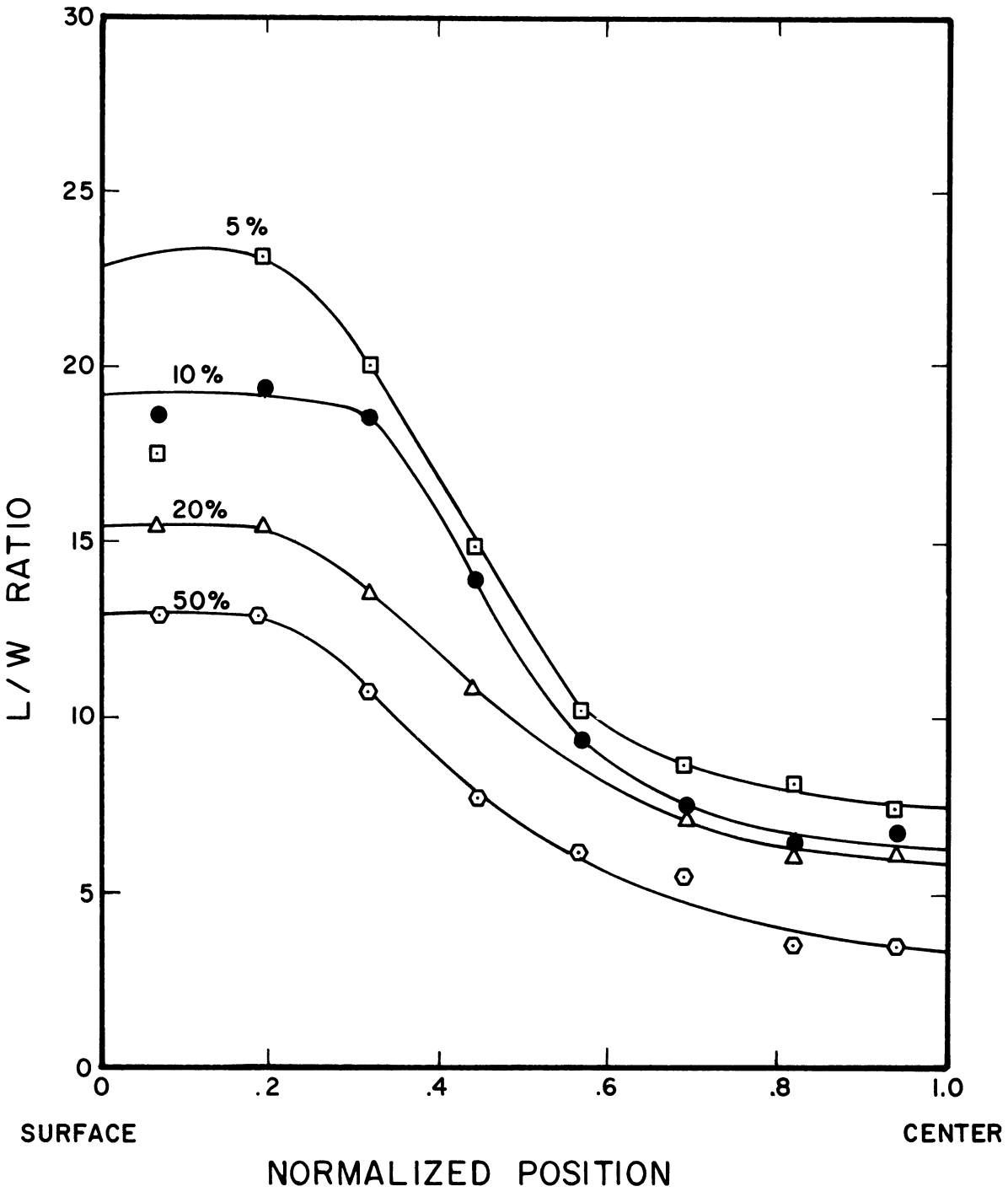

Figure 54. L/W Traverses for Per Cent Nonmetallic Material Study Samples. Per cents of the NaCl phase are indicated.

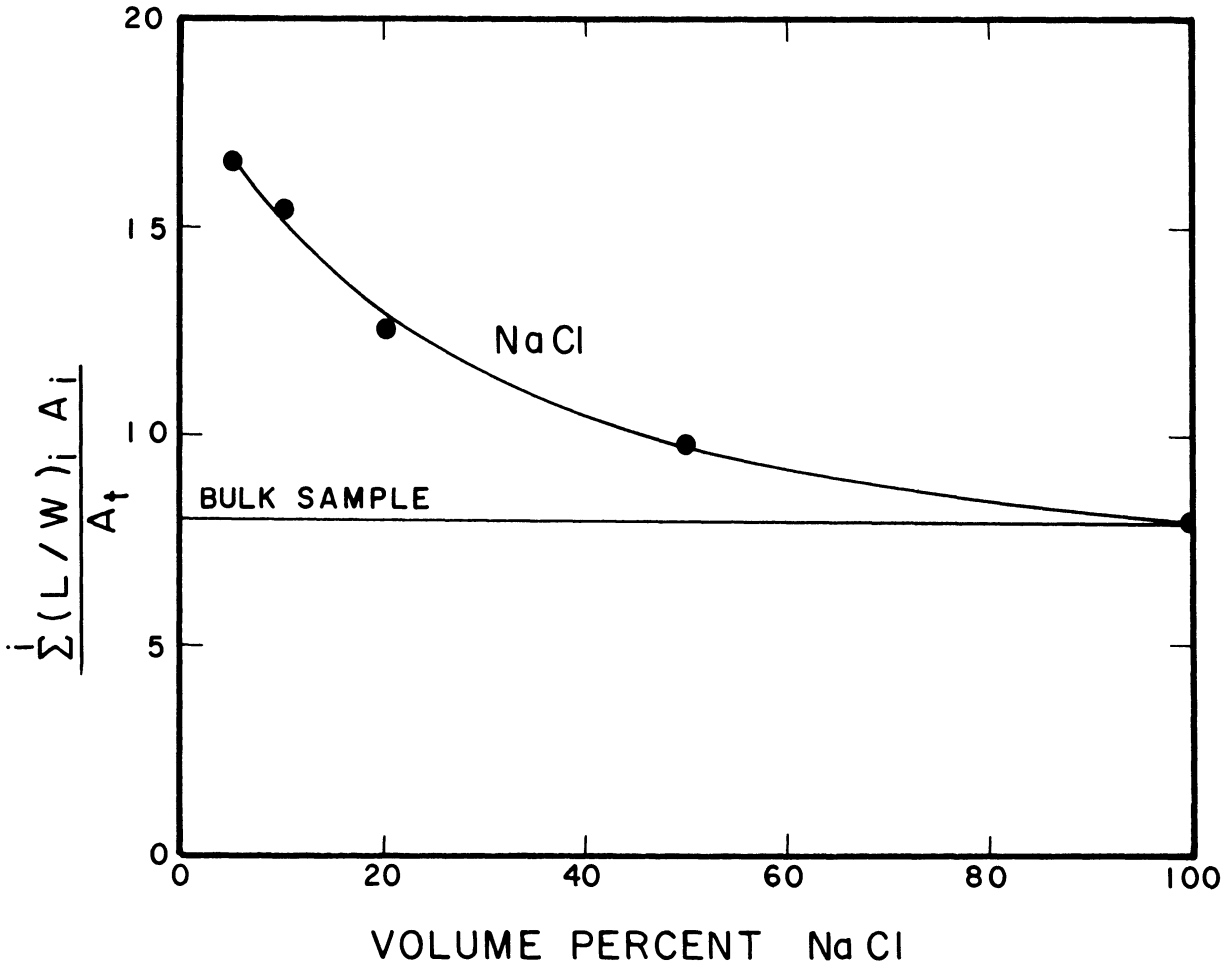

Figure 55. Inclusion Deformation versus Per Cent NaCl.

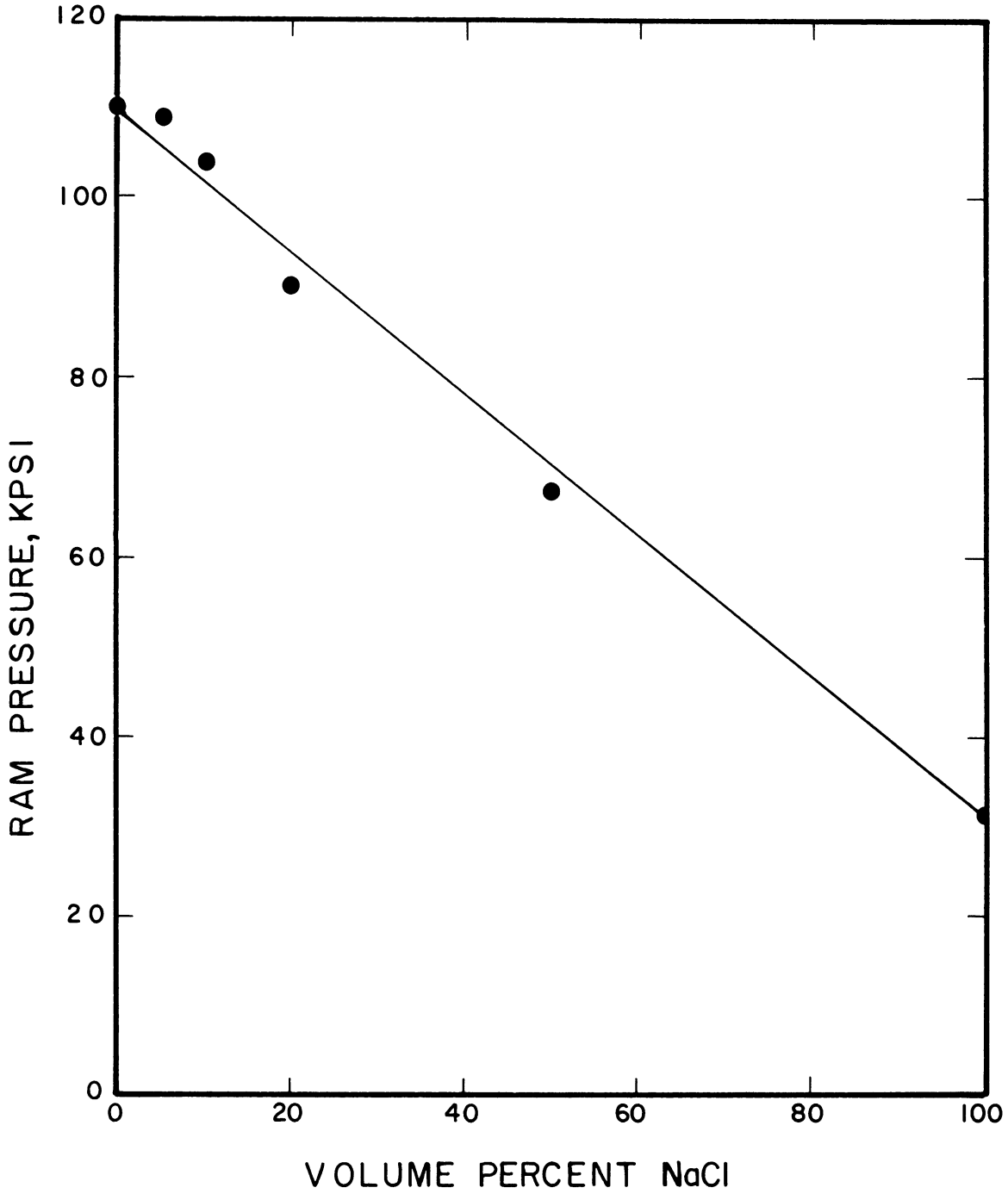

Figure 56. Ram Pressure versus Per Cent NaCl.

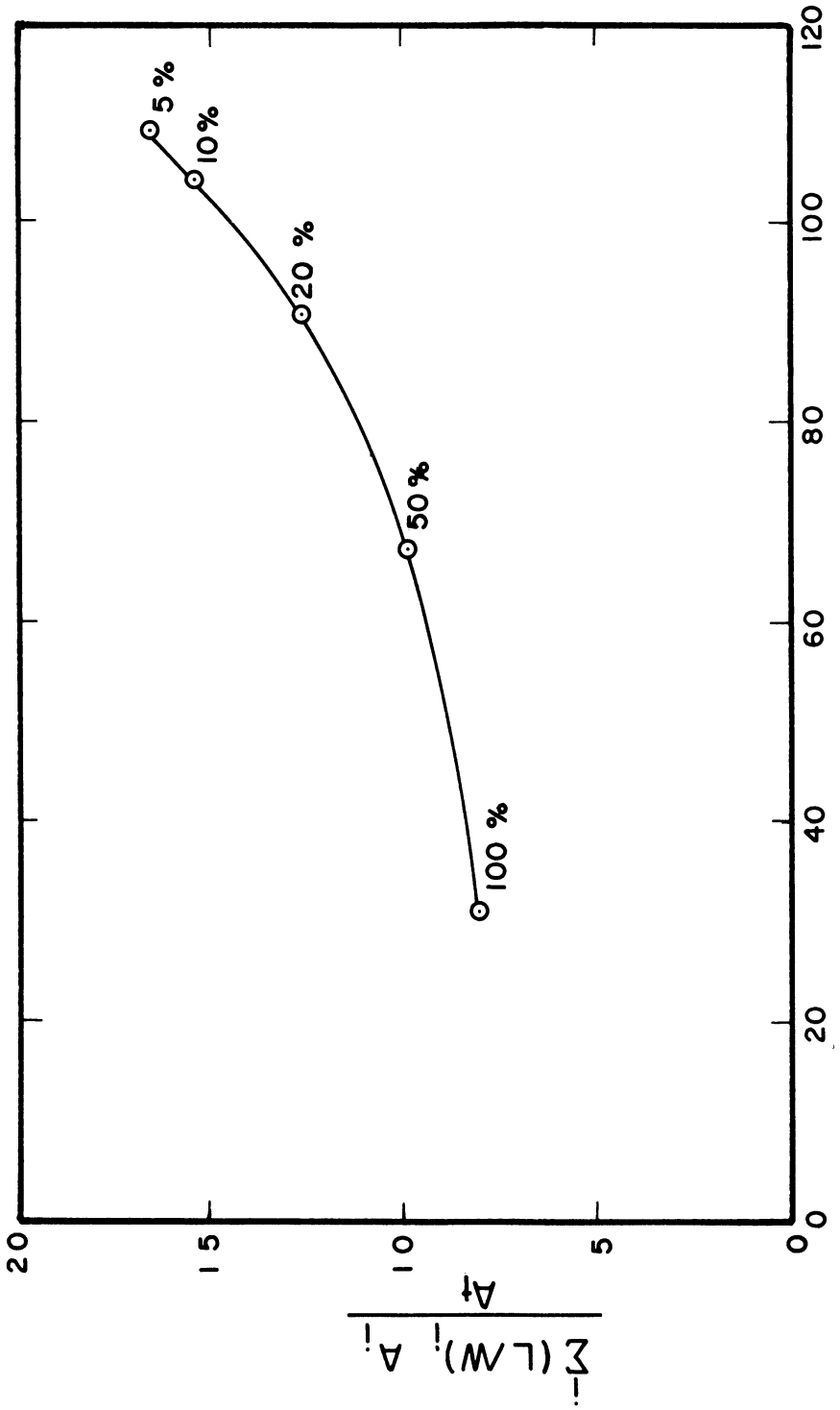

Figure 57. Inclusion Deformation - Ram Pressure Relationship for Per Cent NaCl Study Samples.

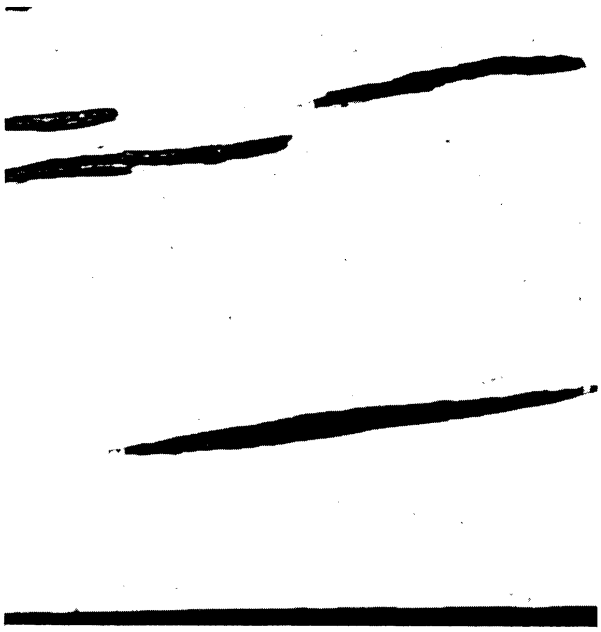

a) Sample: 95 Cu - 5 NaCl.

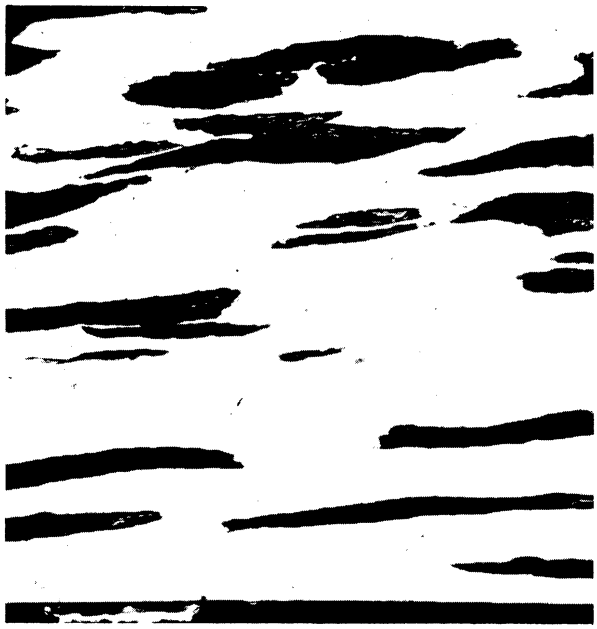

b) Sample: 80 Cu - 10 NaCl.

c) Sample: 50 Cu - 50 NaCl.

d) Sample: 100 NaCl.

Figure 58. Microstructures Illustrating the Effect of Per Cent NaCl on Inclusion Deformation. Die: 90° - 75% reduction. 37.5X.

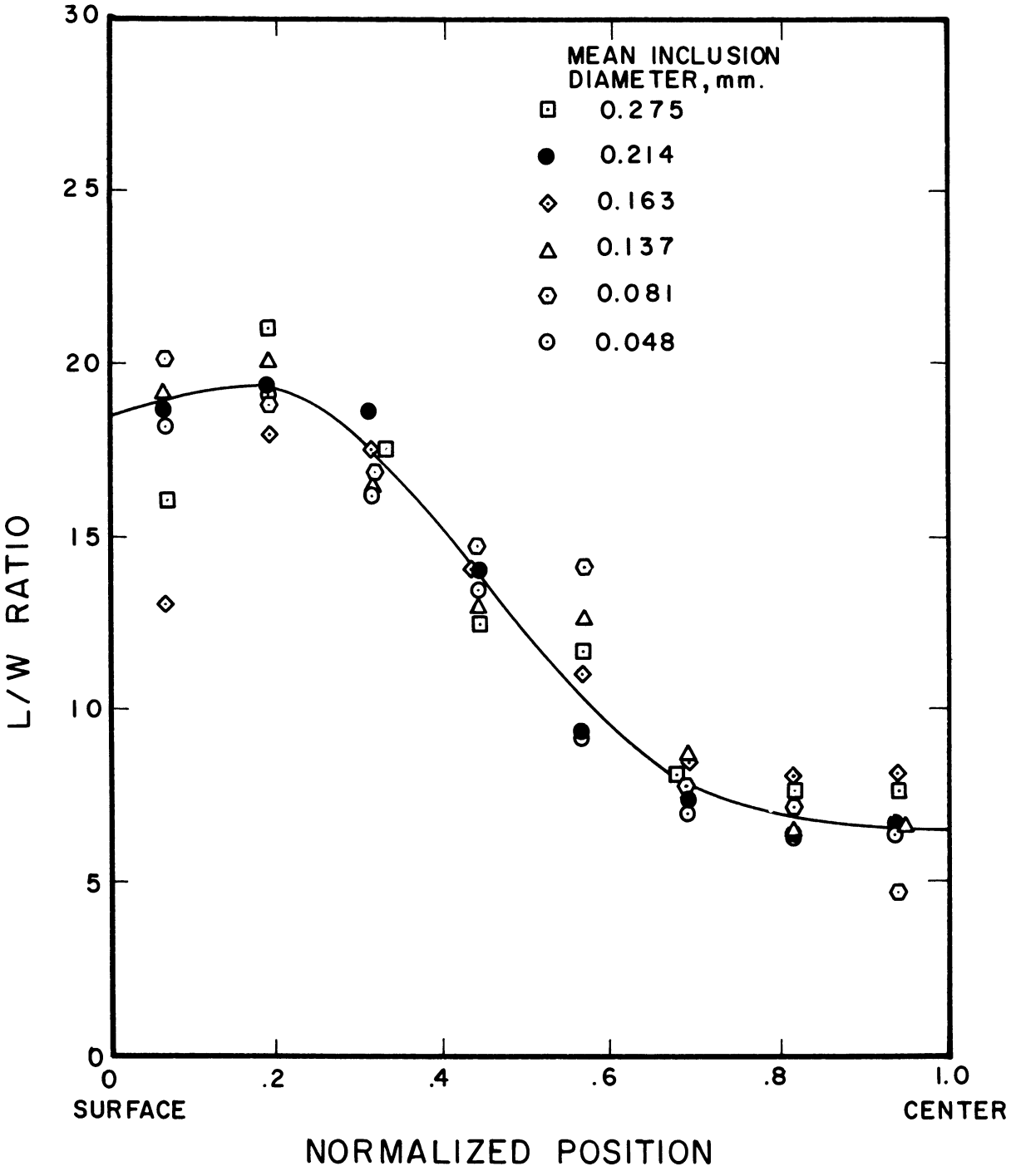

Figure 59. L/W Traverses for Inclusion Size Study Samples.

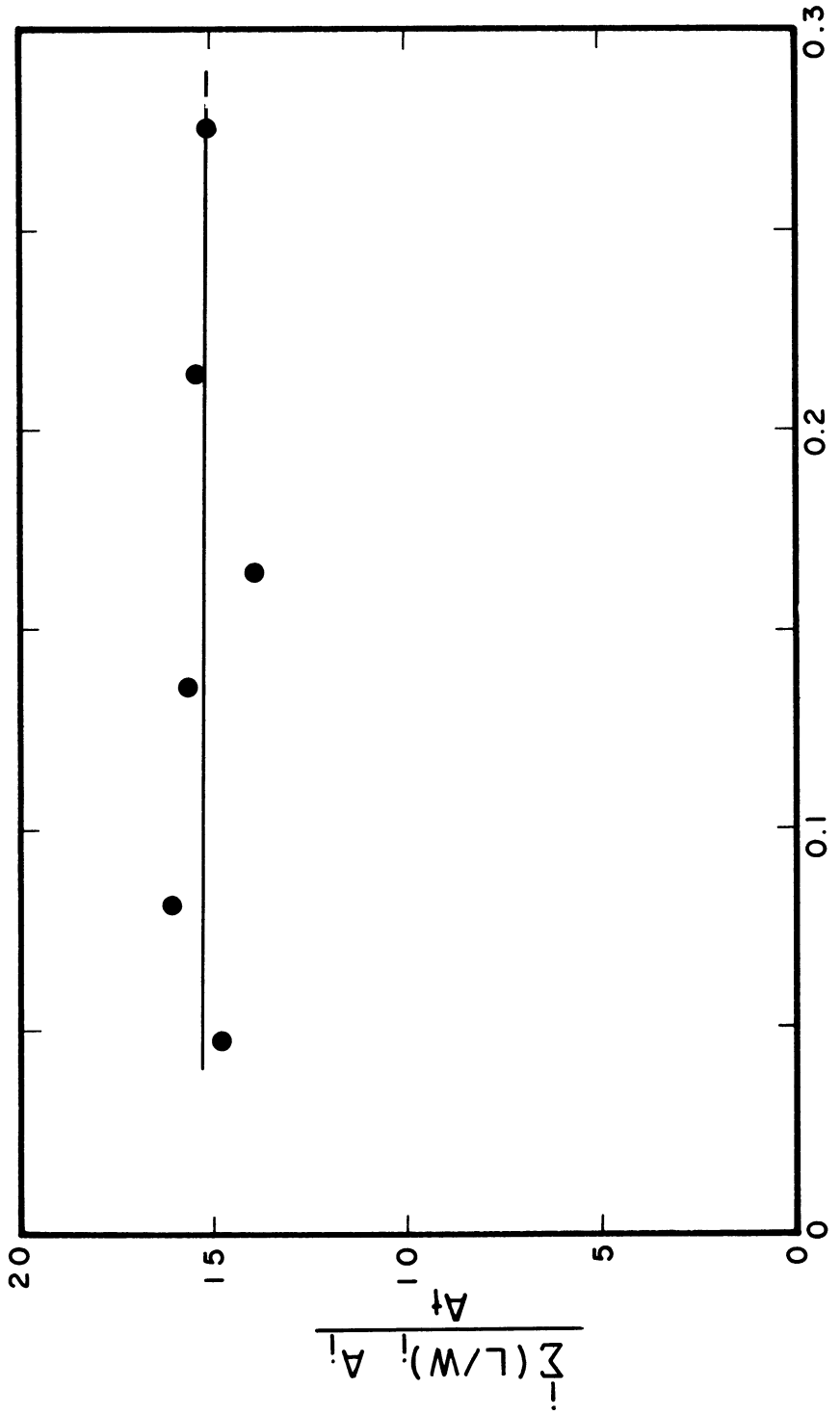

Figure 60. Inclusion Deformation versus Mean Inclusion Diameter.

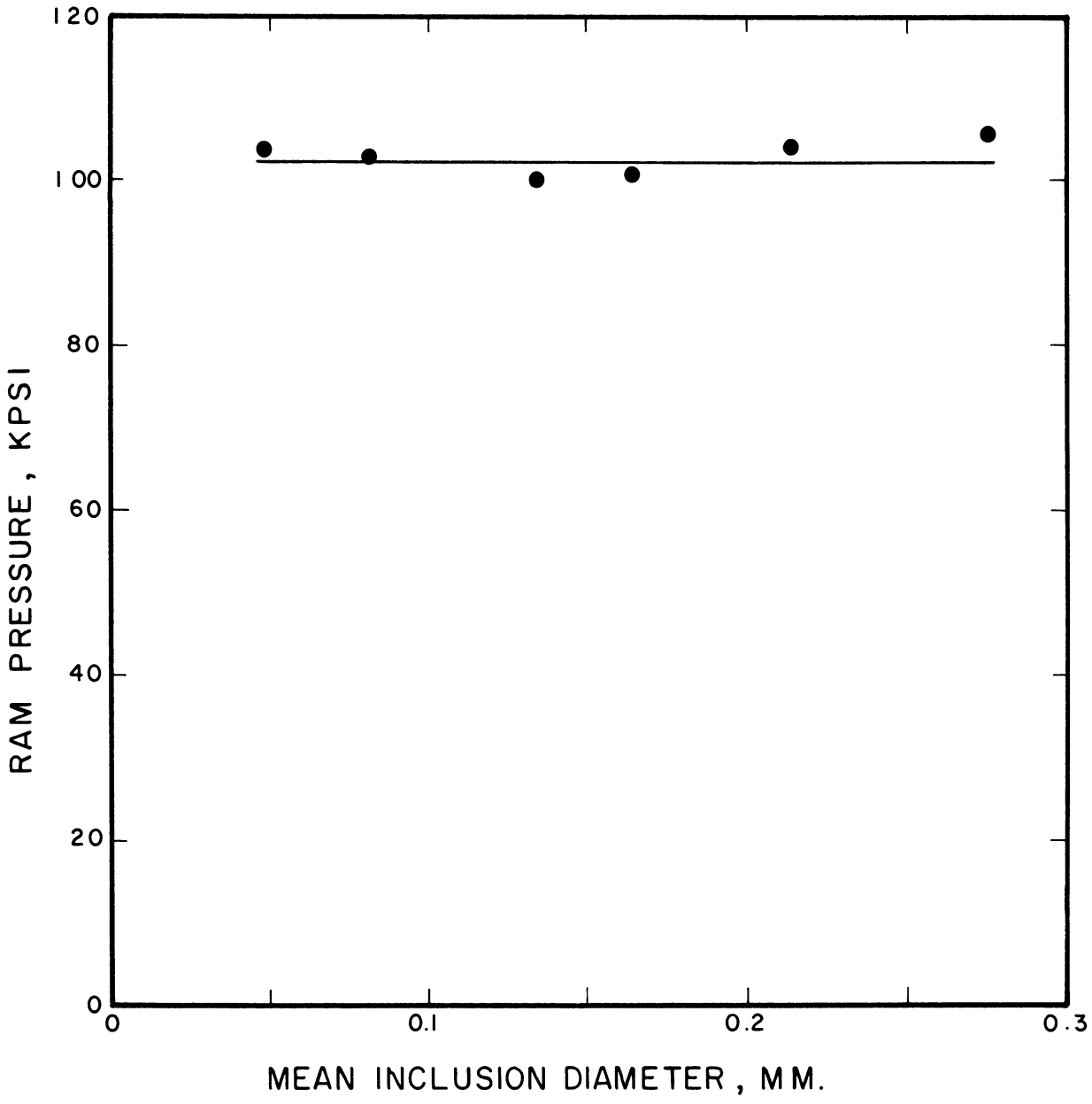

Figure 61. Ram Pressure versus Mean Inclusion Diameter.

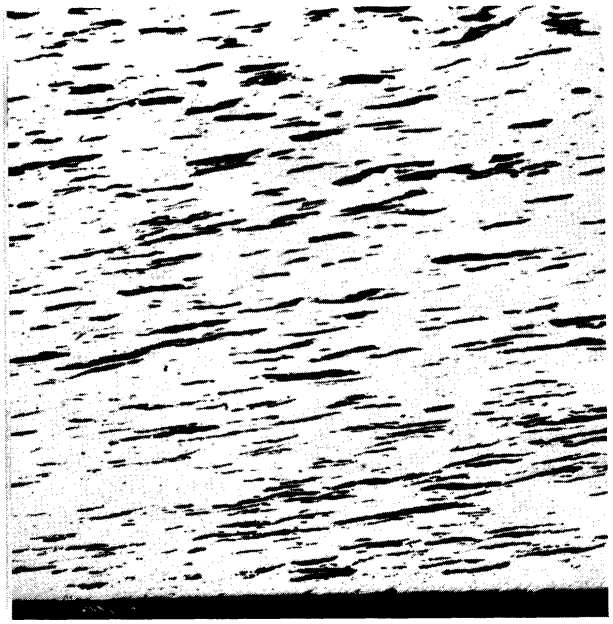

a) Mean inclusion diameter: 0.048 mm.

b) Mean inclusion diameter: 0.081 mm.

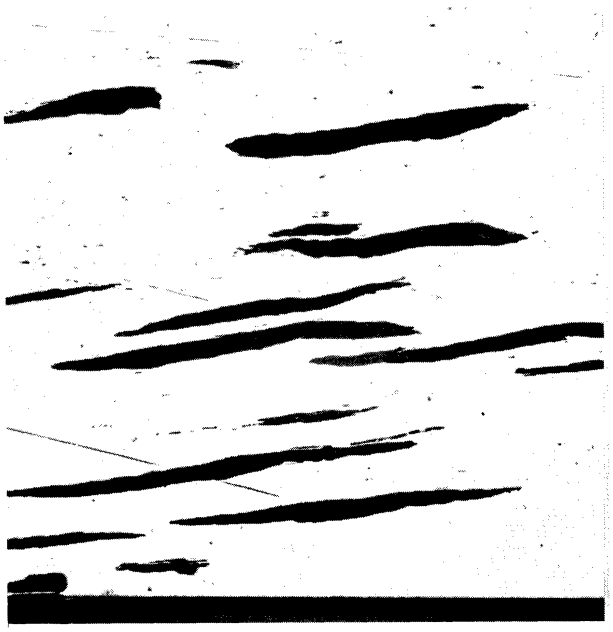

c) Mean inclusion diameter: 0.163 mm.

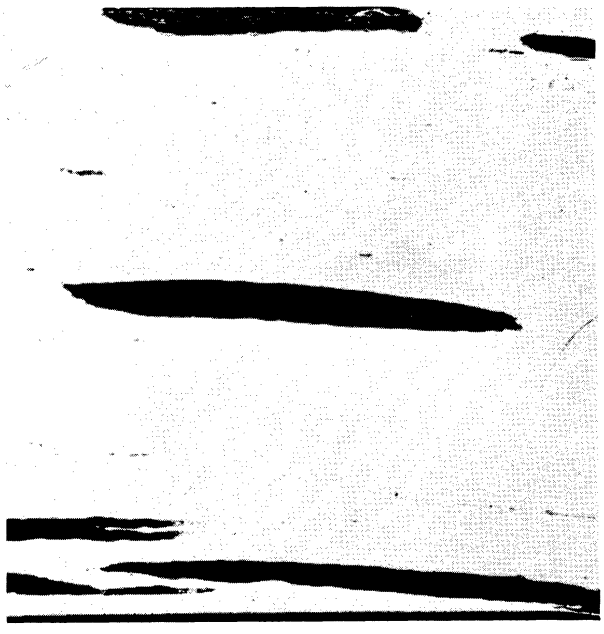

d) Mean inclusion diameter: 0.275 mm.

Figure 62. Microstructures Illustrating the Effect of Inclusion Size on Inclusion Deformation. Samples: 90 Cu - 10 NaCl. Die: 90° -75% reduction. 37.5X.

The following effects were observed:

1. The L/W profiles across all of the samples are approximately the same (Figure 59).
2. The amount of inclusion deformation decreases very slightly with increasing inclusion size (Figure 60).
3. The ram pressure does not change with inclusion size (Figure 61). A least squares fit of a straight line to the experimental data indicates a slope of 1000 psi/mm which is not a significant variation.

7. Effect of Inclusion Type

(Data and figures: 90° - 75 per cent reduction dies, 90 per cent copper - balance KCl, NaCl, NaF, or LiF samples, Figures 63 through 67)

Inclusion hardness was used as the index of the inclusion properties. Both average and final inclusion hardness values are plotted. The average hardness values plotted are the average of the inclusion hardness values before and after extrusion while the final hardness is the inclusion hardness in the extruded samples. The inclusion L/W ratio in the as-sintered samples varies with inclusion type. To eliminate this variable, the L/W ratio at the sample center was corrected for the as-sintered L/W ratio and plotted in Figure 64(a). However, the L/W correction does not change the results appreciably.

As inclusion hardness increases, the following effects can be observed:

1. The amount of inclusion deformation decreases (Figures 63 and 64).
2. The ram pressure increases (Figure 65).

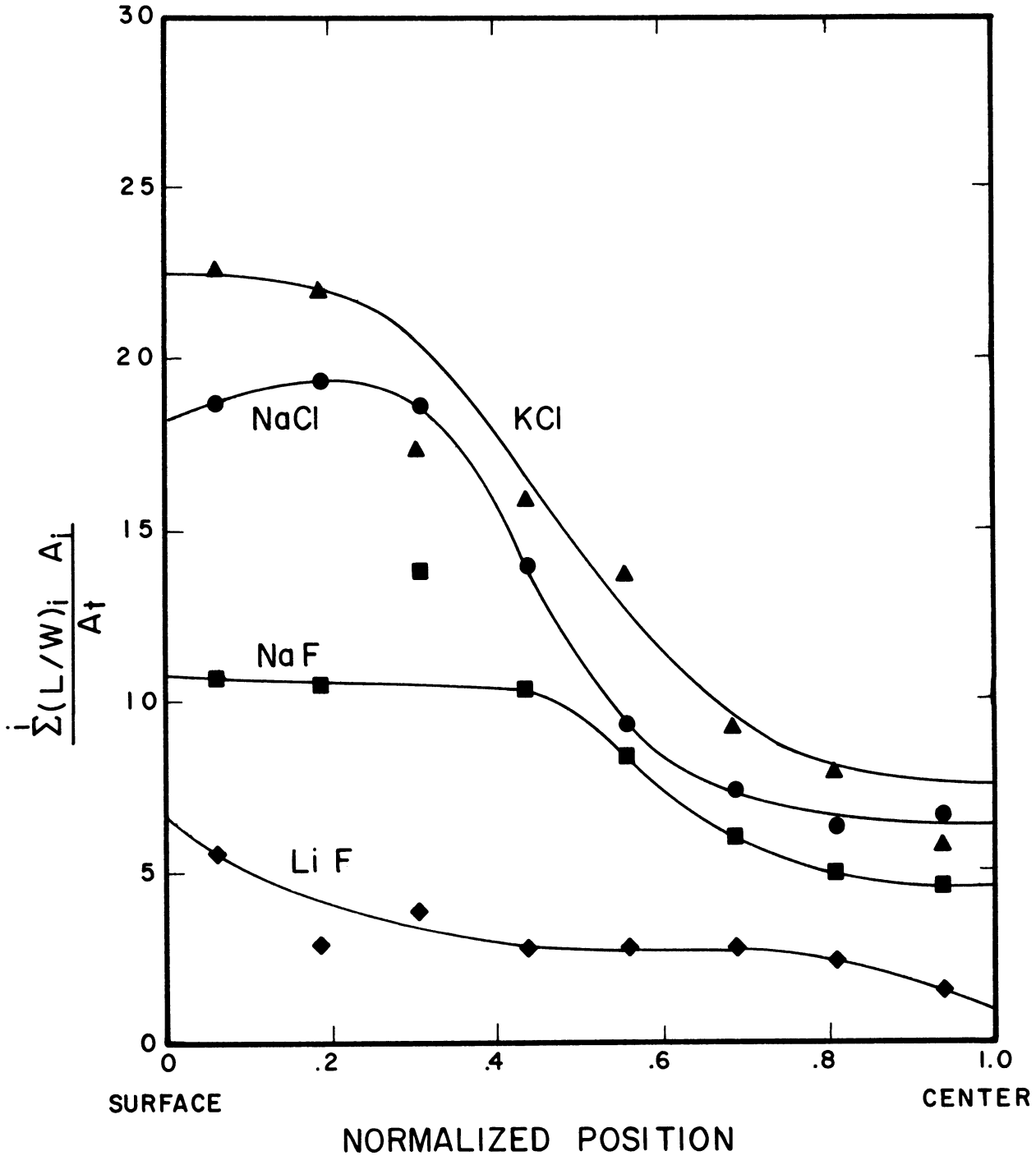

Figure 63. L/W Traverses for Inclusion Type Study Samples.

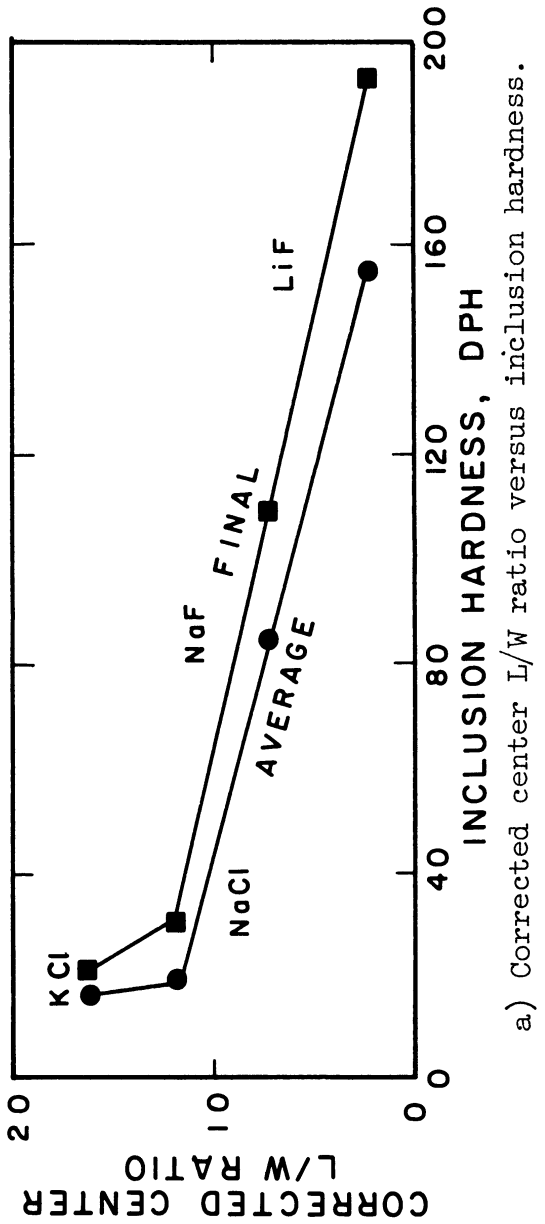

a) Corrected center L/W ratio versus inclusion hardness.

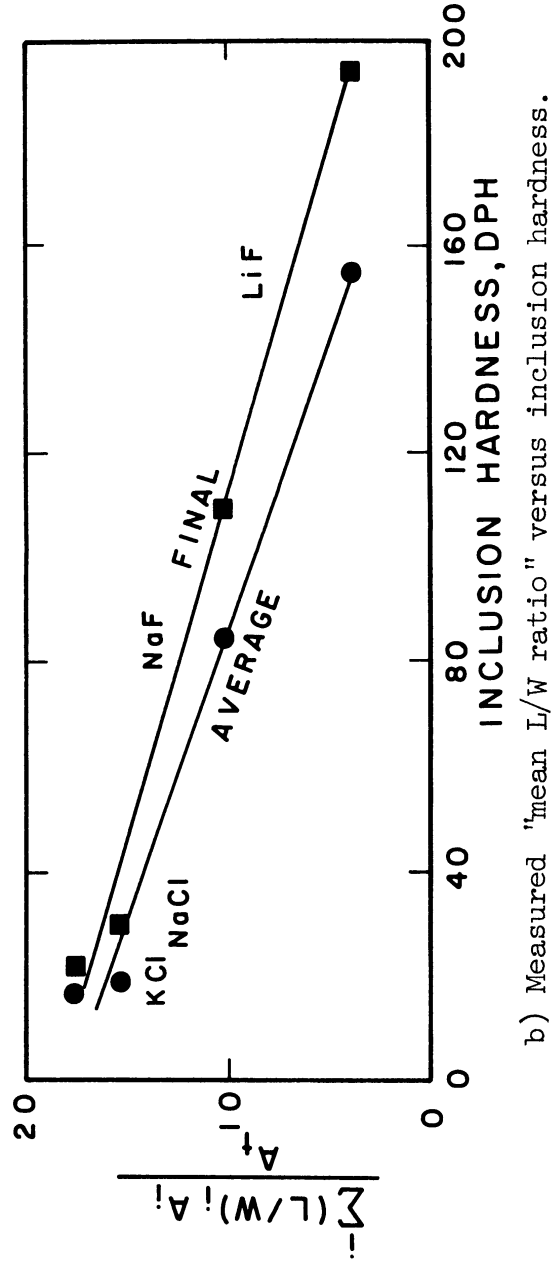

b) Measured "mean L/W ratio" versus inclusion hardness.

Figure 64. Inclusion Deformation versus Inclusion Hardness.

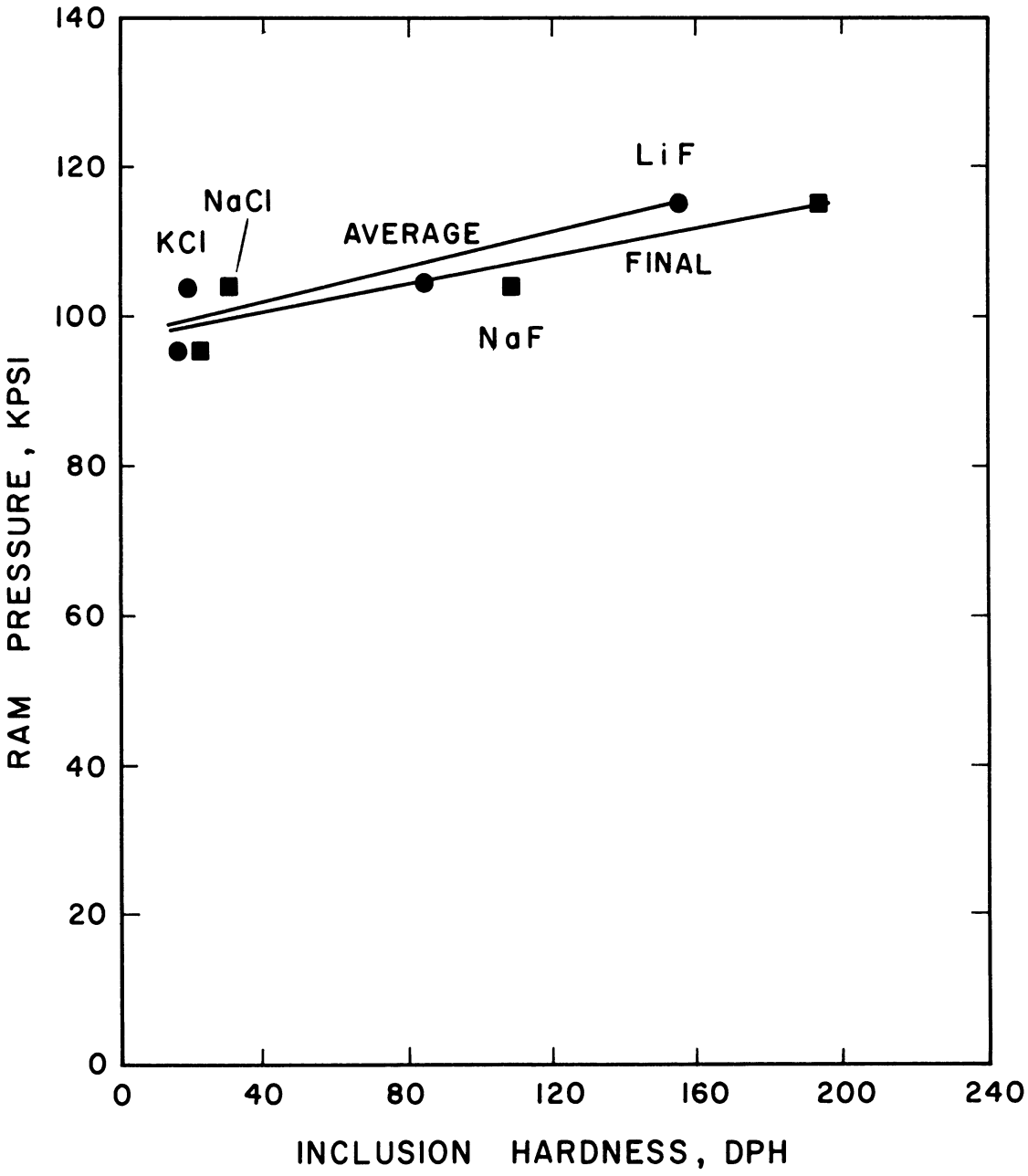

Figure 65. Ram Pressure versus Inclusion Hardness.

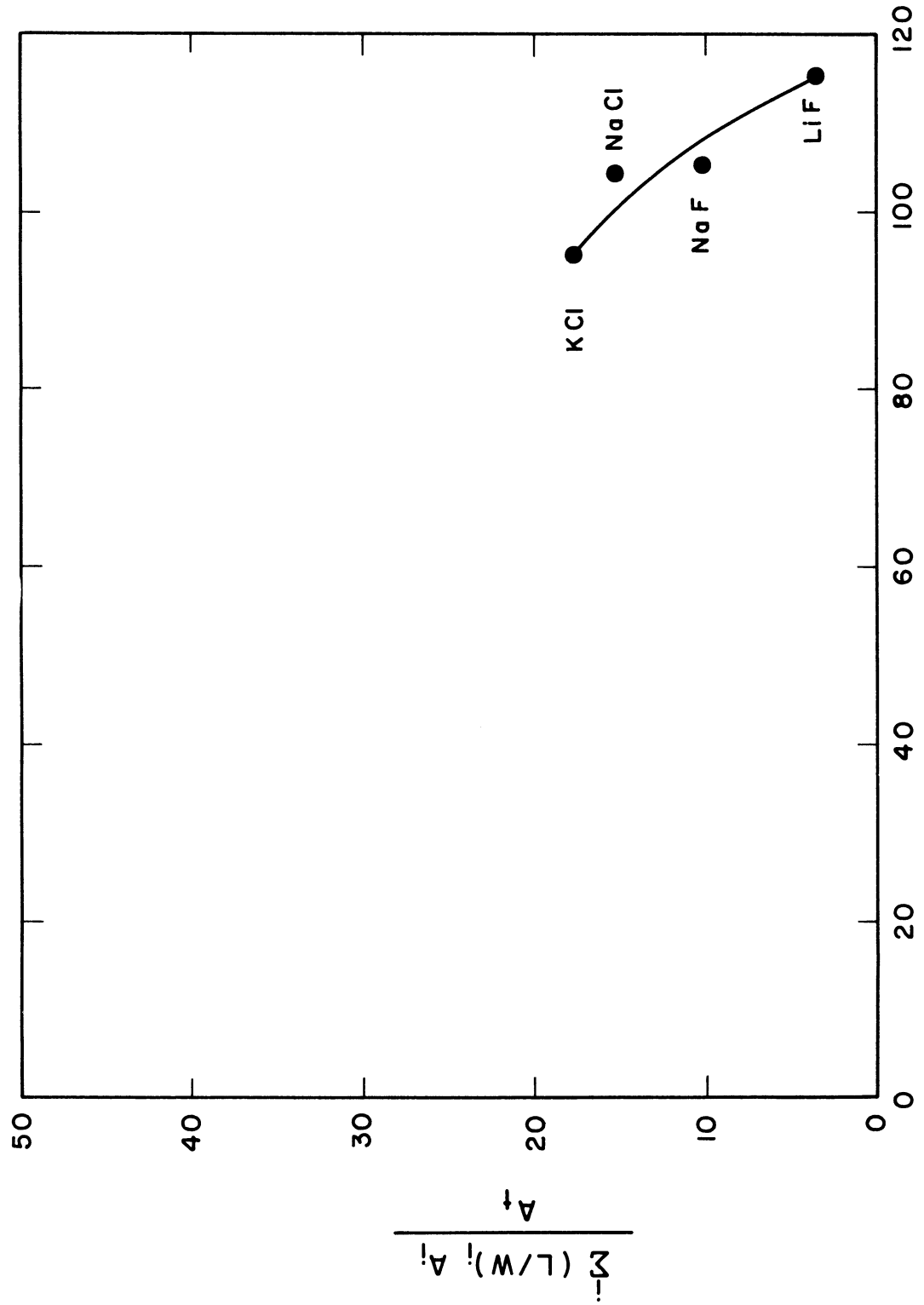

Figure 66. Inclusion Deformation - Ram Pressure Relationship for Inclusion Type Study Samples.

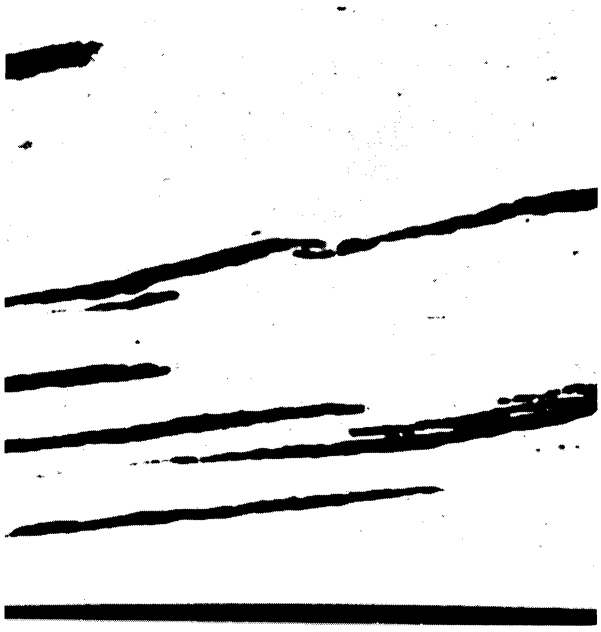

a) Sample: 90 Cu - 10 KCl.

b) Sample: 90 Cu - 10 NaCl.

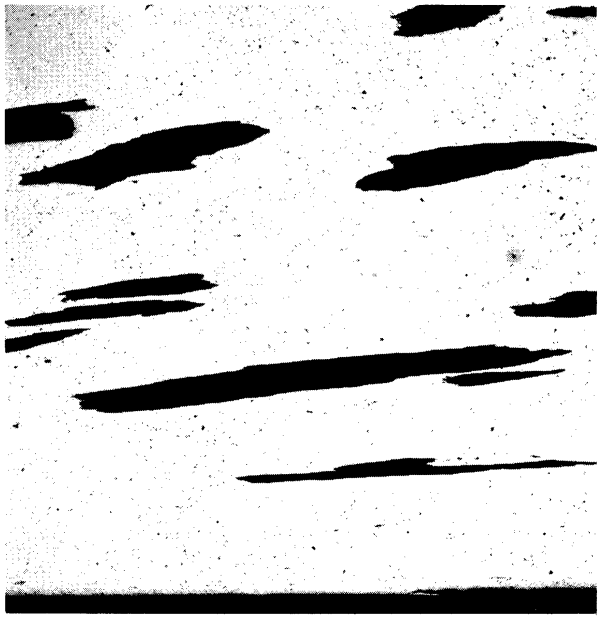

c) Sample: 90 Cu - 10 NaF.

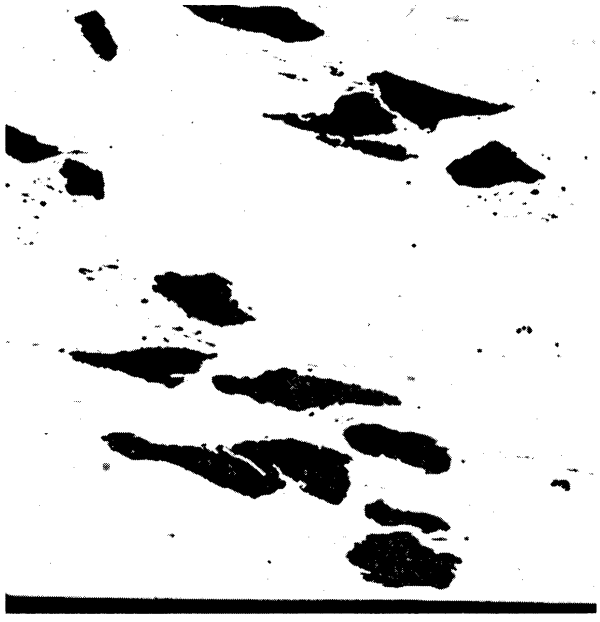

d) Sample: 90 Cu - 10 LiF.

Figure 67. Microstructures Illustrating the Effect of Inclusion Type on Inclusion Deformation. Die: 90° -75% reduction. 37.5X.

KCl, NaCl, and NaF inclusions deformed more than the copper matrix (8/1) while the converse was true for LiF inclusions (Figure 64). Many of the inclusions fractured during extrusion of the 90 Cu - 10 LiF sample.

8. Effect of Matrix Type

(Data and figures: 90° - 75 per cent reduction dies, 10 per cent NaCl - balance Pb, Al, Ag, Cu, or 75-35 brass samples, Figures 68 through 72)

Both average and final matrix hardness values were used as an index of the matrix properties. The average hardness values plotted are the average of the matrix hardness values before and after extrusion while the final hardness is the average matrix hardness in the extruded samples. The L/W values measured at the sample center were corrected for the L/W ratios in the as-sintered samples and they are presented in Figure 69(a).

As the matrix hardness increases, the following effects were observed:

1. The amount of inclusion deformation increases (Figures 68 and 69). NaCl inclusions in copper deform more than in an aluminum or silver matrix. However, the correction for as-sintered L/W ratio must be made for this result to be obvious (Figures 69(a) and (b)).
2. After a rapid initial increase in the amount of inclusion deformation, the rate of increase becomes constant at a lower value (Figure 69).

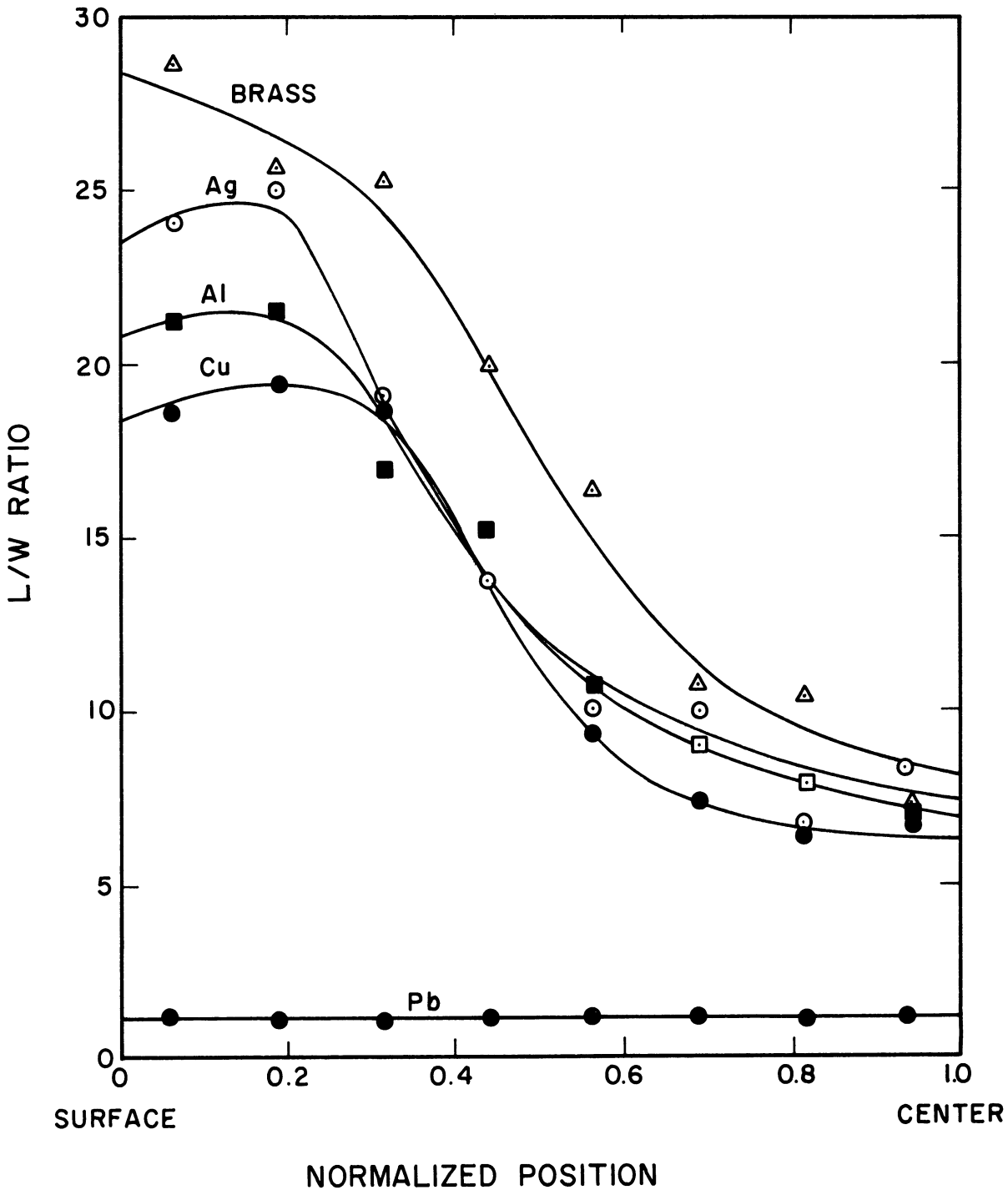

Figure 68. L/W Traverses for Matrix Type Study Samples.

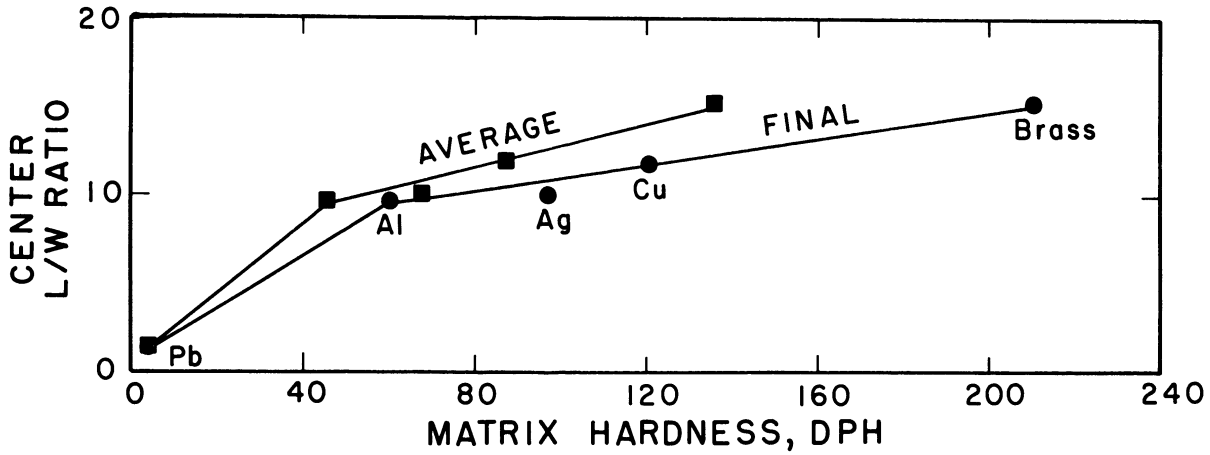

a) Corrected center L/W ratio versus matrix hardness

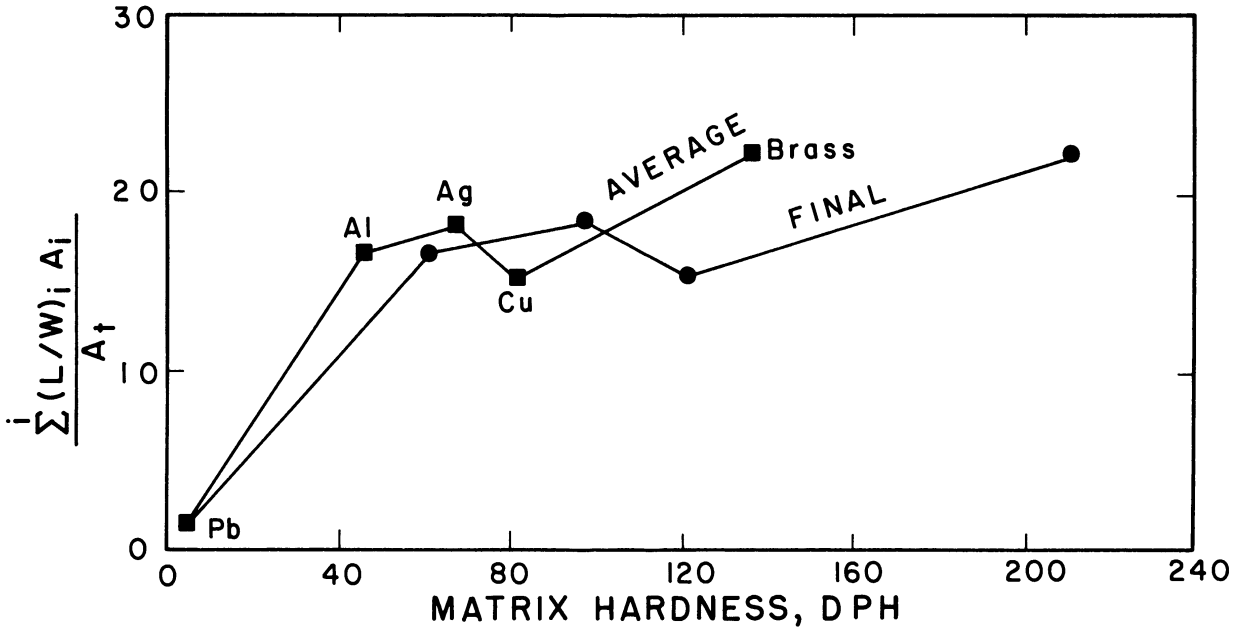

b) Measured "mean L/W ratio" versus matrix hardness

Figure 69. Inclusion Deformation versus Matrix Hardness.

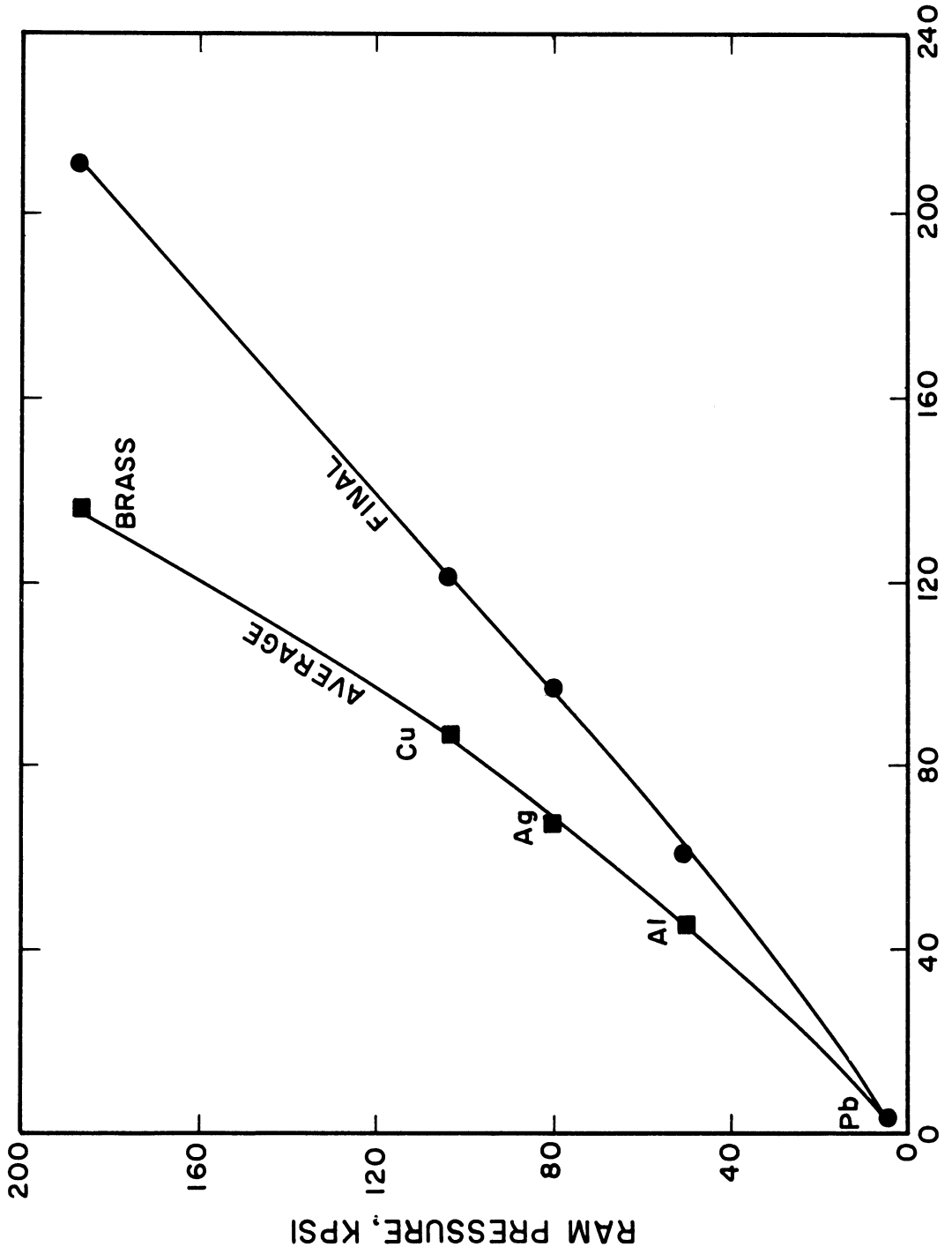

Figure 70. Ram Pressure versus Matrix Hardness.

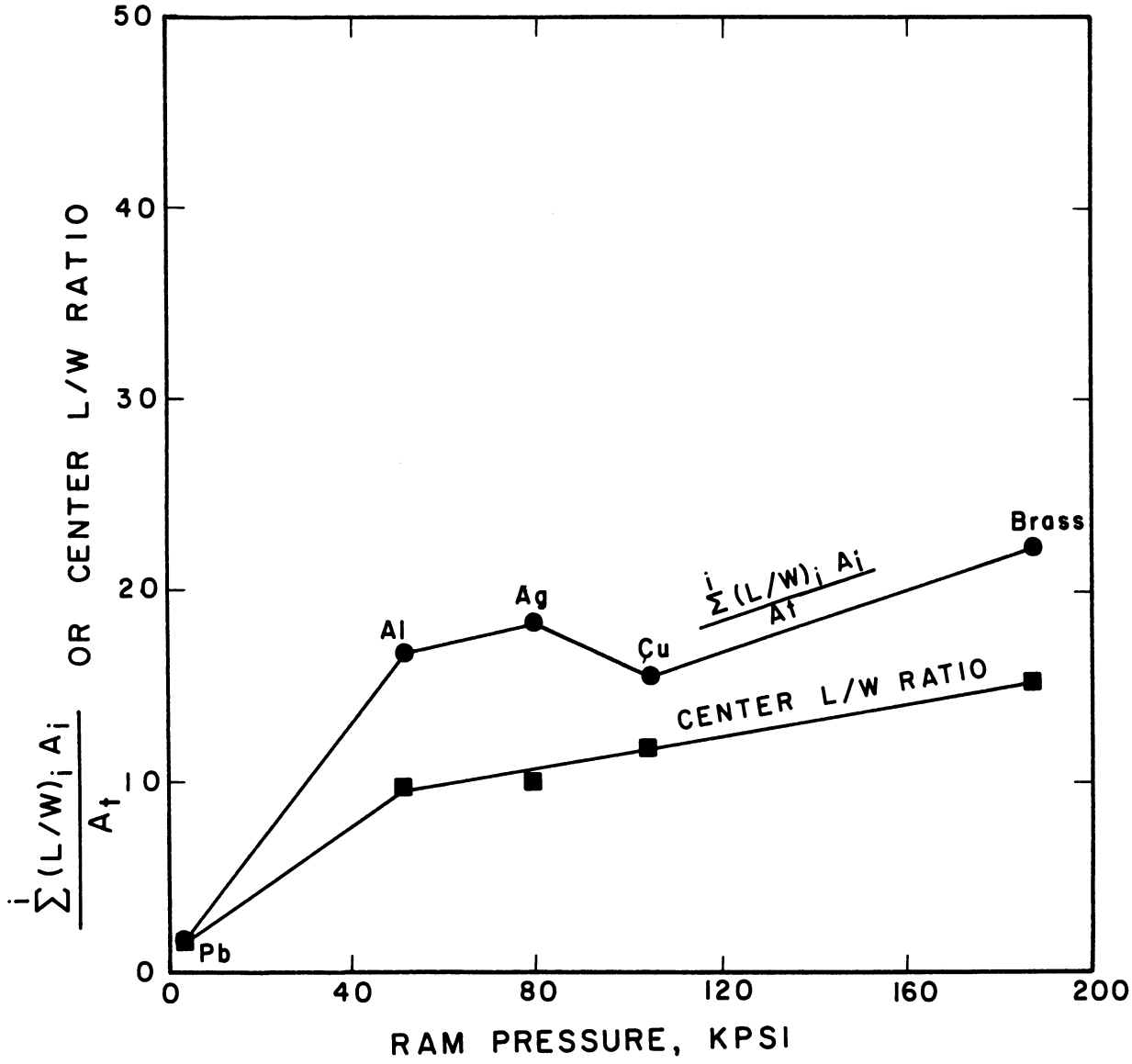

Figure 71. Inclusion Deformation - Ram Pressure Relationship for Matrix Type Study Samples.

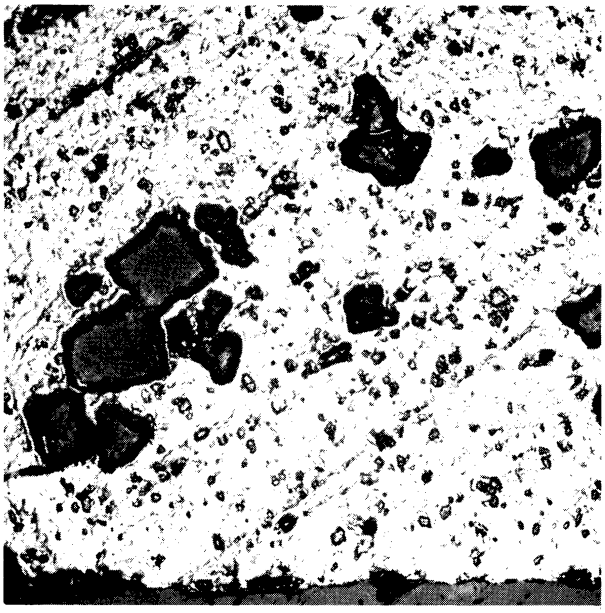

a) Sample: 90 Pb - 10 NaCl.

b) Sample: 90 Al - 10 NaCl.

c) Sample: 90 Ag - 10 NaCl.

d) Sample: 90 Brass - 10 NaCl.

Figure 72. Microstructures Illustrating the Effect of Matrix Type on Inclusion Deformation. Die: 90° -75% reduction. 37.5X.

3. Essentially no inclusion deformation occurs for the lead matrix. For the aluminum, silver, copper, and brass matrices, the amount of inclusion deformation is greater than the amount of matrix deformation (Figures 68 and 69).
4. Ram pressure increases (Figure 70).

CHAPTER VI

DISCUSSION OF RESULTS

The experimental results will be discussed under the following headings:

A. Strain Hardening Patterns.

B. Flow Patterns.

C. Calculated Stress Distributions.

D. Effects of Extrusion Parameters on Inclusion Deformation.

E. Plastic Deformation and Fracture.

Conclusions are listed at the end of each section.

A. Strain Hardening Patterns

The strain hardening patterns shown in Figure 21 can be explained on the basis of the shear stress levels developed in the samples. For the 60° and 90° dies, the samples slide along the lubricated die surface while for the 135° and 180° dies, shear occurs through the samples. Consequently, as the die angle increases, the shear stress levels in the samples increase. This conclusion is consistent with the results of Sachs and Eisbein[95] and Johnson.[109] The former show that the amount of sample distortion near the sample surface increases with increasing die angles. Johnson[109] states that lubricated slip over the die face occurs for included angles up to about 120°.

As the die angle increases, (1) the strain hardening patterns become more complex, and (2) the hardness increases near the die lips. These changes are a consequence of increasing shear stress levels in the samples.

The softer regions near the die-container junction for the 135° and 180° dies are the result of shear occurring through the sample. For these die angles, the samples essentially form their own die surface behind the die lips. Consequently, the amount of strain and strain hardening ahead of this internal surface is reduced. The region ahead of this internal shear surface is the so-called "dead" metal region.

The same over-all stress distribution would be expected for the same die angle, even with different reductions in area. This is evidenced by the similarities in the strain hardening patterns for the 55.5 and 75 per cent reduction dies (Figure 22). As would be expected for heavier reductions, the hardness values for corresponding normalized positions are greater for the 75 per cent reduction die.

Strain hardening near the container wall is a consequence of sliding friction between the sample and the container. The hardness increase behind the die entrance is greater than the increase between the die lips. The annealed sample hardness was approximately 40 DPH. Observation of the strain hardening patterns indicates that appreciable hardening occurs even in regions where no macroscopic flow occurred. This result suggests that appreciable hardening can occur under the influence of high confining pressures without appreciable plastic flow. Since the samples fit the chamber snugly, the hardening is not caused by flow perpendicular to the extrusion direction. The observed hardening is not the result of a second phase on sample densification since high purity copper bar stock was used for the samples.

It was found experimentally that 90 Cu - 10 NaCl compacts could be hardened by pressing in a closed die (Figure 9). The matrix hardness

increased from 25 to 90 DPH under a pressure of 126,000 psi. These samples fit the pressing die snugly. However, in these samples the density was approximately 94 per cent of theoretical and a softer second phase was present. Consequently, some strain could be expected during pressing.

The evidence is strong that copper can be hardened by the application of high hydrostatic pressures. However, further experimental work would be required to establish this as fact.

Conclusions - (Strain hardening patterns):

1. As the die angle increases, the shear stress levels near the sample surface increase.
2. "Dead" metal zones are formed for 135° and 180° dies. Shear surfaces are formed within the sample.
3. Strain hardening patterns are quite complex. Consequently, it seems unlikely that simple strain hardening pattern equations can be developed for use with the current extrusion theories.
4. There is evidence that materials can be hardened by the application of high confining pressures.

B. Flow Patterns

The flattening of the inclusions behind the die entry is a consequence of nonhydrostatic behavior of the matrix. The stresses in the extrusion direction are greater than those normal to the die wall. For the same pressure, a weaker material would be expected to behave more hydrostatically. Consequently, the amount of inclusion flattening would be expected to decrease as the matrix yield strength decreases as observed for the data in Table IV.

The other observations on inclusion flow are consistent with the flow patterns for gridded tin presented by Sachs and Eisbein.[95] For their approximately 90° included angle die, the bulk of the deformation of a square element occurs in the region of a line normal to the die wall and originating at the die lips. Flow is not directed toward the apex of a cone formed by extending the die lips as is assumed for some extrusion theories.

The increase in inclusion L/W ratio as the sample surface is approached results from the shear stress distribution. This will be discussed more fully in section D-1 of this chapter.

The stress component directions referred to in the ensuing discussion are presented in Figure 6. The inclusion length in a circumferential (Θ) direction was not observed to vary significantly across a cross section (Figure 24(b)). Thus, the inclusion length in a circumferential direction is approximately equal to the inclusion width at the sample center. This width can be measured in a symmetry plane parallel to the extrusion direction. Consequently, L/W measurements in a symmetry plane parallel to the extrusion direction are a good index of the amount of inclusion deformation.

For Shield's[111] stress analysis $\sigma_\varphi = \sigma_\Theta$. For $\tau_{R\varphi} < \sigma_o/\sqrt{3}$, σ_R is more tensile (or less compressive) than σ_φ and σ_Θ. The inclusion deformation at the sample center is a consequence of these stress components. As the sample surface is approached, the samples thin rapidly in the φ direction under the influence of the shear stress $\tau_{R\varphi}$. There is no shear stress component in a plane perpendicular to the Θ direction. Inclusion deformation is controlled by both the difference between σ_R and $\sigma_\varphi = \sigma_\Theta$ and by $\tau_{R\varphi}$.

$\tau_{R\varphi}$ increases as the sample surface is approached and results in a decrease in the difference between σ_{φ} and σ_R. Where there are moderate to large shear stress values, the inclusion L/W ratio increases markedly as the sample surface is approached (section D-1 of this chapter). Consequently, the shear stress level has a major effect on the amount of inclusion deformation. The amount of inclusion deformation can be minimized by minimizing $\tau_{R\varphi}$.

Conclusions - (Flow patterns):

1. Observed inclusion flow patterns are consistent with the flow patterns observed for gridded tin by Sachs and Eisbein.(95)
2. Inclusion flow patterns for 90° and larger angle dies indicate that flow is not directed toward the virtual apex of the cone formed by extending the die lips. Consequently, the assumption of this flow pattern in an extrusion theory for large angle dies would only serve as a rough first approximation.
3. Inclusion length in the circumferential direction does not appear to be a function of the position of the inclusion in the cross-section.
4. L/W ratios measured in a symmetry plane parallel to the extrusion direction are a good index of the amount of inclusion deformation.
5. Inclusion deformation is controlled by both $\tau_{R\varphi}$ and the difference in σ_R and $\sigma_{\varphi} = \sigma_{\theta}$.

6. For large values of $\tau_{R\varphi}$, the shear stress can have a much greater effect on the amount of inclusion deformation than the $\sigma_\varphi - \sigma_R$ difference.
7. For a given sample type and reduction, the amount of inclusion deformation can be minimized by minimizing the shear stress ($\tau_{R\varphi}$).

C. Calculated Stress Distributions

Lubricated slip along the die face occurs for the 60° and 90° dies (section A of this chapter). The shear stress calculated from the modified analysis for these dies reached $\sigma_o/\sqrt{3}$ well inside the sample which indicates shear through the sample. Consequently, the calculated stress distributions do not accurately describe the stress state in the sample. For this reason, no attempt was made to correlate inclusion strain with the calculated stress components.

The failure of the calculations is a result of the failure to consider the contribution of the end effects to the ram pressure. An accurate method of determining the contribution of the end effects to ram pressure must be established before Shield's stress analysis can be applied to practical extrusion problems. This statement in no way effects the validity of Shield's stress analysis.

The contribution of the end effects to ram pressure is large for a 90° - 75 per cent reduction die. The final matrix yield strength was used in the calculations for Figure 29. For the determination of the constant C, this yield strength overestimate is equivalent to a 38 per

cent reduction in the ram pressure. As shown in Figure 29, this reduction does not reduce the shear stress levels enough.

Figure 25 was determined for a nonstrain hardening matrix (Pb). Figure 26 was determined for a material with high strain hardening qualities (Cu), using the average of the initial and final yield strengths for the calculation of the constant C. The fact that these figures are almost identical indicates that use of the average sample yield strength for the calculation of C would yield satisfactory results for a strain hardening material. This value could be used to determine the value of each stress component divided by $\bar{\sigma}_o$. The yield strength value at each position in the sample would have to be used to accurately evaluate the individual stress components.

As the die angle increases, the size of the $\tau_{R\varphi} = \sigma_o/\sqrt{3}$ region increases. This is a consequence of both increased shear stresses in the sample and increased stress required to change the direction of material flow at the die entry and exit sections.

Conclusions - (Calculated stress distributions):

1. For 75 per cent reduction dies, the stress required to change the direction of material flow at the die entry and exit sections is a moderately large portion of the ram pressure (> 38 per cent for a 90° - 75 per cent reduction die).
2. An accurate method of determining the contribution of the end effects to ram pressure must be established before Shield's stress analysis[111] can be applied to practical extrusion problems.

3. For Shield's stress analysis, the use of an average yield strength value for the calculation of the constant C would yield satisfactory results.

D. Effects of Extrusion Parameters

In this section, the effects of individual extrusion parameters will be considered under the following headings:

1. Die Angle.
2. Per Cent Reduction.
3. Strain Rate.
4. Temperature.
5. Per Cent Nonmetallic Material.
6. Nonmetallic Inclusion Size.
7. Inclusion Type.
8. Matrix Type.

Copper - NaCl samples were used to study a number of the extrusion parameters. In all cases, the NaCl inclusions deformed more than the copper matrix. The greater NaCl deformation results from the fact that NaCl has a lower hardness and yield strength than copper.

1. Die Angle

The effect of die angle can be explained on the basis of the stress distribution in the sample as discussed in sections A and B of this chapter. Near the sample center, the shear stress level is low. Consequently, the amount of inclusion deformation depends on the $\sigma_\varphi - \sigma_R$ difference. At the sample center, this difference is the same for all die angles and a fixed reduction in area. Thus, the same center L/W

ratio would be expected for the samples as is observed in Figure 32. As the sample surface is approached, the shear stress levels increase with increasing die angles resulting in increased inclusion deformation.

In deforming composite samples, the $\sigma_\varphi - \sigma_R$ difference results in a minimum amount of inclusion deformation. This minimum amount of deformation is illustrated by the results for the 60° die where the amount of inclusion deformation is approximately constant across the sample. As the shear stress levels increase, the amount of inclusion deformation rapidly exceeds this minimum value. Consequently, inclusion deformation can be minimized by minimizing the shear stress levels in the sample.

The increase in ram pressure with increasing die angle is a consequence of two factors. As the die angle increases, the change in direction of material flow at the die entry and exit sections increases. As the die angle increases, the shear stress level increases. Both factors increase the required extrusion pressure.

Shear occurs through the sample for both the 135° and 180° dies. As a result, the rate of ram pressure change decreases between these two die angles.

As seen in the foregoing discussion, a process change which reduces shear stress levels will markedly reduce inclusion deformation and ram pressure. Process changes which lower the shear stress level include:

1. Use of more effective lubricants.
2. Use of lower angle dies for extrusion and drawing operations.

Conclusions - (Die angle):

1. Ram pressure and inclusion deformation can be minimized by reducing the shear stress levels in the samples. Shear stress levels can be reduced by the use of more effective lubricants and proper deformation equipment design.

2. Per Cent Reduction

The total sample strain and the stress level transmitted to the inclusions increase with increasing sample reductions. Thus, inclusion deformation would be expected to increase with increasing sample reductions as is observed in Figure 38.

As the reduction increases, the amount of work increases resulting in the ram pressure data shown in Figure 39. The experimental ram pressure data fit an equation of the form

$$RP = a \log_e\left(\frac{A_i}{A_f}\right) - b \qquad (38)$$

where a and b are constants. The linear dependence of the ram pressure on $\log_e (\frac{A_i}{A_f})$ is in agreement with results presented by Pearson and Parkins[92] and Johnson.[107] Since strain hardening increases with increasing reductions, a plot of $RP/\bar{\sigma}_o$ would have a slightly flatter slope than that presented in Figure 39(b).

The slopes of the inclusion deformation and ram pressure curves increase rapidly with increasing reductions. As a result, several reductions, rather than one large reduction, would reduce the ram pressure requirements. Several reductions would also be expected to reduce the amount

of inclusion deformation. Pearson and Parkins[92] show that the ram pressure is a linear function of $\log_e (\frac{A_i}{A_f})$ for strain hardening and nonstrain hardening materials. Thus, the stress transmitted to the inclusions is a linear function of $\log_e (\frac{A_i}{A_f})$. As a result, less inclusion deformation might be expected if several reductions were used. This conclusion was not verified experimentally.

Conclusions - (Per cent reduction):

1. Inclusion deformation and ram pressure can be reduced by reducing the amount of sample deformation.
2. There is evidence that several reductions, rather than one large reduction, might reduce the amount of inclusion deformation. However, this was not verified experimentally.
3. Ram pressure is a linear function of $\log_e (\frac{A_i}{A_f})$.

3. Strain Rate

Inclusion deformation increases with increasing strain rate (Figure 43). Since the bulk sample deformation remains constant, the amount of matrix deformation decreases. This result suggests that the rate of inclusion strain hardening increases less rapidly than that of the matrix for increasing strain rates.

The slopes of the strain hardening curve ($d\sigma/d\epsilon$) increase significantly with increasing strain rates ($\dot{\epsilon}$) for both metals[120] and NaCl type ionic solids.[39] Approximately a two-fold hardness increase occurred for pure NaCl which was extruded through a 90° - 75 per cent reduction die while a five-fold hardness increase occurred for pure copper. Thus, for the

same strain, copper strain hardens much more rapidly than NaCl. Therefore, the quantity $d(d\sigma/d\epsilon)/d\dot{\epsilon}$ would be expected to increase more rapidly for copper than NaCl.

The increase in ram pressure with increasing strain rate is a result of the increase in the rate of strain hardening. A linear relationship exists between $\log_e$ (RP) and $\log_e$ (extrusion velocity) which is in agreement with the empirical relationship presented by Pearson and Parkins[92] (Equations (24) and (25) in Chapter II).

Conclusions - (Strain rate):

1. Ram pressure and inclusion deformation increase with increasing strain rates.
2. A linear relationship exists between $\log_e$ (RP) and $\log_e$ (extrusion velocity).

4. Temperature

The shape of the L/W profiles changesabove 200°F (Figure 47), probably as a result of a change in the coefficient of friction at the sample surface. The stearic acid lubricant melts below 200°F and boils at 721°F. Consequently, as the extrusion temperature increases, there is a range where the stearic acid portion of the lubricant is liquid while at higher temperatures, most of the lubrication is due to the graphite. These changes in the character of the lubricant would be expected to have some effect on the amount of inclusion deformation and ram pressure. However, the results indicate that this effect is not large. The effect of the lubricant is minimized at the center of the sample. As shown in Figure 47, the center inclusion L/W values have the same temperature dependency as the surface L/W values.

On of the most interesting effects of temperature is the shape of the inclusion deformation-temperature curve (Figure 48). There is a minimum in this curve at approximately 300°F. This minimum would not be expected on the basis of the ram pressure curves (Figure 49) or the hardness curves (Figures 50 and 52) for the individual phases. However, the final inclusion hardnesses show that a maximum inclusion hardness occurs at 300°F (Figure 51). Consequently, the L/W minimum at approximately 300°F is the result of an increase in the inclusion hardness.

At elevated temperatures, the inclusion hardness values would be below the values measured at room temperature. The L/W increase with temperature above 300°F is a result of decreasing inclusion hardness and yield strength values. In general, the amount of inclusion deformation increases as the metal/inclusion hardness ratio increases. This will be demonstrated in section E of this chapter.

The exact reason for the intermediate temperature hardness increase is not known. It is not associated with pure NaCl, as indicated by the ram pressure curve (Figure 49) or the hardness curves (Figures 50 and 52). Consequently, it must be caused by an impurity picked up from the copper during sintering.

To check this, Harshaw NaCl single crystals were heat treated under copper powder for 30 hours. After heat treatment, they were rapidly cooled to room temperature. The room temperature hardness was approximately 3 DPH greater than that shown in Figure 52. The hardness differential increased up to approximately 500°F and was time dependent. These results suggest that an impurity was picked up from the copper which leads to a precipitation hardening reaction. Precipitation hardening and overaging would be consistent with the hardness values shown in Figure 51. The

hardness increase observed for the Harshaw NaCl single crystals was not as large as that observed for the inclusions. However, the Harshaw crystals were much larger. Thus, the amount of impurity diffusing into the Harshaw crystals is probably much smaller.

For 90 Cu - 10 NaCl samples, the shape of the ram pressure curve is controlled primarily by the copper matrix. As temperature increases, the amount of strain hardening and hot hardness decrease and thus the yield strength and ram pressure decrease. This is also true for the pure copper and pure NaCl samples (Figure 49).

For the copper sample, the change in the ram pressure slope between 700° and 1100°F is a result of recrystallization. In contrast, the hardness curve for copper indicates that recrystallization is complete at 920°F (Figure 50). The difference in the recrystallization range between the ram pressure and hardness curves results from the time dependence of recrystallization. The samples were at temperature for approximately five minutes after extrusion was finished.

The ram pressure required to extrude the 90 Cu - 10 NaCl sample is less than that required to extrude the pure copper sample. Since NaCl has a lower yield strength than copper, the addition of NaCl lowers the sample yield strength and the required extrusion pressure.

The hot hardness curves for annealed, high purity copper and NaCl have the anticipated shape. As temperature increases, interatomic spacing increases, and dislocation motion is easier. As a result, the hot hardnesses of high purity Cu and NaCl decrease smoothly with increasing temperature. The hot hardness data indicates that the intermediate temperature increase in yield strength which was reported for impure NaCl by Ekstein[42] and Eshelby, et al.,[41] does not occur for pure NaCl.

Conclusions - (Temperature):

1. The amount of inclusion deformation is dependent on the inclusion hardness (yield strength). In general, the amount of inclusion deformation decreases with increasing inclusion hardness.
2. Ram pressure decreases with decreasing hardness and yield strength of the sample. Since yield strength generally decreases with increasing temperature, ram pressure generally decreases with increasing temperature.
3. The addition of a softer inclusion phase to a material decreases the sample yield strength and the pressure required for extrusion.
4. The hardnesses of annealed, high purity copper and NaCl decrease smoothly with increasing temperature.

5. Per Cent Nonmetallic Material

The shape of the L/W traverses are almost the same for all NaCl volume fractions and thus it follows that the stress distributions are approximately the same. The stress level in a sample decreases with increasing NaCl volume fractions, as indicated by Figure 56. Thus, as the stress level transmitted to the inclusions decreases, the amount of inclusion deformation decreases (Figure 55).

Copper strain hardens more than NaCl for equivalent strains. As the copper volume fraction increases, the amount of copper deformation increases and the hardness differential between the copper and the NaCl increases. As the hardness differential increases, the stress transmitted

to the NaCl increases relative to the yield strength of NaCl. Thus, the curve for NaCl deformation curves upward as the NaCl volume fraction is reduced. If the inclusion material were more rigid than the matrix, the opposite effect would be expected. As the volume fraction of the harder inclusion material increased, the inclusion L/W ratio would increase.

The linear decrease in ram pressure (Figure 56) indicates a linear decrease in the average sample yield strength. Since the ram pressure line runs between the ram pressures of the two pure components, the average yield strength of the two-phase system is given by

$$\sigma_{SAMPLE} = \sigma_{Cu} f_{Cu} + \sigma_{NaCl} f_{NaCl} \qquad (39)$$

where σ is the average yield strength and f is the volume fraction of the indicated phases. The inclusions are relatively large and noncoherent. This linear relationship would not be expected for very small, hard inclusions.

Conclusions - (Per cent nonmetallic material):

1. A decrease in the amount of the metal matrix reduces inclusion deformation when the inclusion is the softer of the two phases. The converse is true when the inclusions are harder than the metal matrix.
2. Ram pressure decreases linearly with decreasing average sample yield strengths.

6. Nonmetallic Inclusion Size

Inclusion deformation was observed to decrease very slowly as inclusion size increased (Figure 60). As inclusion size increases,

the amount of copper strain hardening near an inclusion would decrease slightly since NaCl deforms more than the copper matrix. This results in a slight decrease in the stress acting on the inclusions as inclusion size increases and explains the observed data trend. For an inclusion which deforms less than the matrix, the opposite effect would be expected; i.e., inclusion deformation would increase slightly for increasing inclusion sizes as observed experimentally by Pickering.(79) Scheil(80) reported no size effect for Cu_2S in copper which is not inconsistent with the above interpretation for the scatter in his data. In any event, inclusion deformation does not change appreciably with inclusion size changes.

The ram pressure was independent of inclusion size for inclusion diameters down to 48 microns (Figure 61). The mean free path for the 48 micron NaCl inclusions is approximately 300 microns. Edelson and Baldwin(88) state that the second phase must be harder than the matrix for particle strengthening to occur. Softer, noncoherent inclusions would not be expected to cause significant dislocation pile-ups and particle strengthening. For a hard inclusion phase, particle strengthening would be expected for low intraparticle mean free paths. The mean free path required for hardening would increase as the particle coherency increased.

The fact that ram pressure does not change with particle size suggests that average sample yield strength is determined by the volume fractions of the sample phases. This result would not be expected for fine, coherent, harder second phases.

Conclusions - (Nonmetallic inclusion size):

1. Inclusion deformation is almost independent of inclusion size. The results show a slow decrease in inclusion deformation with increasing inclusion size.
2. Ram pressure is independent of inclusion size. This result would not be expected for very fine, hard, coherent inclusions.
3. Average sample yield strength is determined by the volume fraction of the phases present. Again, this result would not be expected for very fine, hard, coherent inclusions.

7. Inclusion Type

For a fixed matrix type, inclusion deformation decreases with increasing inclusion hardness values. This result would be expected since inclusion yield strength increases with increasing inclusion hardness.

The final hardness values for the copper matrix range from 120.8 to 136.5 DPH. The results indicate that a harder inclusion (LiF) deforms less than the matrix (Figure 64) while the converse is true for softer inclusions (KCl, NaCl, NaF). These results are a consequence of the relative yield strengths of the two phases.

The ram pressure required to extrude pure copper is 110,000 psi. The results presented in Figure 65 indicate that the addition of a second phase, which is harder than the matrix, increases the ram pressure while the converse is true for a softer second phase. Since ram pressure is linearly proportional to the average sample yield strength, the results

show that the addition of a harder second phase increases the average yield strength of a material. The converse is true for softer inclusions. This result would be expected for two reasons:

1. The harder inclusions add to the yield strength on a volume fraction basis.
2. As the inclusion hardness increases, the amount of inclusion deformation decreases. Thus, for a fixed sample strain, the amount of matrix strain increases as the inclusion hardness increases and the amount of matrix strain hardening would increase.

Conclusions - (Inclusion type):

1. For a fixed matrix type, inclusion deformation decreases with increasing inclusion hardness.
2. Inclusions which are harder than the matrix will deform less than the matrix. The converse is true for softer inclusions.
3. The addition of a harder second phase increases the average yield strength of a sample while the converse is true for the addition of a softer second phase.
4. Ram pressure increases as the average sample yield strength increases.

8. Matrix Type

The stress levels acting on the inclusions increase as the matrix hardness increases. Consequently, the amount of inclusion deformation increases (Figure 69). This trend is not fully evident until the

measured L/W ratios are corrected for the L/W ratios in the as-sintered samples.

The lead matrix is softer than the NaCl inclusions while the converse is true for the other matrix materials studied. When the matrix is softer than the inclusions, the matrix undergoes more deformation than the inclusions (Figure 69). The converse is true for matrix materials which are harder than the inclusions.

The sample yield strength increases with increasing matrix hardness and results in an increase in the average sample yield strength.

Conclusions - (Matrix type):

1. Inclusion deformation increases as the matrix hardness increases.
2. When the matrix is softer than the inclusions, the matrix undergoes more deformation than the inclusions. The converse is true for matrix materials which are harder than the inclusions.
3. Ram pressure increases as the average yield strength of the sample increases.

E. Plastic Deformation and Fracture

The high ductility possible for NaCl type ionic solids is illustrated by the L/W results presented in section D of Chapter V. Inclusions which are softer than the matrix are more highly deformed than the matrix. Final NaCl L/W ratios of several hundred to one were obtained using a 180° - 75 per cent reduction die. Consequently, with the proper stress state, NaCl-type ionic solids have high ductilities.

The results for inclusion type and matrix type suggest that inclusion deformation is controlled, at least in part, by the relative hardnesses of the inclusion and matrix involved. To show the correlation more clearly, corrected center L/W ratios were plotted as a function of metal/inclusion hardness ratio (Figure 73). The center L/W ratio was used since a correction must be made for the varying L/W ratio in the as-sintered samples. The hardness of each phase, before and after extrusion, was averaged to obtain the values plotted.

As indicated in Figure 73, three types of inclusion behavior are observed as the metal/inclusion hardness ratio increases. These types of inclusion behavior can be classified as follows:

1. Rigid behavior. Neither deformation nor fracture occur.
2. Brittle-ductile behavior. Both deformation and fracture occur. In this region, the amount of inclusion deformation increases and the amount of fracture decreases as the metal/inclusion hardness ratio increases.
3. Ductile behavior. The inclusions are highly deformed plastically and fracture is almost nonexistent. However, highly deformed inclusions do fracture occasionally.

The three regions of inclusion behavior can be explained on the following basis. The inclusion hardness is directly related to the flow and fracture stress of the inclusions while stress is transmitted to the inclusions through the metal matrix. Consequently, as the matrix hardness increases, the stress level acting on the inclusions increases relative to the flow and fracture stress of the inclusions.

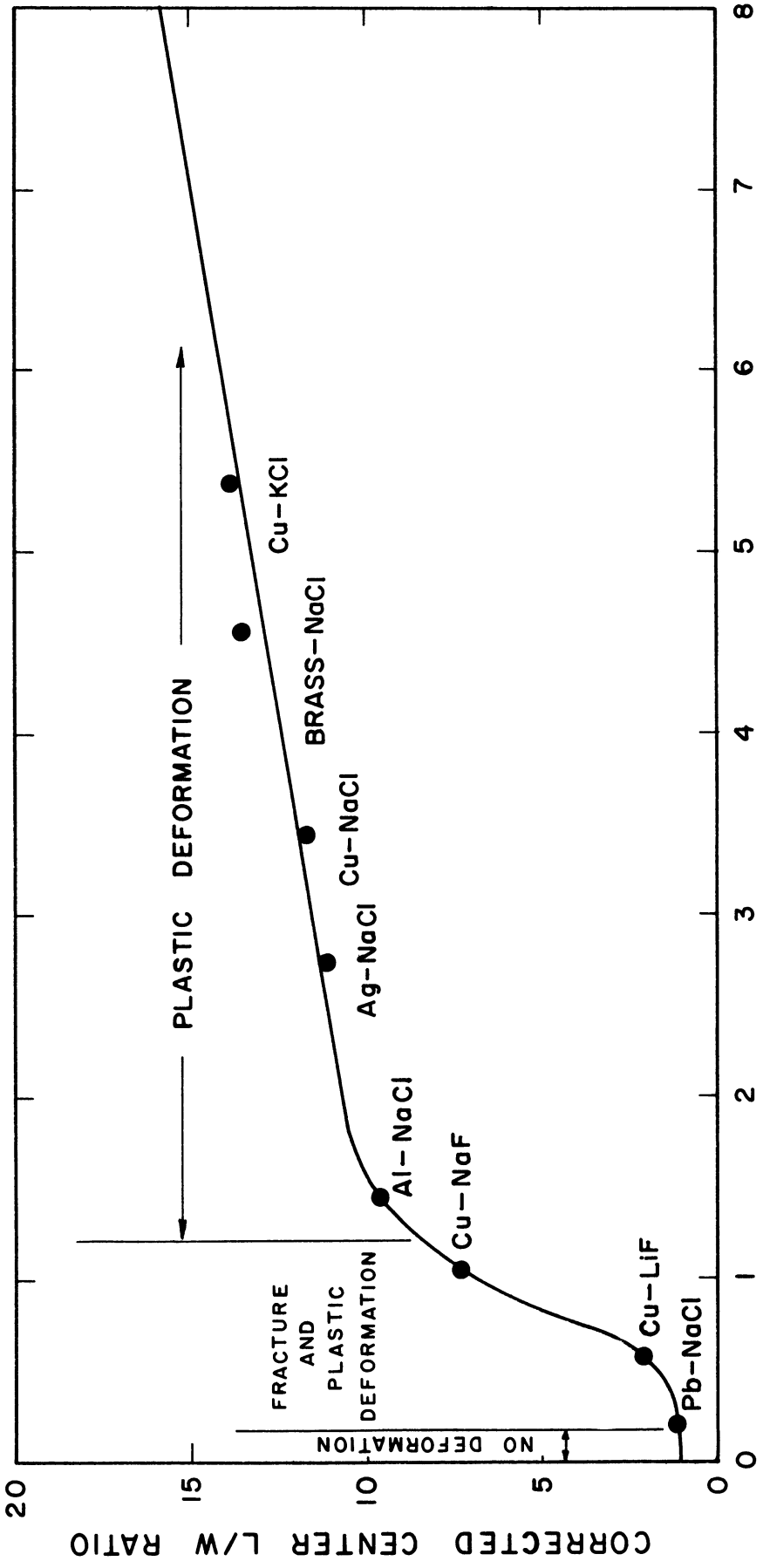

Figure 73. The Effect of Metal/Inclusion Hardness Ratio on Inclusion Deformation and Type of Inclusion Deformation Behavior.

For low metal/inclusion hardness ratios (M/I ratios), the stress transmitted to the inclusions is below the flow and fracture stress of the inclusions. Consequently, the inclusions behave as rigid bodies in the matrix.

For intermediate M/I ratios, the stress acting on the inclusion exceeds both the fracture and yield strengths. The hydrostatic stress levels are not high enough to prevent the development of pure tensile stresses in the inclusions, and fracture occurs. As the M/I ratio increases in this region, the hydrostatic stress levels increase. Thus, inclusion deformation increases, and the fracture tendency decreases.

For high M/I ratios, high hydrostatic stresses tend to prevent crack propagation. The stress levels are high relative to the yield strength of the sample and the inclusions deform readily.

The results from the temperature study should show the same deformation behavior since the same die was used. Unfortunately, the phase hardness values are not known at temperature. The room temperature hardness values were extrapolated on the basis of the derivation presented in Appendix E and the results are presented in Figure 74.

The extrapolation would be most valid for the -108, 80, and 1316°F points. These points follow the predicted behavior exactly. The precipitation hardening reaction shown in Figure 51 occurs in NaCl in the intermediate temperature range. Therefore, the slope of the $\log_e$ (hardness) vs. temperature plot would be expected to change from the slope obtained for pure NaCl in this temperature range. In addition, with an impurity picked up from the copper matrix, intermediate temperature NaCl yield strength increases could be expected. These intermediate temperature increases are predicted by Eshelby, et al.[41] if divalent ions

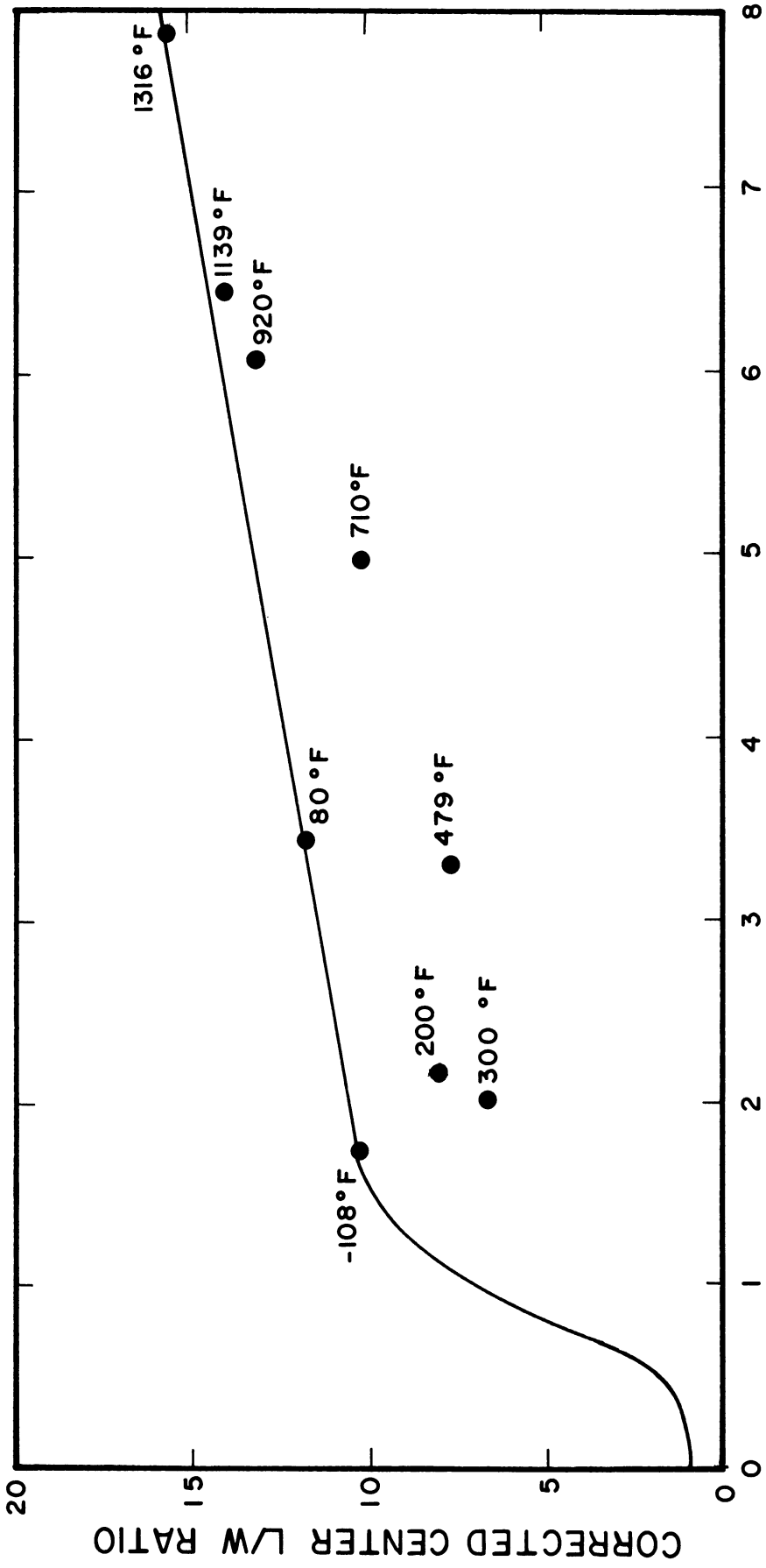

Figure 74. The Effect of Metal/Inclusion Hardness Ratio on Inclusion Deformation for Temperature Study Samples.

are present in the NaCl lattice. Both factors could increase the intermediate temperature inclusion hardness over the extrapolated values and improve the data fit.

While all of the data from the temperature study do not fall on the L/W curve predicted from Figure 73, the general trends are the same. The degree of agreement is all that can be expected within the limitations of the hot hardness estimates.

As the reduction in area increases, the shape of Figure 73 would be expected to change. The M/I ratio is indirect evidence of the stress level transmitted to the inclusions relative to the inclusion yield strength. Increasing the sample reduction increases the stress level acting on the inclusions which would not be evidenced by the M/I ratio in non-strain hardening materials. In these materials, an increase in sample reduction would have the same effect as an increase in the matrix hardness. The effect of other process variables on the shape of Figure 73 can be predicted on the basis of their effect on the stress levels transmitted to the inclusions.

Figure 73 is significant for two reasons. It shows the effect of stress level on inclusion behavior and it shows the effect of relative metal and inclusion properties on inclusion behavior. Consequently, Figure 73 enables predictions to be made about inclusion behavior. Any deformation parameter which changes the metal/inclusion hardness ratio will change the inclusion deformation behavior as shown in Figure 73. For a fixed sample type, the major parameter effecting the M/I ratio is temperature. Less significant changes can be obtained by varying the strain rate for strain hardening materials (see section D-3 of this chapter).

The following discussion applies for dilute inclusion concentrations. Sample deformation will not occur until the matrix yield strength is exceeded. Consequently, the initial M/I ratio for the sample [(M/I)s] is important. Types of inclusion deformation behavior shown in Figure 73 for M/I ratios lower than the $(M/I)_s$ ratio can not be obtained by increasing the sample reduction. However, the behavior range for higher M/I ranges can theoretically be reached by increasing the sample reduction. This is true for both strain hardening and non-strain hardening materials since, in general, the matrix strain hardens more rapidly than the inclusions. The same argument can be made for shear stress ($\tau_{R\varphi}$) levels in the sample. If the original $(M/I)_s$ value is in the deformation range, increasing the shear stress level will increase the amount of inclusion deformation. However, even when the shear stress level is reduced to zero, rigid or ductile-brittle behavior would not be expected. Consequently, for initially ductile inclusions, rigid behavior or fracture and dispersion could only be obtained by decreasing the M/I ratio for the sample.

In general, the shape of Figure 73 is at least qualitatively consistent with the results reported in the literature. (See section B of Chapter II.) Pickering[79] reported that iron oxide inclusions become increasingly plastic as the rolling temperature decreases from 1150 to 800°C. The author is not familiar with hot hardness data which would prove that this decrease is consistent with Figure 73.

Conclusions - (Plastic deformation and fracture):

1. With the proper stress state, NaCl-type ionic solids have high ductilities.

2. As the stress level transmitted to the inclusions increases, three types of inclusion deformation behavior are encountered.
   a. Rigid inclusions. No inclusion deformation occurs.
   b. Brittle-ductile inclusions. Both inclusion fracture and deformation occur.
   c. Ductile inclusions. High inclusion deformations occur.

   The zones where the various types of deformation behavior occur can be related to the metal/inclusion hardness ratios.
3. Figure 73 can be used to qualitatively predict the effect of sample and process changes on inclusion deformation behavior.
4. The ability to change the type of inclusion behavior is limited in part by the metal/inclusion hardness ratio. Inclusion behavior types occurring for M/I ratios lower than the sample M/I ratio can not be achieved by means other than changing the sample M/I ratio. The converse of this statement is not true.

CHAPTER VII

CONCLUSIONS

The conclusions will be summarized under the following headings: (A) Extrusion, and (B) Inclusion Deformation. A more detailed presentation of the conclusions is given at the end of the indicated sections of Chapter VI.

A. Extrusion

For 75 per cent reduction dies, the stress required to change the direction of material flow at the die entry and exit sections is a moderately large portion of the ram pressure. Consequently, an accurate method of determining the contribution of the end effects must be established before Shield's stress analysis can be applied to practical extrusion problems. (VI-C)

The ram pressure required for extrusion can be reduced by:

1. Reducing the shear stress levels at the material surface through use of more effective lubricants and proper deformation equipment design (VI-D-1).
2. Decreasing the amount of sample reduction (VI-D-2).
3. Decreasing the extrusion velocity (VI-D-3).
4. Increasing the extrusion temperature (VI-D-4).
5. Decreasing the yield strength of the material being extruded (VI-D-4, 5, 7, 8).

B. Inclusion Deformation

With the confined stress states which occur in extrusion, NaCl-type ionic solids can have high ductilities (VI-E). As the stress levels increase, three types of inclusion deformation behavior occur:

1. Rigid inclusions (neither fracture nor deformation occur).
2. Brittle-ductile inclusions (inclusion deformation and fracture occur).
3. Ductile inclusions (high inclusion deformations occur).

The minimum stress acting on an inclusion is governed by the metal/inclusion hardness ratio (VI-E).

The amount of inclusion deformation can be decreased by the following process and sample changes:

1. Decreasing the shear stress levels at the material surface by the use of more effective lubricants and proper deformation equipment design (VI-A, B, D-1).
2. Decreasing the total sample reduction (VI-D-2).
3. Decreasing the strain rate (VI-D-3).
4. Proper operating temperature selection (VI-D-4).
5. Changing the relative yield strengths of the two phases (VI-D-7, 8, E).
6. Changing the relative amounts of the two phases (VI-D-5).

Inclusion size does not have a major effect on the amount of inclusion deformation (VI-D-6).

APPENDICES

APPENDIX A

MEASURED VS. TRUE L/W RATIO FOR AN ELLIPSOIDAL INCLUSION

If the inclusions have an ellipsoidal shape, the measured and true L/W ratios are the same. The equation of an ellipsoidal inclusion is

$$\frac{x^2}{a^2} + \frac{y^2}{b^2} + \frac{z^2}{c^2} = 1 \tag{40}$$

where a, b, and c are constants equal to 1/2 of the major axis of the inclusion in the x, y, and z directions respectively (Figure 75). Since,

$$a = L/2 \tag{41}$$

and

$$b = W/2$$

where L and W are the inclusion length and width, we can write

$$\frac{(2x)^2}{L^2} + \frac{(2y)^2}{W^2} + \frac{z^2}{c^2} = 1 \tag{42}$$

The section through the inclusion in the plane of measurement has a constant value of z. Consequently, Equation (42) can be written as

$$\frac{(2x)^2}{L^2} + \frac{(2y)^2}{W^2} = 1 - \frac{z^2}{c^2} = E \tag{43}$$

where E is a constant for the plane of measurement. The measured length of the inclusion (ℓ_m) is 2x for y = 0. Consequently,

$$\ell_m = 2x = L\sqrt{E} \tag{44}$$

and

$$\omega_m = 2y = W\sqrt{E} \tag{45}$$

Dividing Equation (44) by Equation (45), we have

$$\frac{\ell_m}{\omega_m} = \frac{L}{W} \tag{46}$$

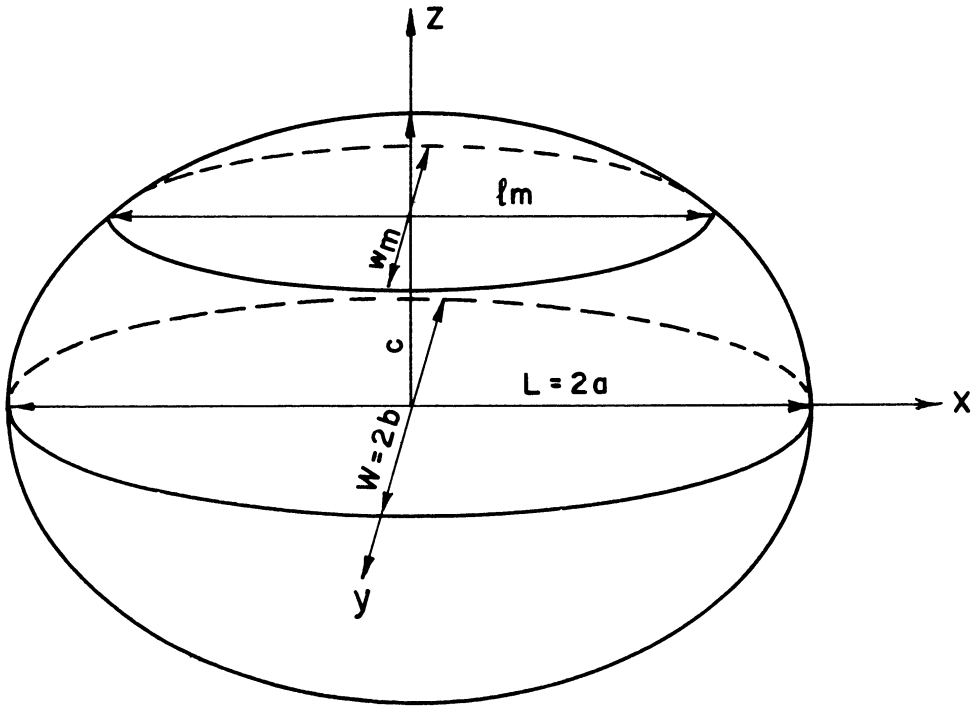

Figure 75. Section Through an Ellipsoidal Inclusion.

Consequently, for an ellipsoidal inclusion, the measured L/W value (ℓ_m/ω_m) is the true L/W value.

APPENDIX B

MODIFICATION OF SHIELD'S STRESS ANALYSIS

The stress analysis used is a modification of Shield's[111] analysis for plastic flow in a converging connical channel. In this appendix, the method is modified to apply to extrusion. This modification parallels that presented by Shield for wire drawing. The dimensions used for the analysis and the directions of the principal stress components are shown in Figure 6. The assumptions are the same as those presented by Shield.

1. General Equations

For the von Mises yield condition, the stress components are given by the equations

$$\tau_{R\varphi} = k\tau \tag{47}$$

$$\sigma_\varphi = \sigma_\theta = \sigma_R - k\sqrt{3(1-\tau^2)} = k\,g(R) - 3k\int \tau\, d\varphi \tag{48}$$

where

$$g(R) = -C\ \log_e(R) + A \tag{49}$$

and

$$k = \sigma_o/\sqrt{3} \tag{50}$$

The quantity $\tau(\varphi)$ is given by

$$\tau'(\varphi) + \tau\cot\varphi + 2\sqrt{3(1-\tau^2)} = C \tag{51}$$

A and C are constants of integration to be determined by the boundary conditions.

At the die surface,

$$\tau_{R\varphi} = m k \tag{52}$$

where m is a constant ≤ 1. Thus, the boundary conditions on $\tau(\varphi)$ are

$$\left.\begin{aligned} \tau(0) &= 0 \\ \tau(\alpha) &= m \end{aligned}\right\} \tag{53}$$

Since the coefficient of friction at the die surface is unknown, m is unknown.

2. Calculation of C

The constant C is determined from the condition at the die entrance (at Z_i). Here, the stress across the section is assumed to equal the extrapolated ram pressure (RP). The stresses at the die entrance and exit sections are given by

$$\sigma_{z_i} = -k C \log_e(Z_i) + k L(\varphi) \tag{54}$$

$$\sigma_{z_f} = -k C \log_e(Z_f) + k L(\varphi) \tag{55}$$

where

$$L(\varphi) = A + \frac{1}{2}\sqrt{3(1-\tau^2)}(1+\cos 2\varphi) - 3\int \tau d\varphi - \tau \sin 2\varphi \tag{56}$$

Subtracting (55) from (54), we have

$$\sigma_{z_i} - \sigma_{z_f} = k C \log_e\left(\frac{Z_f}{Z_i}\right) \tag{57}$$

Since the ram pressure is compressive, the mean extruding stress over the entrance section is given by

$$\pi Z_i^2 \tan\alpha\,(-RP) = \int_0^{\alpha} \sigma_{Z_i}\, 2\pi Z_i^2 \tan\varphi \sec^2\varphi \, d\varphi \tag{58}$$

For the mean stress over the exit section being 0, we have

$$\int_0^{\alpha} \sigma_{Z_f}\, 2\pi Z_f^2 \tan\varphi \sec^2\varphi \, d\varphi = 0 \tag{59}$$

The substitution of Equation (50) into Equation (58) leads to the result

$$\pi Z_i^2 \tan^2\alpha\,(-RP) = \int_0^{\alpha} \left[\sigma_{Z_f} + kC \log_e\left(\frac{Z_f}{Z_i}\right)\right] 2\pi Z_i^2 \tan\varphi \sec^2\varphi \, d\varphi \tag{60}$$

Cancelling like terms and using Equation (59), we have

$$\tan^2\alpha\,(-RP) = 2kC \log_e\left(\frac{Z_f}{Z_i}\right) \int_0^{\alpha} \tan\varphi \sec^2\varphi \, d\varphi \tag{61}$$

By noting that

$$\sec^2\varphi = \frac{d(\tan\varphi)}{d\varphi} \tag{62}$$

Equation (61) reduces to

$$-(RP) = kC \log_e\left(\frac{Z_f}{Z_i}\right) \tag{63}$$

Substituting Equation (50) in Equation (63) and solving for $\underline{C}$ leads to the result

$$C = \frac{\sqrt{3}\,(RP)}{\bar{\sigma}_o \log_e\left(\frac{Z_i}{Z_f}\right)} \tag{64}$$

Equation (64) yields the value of the constant $\underline{C}$ to be used in solving Equation (51).

3. Calculation of $\tau(\varphi)$

Equation (51) can not be solved directly to determine $\tau(\varphi)$. It was solved incrementally using a computer. The computation was started with the known boundary condition $\tau(0) = 0$. Using Equation (51) in the following form, the slope of the τ vs. φ curve was determined for $\tau = \varphi = 0$.

$$\frac{\Delta\tau}{\Delta\varphi} = C - \tau\cot\varphi - 2\sqrt{3(1-\tau^2)} \tag{65}$$

Multiplying the slope by a small $\Delta\varphi$ ($\Delta\varphi = \varphi_{j+1} - \varphi_j$), the value of was determined at φ_{j+1}. This process was continued to obtain corresponding values of τ and φ. Whenever τ was greater than 1, τ was taken as 1. A value of $\tau = 1$ corresponds to shear through the sample.

4. Calculation of the Constant A

The value of A must be known to solve Equations (48) and (49). This constant is determined from the fact that the mean stress at the die exit is equal to zero. From Equation (56), we have

$$2\pi Z_f^2 \int_0^{\alpha} \sigma_{z_f} \tan\varphi \sec^2\varphi \, d\varphi = 0 \tag{66}$$

σ_{z_f} is given by Equation (52) as

$$\sigma_{z_f} = -kC\log_e Z_f + k\left[A + \tfrac{1}{2}\sqrt{3(1-\tau^2)}(1+\cos 2\varphi) - 3\int\tau\,d\varphi - \tau\sin 2\varphi\right] \tag{67}$$

Substituting Equation (66) into (67) and solving for A leads to the result

$$A = \frac{\int_0^{\alpha}\left[C\log_e Z_f - \tfrac{1}{2}\sqrt{3(1-\tau^2)}(1+\cos 2\varphi) + 3\int\tau\,d\varphi + \tau\sin 2\varphi\right]\tan\varphi\sec^2\varphi\,d\varphi}{\int_0^{\alpha}\tan\varphi\sec^2\varphi\,d\varphi} \tag{68}$$

Equation (65) was solved incrementally using a computer.

5. Calculational Procedure

The stress values calculated are all divided by $\bar{\sigma}_o$. The following sequence of operations was used:

1. Calculate $\underline{C}$ from Equation (64).
2. Determine τ as a function φ using an incremental solution to Equation (51).
3. Determine the constant $\underline{A}$ from Equation (68) using an incremental solution.
4. Calculate $\tau_{R\varphi}/\bar{\sigma}_o$ from Equation (48).
5. Calculate $\sigma_R/\bar{\sigma}_o$, $\sigma_\varphi/\bar{\sigma}_o$, and $\sigma_\theta/\bar{\sigma}_o$ from Equations (48), (49), and (68).

APPENDIX C

EXPERIMENTAL RAM PRESSURE AND "MEAN L/W VALUE" DATA

Sample	Die*	Ram Pressure, K_{psi}	Measured $\frac{\sum_{i} (L/W)_i A_i}{A_t}$	Variable
90Cu-10NaCl	60°-75%	89.0	6.5	Die Angle
"	90°-75%	104.0	15.4	" "
"	135°-75%	126.0	38.2	" "
"	180°-75%	130.0	55.5	" "
"	90°-30.9%	25.1	4.5	Percent Reduction
"	90°-55.5%	65.0	6.6	" "
"	90°-73.5%	104.0	15.4	" "
"	90°-88.5%	173.6	43.3	" "
"	90°-75%	102.0	14.8	Ram Velocity(0.05ipm)
"	"	104.0	15.4	" " (0.10ipm)
"	"	106.6	17.2	" " (0.30ipm)
"	"	109.3	18.1	" " (0.71ipm)
"	"	137.5	15.0	Temperature(-108°F)
"	"	104.0	15.4	" (75°F)
"	"	86.3	10.5	" (200°F)
"	"	78.3	6.7	" (300°F)
"	"	76.1	--	" (395°F)
"	"	67.7	8.3	" (497°F)
"	"	60.5	13.5	" (710°F)
"	"	43.0	18.2	" (920°F)
"	"	24.9	20.3	" (1139°F)
"	"	24.5	24.6	" (1316°F)
95Cu-5NaCl	"	109.0	16.6	Percent NaCl
90Cu-10NaCl	"	104.0	15.4	" "
80Cu-20NaCl	"	90.5	12.5	" "
50Cu-50NaCl	"	67.5	9.9	" "
100NaCl	"	31.0	8.0	" "
90Cu-10NaCl	90°-75%	105.5	15.1	Inclusion Size(0.275mm)
"	"	104.0	15.5	" " (0.214mm)
"	"	100.5	14.0	" " (0.163mm)
"	"	100.0	15.6	" " (0.137mm)
"	"	102.8	16.0	" " (0.081mm)
"	"	103.5	14.7	" " (0.048mm)
90Cu-10KCl	"	95.0	17.6	Inclusion Type
90Cu-10NaCl	"	104.0	15.4	" "
90Cu-10NaF	"	105.0	10.1	" "
90Cu-10LiF	"	115.0	3.6	" "
90Pb-10NaCl	90°-75%	4.9	1.0	Matrix Type
90Al-10NaCl	"	50.3	16.6	" "
90Ag-10NaCl	"	79.3	18.1	" "
90Cu-10NaCl	"	104.0	15.4	" "
90 Brass-10NaCl	"	186.5	22.2	" "
100Cu	"	147.7	"	Temperature(-108°F)
"	"	110.0	"	" (82°F)
"	"	95.0	"	" (307°F)
"	"	78.0	"	" (505°F)
"	"	80.9	"	" (705°F)
"	"	51.4	"	" (910°F)
"	"	34.0	"	" (1115°F)

*The included die angle and per cent reduction in area are listed.

APPENDIX D

MATRIX AND INCLUSION HARDNESS VALUES

Sample	Matrix Hardness		Inclusion Hardness	
	Before Extrusion	After Extrusion	Annealed Single Crystals	After Extrusion
90Pb-10NaCl	4.0	4.0	17.4	26.6
90Al-10NaCl	30.8	60.1	17.4	45.8
90Ag-10NaCl	36.8	97.0	17.4	31.4
90Cu-10NaCl	40.5	120.8	17.4	30.0
90 Brass-10NaCl	61.1	210.2	17.4	42.2
90Cu-10KCl	42.2	131.0	10.9	21.3
90Cu-10NaF	40.5	132.0	58.2	109.7
90Cu-10LiF	42.0	136.5	116.2	193.3
90Cu-10NaCl(-108°F)	40.5	134.0	17.4	31.4
90Cu-10NaCl(75°F)	40.5	120.8	17.4	30.0
90Cu-10NaCl(200°F)	40.5	110.0	17.4	42.6
90Cu-10NaCl(300°F)	40.5	101.0	17.4	52.7
90Cu-10NaCl(497°F)	40.5	89.0	17.4	48.5
90Cu-10NaCl(710°F)	40.5	63.0	17.4	37.4
90Cu-10NaCl(920°F)	40.5	54.4	17.4	34.4
90Cu-10NaCl(1139°F)	40.5	55.9	17.4	32.3
90Cu-10NaCl(1316°F)	40.5	56.5	17.4	30.6
100Cu (-108°F)	42.0	141.3	--	--
100Cu (82°F)	42.0	131.0	--	--
100Cu (307°F)	42.0	125.0	--	--
100Cu (505°F)	42.0	117.0	--	--
100Cu (706°F)	42.0	105.3	--	--
100Cu (910°F)	42.0	63.1	--	--
100Cu (1116°F)	42.0	62.7	--	--

APPENDIX E

HARDNESS VALUE EXTRAPOLATION

For the temperature effect study, it would be desirable to know the hardnesses of the sample phases at temperature. Room temperature hardness values were known for the NaCl inclusions and the copper matrix after extrusion at elevated temperatures. In addition, the hardness-temperature relationship was known for each pure phase. Based on this information, a method was sought to extrapolate the room temperature hardness data to elevated temperatures. The extrapolation method used will be presented in this section.

As a first approximation, the hardness was assumed to obey the following relationship

$$H = A e^{-BT} \tag{69}$$

where H is the hardness, T is the absolute temperature, and A and B are constants. Differentiating this equation leads to the result

$$\frac{dH}{dT} = -HB \tag{70}$$

Equation (70) shows that the rate of hardness decrease with increasing temperature is a function of the hardness. Between room temperature and an elevated temperature, the average value of $(\Delta H/\Delta T)$ was known for the pure annealed phases.

Based on Equation (70), we can write

$$\left(\frac{dH}{dT}\right)_u = \left(\frac{dH}{dT}\right)_p \frac{H_u B_u}{H_p B_p} \tag{71}$$

where p represents the pure, annealed phase and u represents the

phase where only the room temperature hardness is known. Assuming $B_u = B_p$, we can write

$$\left(\frac{dH}{dT}\right)_u = \left(\frac{dH}{dT}\right)_p \frac{H_u}{H_p} \tag{72}$$

Using the value of $(\Delta H/\Delta T)$ calculated from Equation (72), the elevated temperature hardness can be obtained from the following equation

$$\left(\frac{\Delta H}{\Delta T}\right)_u (T_e - T_o) = (H_e - H_o) \tag{73}$$

where the subscripts e and o denote the property of interest at the temperature of interest and room temperature, respectively.

In general, B_u would not equal B_p. The difference between these two quantities would be expected to increase as precipitation hardening occured in the NaCl inclusions. Consequently, the extrapolation for NaCl hardness values would get worse in the intermediate temperature range.

At best, this extrapolation method would only be expected to yield an approximation to the elevated temperature hardness values.

BIBLIOGRAPHY

1. Van Vlack, L. H., O. K. Riegger, R. J. Warrick, and J. M. Dahl, "Sulfide Inclusions in Steel," Trans. AIME, 221, 220-228, (1961).

2. Van Vlack, L. H., Elements of Materials Science, Addison-Wesley Publishing Co., Inc., Reading, Massachusetts, (1959).

3. Reusch, E., "On a Special Kind of Deformation in Rock-Salt and Calcite," Pogg. Ann., 132, 441, (1867). After ref. 19.

4. Coblentz, W. W., "Note on the Bending of Rock-Salt," Phys. Rev., 16, 389, (1903).

5. Milch, L., "The Increase of Plasticity of Crystals with Rise of Temperature," Neu. Jahrb. Min. Geol. Pal., 60-72, (1909).

6. Parker, E. R., J. A. Pask, J. Washburn, A. E. Gorum, and W. Luhman, "Ductile Ceramics - A High Temperature Possibility," J. Metals, 10, 351-353, (1958).

7. Gorum, A. E., E. R. Parker, and J. A. Pask, "Effect of Surface Conditions on the Room Temperature Ductility of Ionic Crystals," J. Am. Ceram. Soc., 41, 161-164, (1958).

8. Scheil, E., "Statistical Structure Investigations. I.," Zeitschrift fur Metallkunde, 27, 199-209, (1935).

9. Phillips, Jr., W. L., "Deformation and Fracture Processes in Calcium Fluoride Single Crystals," J. Am. Ceram. Soc., 44, 499-506, (1961).

10. Burn, R. and G. T. Murray, "Plasticity and Dislocation Etch Pits in CaF_2," J. Am. Ceram. Soc., 45, 251-252, (1962).

11. Wachtman, Jr., J. B., and L. H. Maxwell, "Plastic Deformation of Ceramic-Oxide Single Crystals," J. Am. Ceram. Soc., 37, 291-292, (1954).

12. Wachtman, Jr., J. B., and L. H. Maxwell, "Strength of Single Crystal Saphire and Ruby as a Function of Temperature and Orientation," J. Am. Ceram. Soc., 42, 432-433,(1959).

13. Bailey, S. W., R. A. Bell, and C. J. Peng, "Plastic Deformation of Quartz in Nature, "Geological Society of America Bulletin, 69, 1443-1466, (1958).

14. Turner, F. J., "Experimental Deformation of Calcite Crystals," Geological Society of America, Bulletin, 65, 883-933, (1954).

15. Howes, V. R., and S. Tolanski, "Pressure Crack-Figures on Diamond Faces. I. The Octahedral Face," Proc. Royal Soc., (London) A230, 287-293,(1955), also" II. The Dodecahedral and Cubic Faces," ibid, 294-301.

16. Schmid, E., and W. Boas, Kristallplastizitaet, Springer, Berlin (1936). English translation, Plasticity of Crystals, F. A. Hughes and Co., Ltd., London, (1950).

17. Laurent, J. F., "Plastic Deformation in Ionic Crystals," Le Journal de Physique et le Radium, 19, 602-611, (1958).

18. Pask, J. A. "Mechanical Properties of Ceramic Materials," 288-318 of Mechanical Behavior of Materials at Elevated Temperatures, J. E. Dorn, Ed., McGraw-Hill Book Co., Inc., New York, (1961).

19. Gilman, J. J., "Mechanical Behavior of Ionic Crystals," 146-199 of Progress in Ceramic Science, J. E. Burke, Ed., Pergamon Press, New York, (1961).

20. Dommerich, S., "Festigkeitseigenschaften bewässerter Salzkristalls. VI. Richtungsabhängigkeit der Streckgrenze gleichmässig abgelöster Steinsalzstäbchen," Zeit. Physik, 190, 189-196, (1934)

21. Pratt, P. L., "Similar Glide Processes in Ionic and Metallic Crystals," Acta Met., 1, 103-104, (1953).

22. Buerger, M. J., "Translation-Gliding in Crystals of the NaCl Structural Type," Amer. Mineralogist, 15, 174-187, (1935).

23. Gilman, J. J., "Plastic Anisotropy of LiF and Other Rock-Salt Type Crystals," Acta Met., 7, 608-613,(1959).

24. Shubin, G. V., "The Question of Brittleness and Plastic Deformations of NaCl," Izvest. Vysshikh Ucheb. Zavedenii, Fiz., No. 1, 98-103, (1961).

25. Tammann, G., and W. Salge, "Octahedral Glide of NaCl at High Temperatures. Decrease in the Yield Point with Rising Temperature," Neues Jahrb. Mineral. Geol. Palaon, suppl. 57, 117, (1927).

26. Rachinger, W. A., "Glide in Lead Telluride," Acta Met., 4, 647-649, (1956).

27. Huntington, H. R., J. E. Dickey, and R. Thompson, "Dislocation Energies in NaCl," Phys. Rev., 100, 1117-1128, (1955).

28. Van Zeggeren, F., and G. C. Benson, "Calculations of the Surface Energies of Alkali Halide Crystals," J. Chem. Phys., 26, 1077-1082, (1957).

29. Sears, G. W., "Strength of LiF Whiskers," J. Chem. Phys. Solids, 6, 300, (1958).

30. Gyulai, Z. Z. "Festigkeits- und Plastizitatseigenschaften von NaCl-Nadelkristallen," Zeit. Physik, 138, 317-321, (1954).

31. Hulse, C. O., "Formation and Strength of Magnesia Whiskers," J. Am. Ceram. Soc., 44, 572-575, (1961).

32. Stokes, R. J., "Dislocation Sources and the Strength of Magnesium Oxide Single Crystals," Trans. AIME, 224, 1227-1237, (1962).

33. Johnston, W. G. and J. J. Gilman, "Dislocation Velocities, Dislocation Densities, and Plastic Flow in Lithium Fluoride Crystals," J. Applied Physics, 30, 129-144, (1959).

34. Edner, A., "Einfluss von Fremdzusätzen auf die Kohäsionsgrenzen und die ultramikroskopische Solbildung Synthetischer Steinsalzkristalle," Zeit. Physik, 73, 623-648, (1932).

35. Schoenfeld, H., "Einfluss von Fremdzusatzen auf die Kohäsionsgrenzen und die ultramikroskopische Solbildung Synthetischer Steinsalzkristalle," Zeit. Physik, 75, 442-467, (1932).

36. Metag, W., "Einfluss von Fremdzusatzen auf die Kohasionsgrenzen und die ultramikroskopische Solbildung Synthetischer Steinsalzkristalle, Zeit. Physik, 78, 363-374, (1932).

37. Luhman, W. J. and A. E. Gorum, "The Effect of Impurities on the Strength of Silver Chloride," Acta Met., 7, 685-687, (1959).

38. Gorum, A. E., W. J. Luhman, and J. A. Pask, "Effect of Impurities on the Heat Treatment and Ductility of MgO," J. Am. Ceram. Soc., 43, 241-245, (1960).

39. Phillips, Jr., W. L., "Effect of Strain Rate and Temperature on the Stress-Strain Characteristics of NaCl, LiF, and MgO Single Crystals," Trans. AIME, 224, 434-436, (1962).

40. Pratt, P. L, "Point Defects and Mechanical Properties of Ionic Crystals," Inst. of Metals Monograph and Report Series, 99, (1957).

41. Eshelby, J. D., C. W. A. Newey, P. L. Pratt, and A. B. Lidiard, "Charged Dislocations and the Strength of Ionic Crystals," Phil. Mag., 3, 75-89, (1958).

42. Ekstein, H., "Torsion of NaCl," Unpublished work, quoted by Schmid, E., and W. Boas, Plasticity of Crystals, F. A. Hughes and Co., Ltd., London, (1950).

43. Westbrook, J. H., "Flow in Rock-Salt Structures," WADC Tech. Report, 58-304, ASTIA Document AD 15565, General Electric Co., Research Lab., (1958). After ref. 18.

44. Cottrell, A. H., Dislocations and Plastic Flow in Crystals, Oxford Press, London, (1953).

45. Vaughan, W. H. and J. W. Davisson, "Surface Mobility of Dislocations and the Joffe Effect," Report of NRL Progress, (April, 1959). After ref. 19.

46. Clarke, F. J. P. and R. A. J. Sambell, "Micro-cracks and their Relation to Flow and Fracture in Single Crystals of Magnesium Oxide," Phil. Mag., 5, 697-707, (1960).

47. Stokes, R. J., T. L. Johnston, and C. H. Li, "Evironmental Effects on the Mechanical Properties of Ionic Solids with Particular Reference to the Joffe Effect," Trans. AIME, 218, 655-662, (1960).

48. Kronberg, M. L., and J. E. May, "Ductility of Magnesium Oxide Single Crystals," J. Am. Ceram. Soc., 43, 438, (1960).

49. Lad, R. A., C. A. Stearns, and M. G. DelDuca, "Factors Affecting the Plasticity of Ionic Crystals," Acta Met., 6, 610-611, (1958).

50. Aerts, E. and W. Dekeyser, "Gases in Rock Salt and the Joffé Effect," Acta Met., 4, 557-558, (1956).

51. Class, W., E. S. Machlin, and G.T. Murray, "NaCl Embrittlement by Surface Compound Formation, AIME Trans., 221, 769-775, (1961).

52. Murray, G. T., "Brittle-Ductile Transition Temperatures in Ionic Crystals," J. Am. Ceram. Soc., 42, 330-334, (1960).

53. Bassett, G. A., "The Plasticity of Alkali Halide Crystals," Acta Met., 7, 754-755, (1959).

54. Stokes, R. J., T. L. Johnston, and C. H. Li, "Crack Formation in MgO Single Crystals," Phil. Mag., 3, 718-725, (1958).

55. Stokes, R. J., T. L. Johnston, and C. H. Li, "Further Observations of Stroh cracks in Magnesium Oxide Single Crystals," Phil. Mag., 4, 137-138, (1959).

56. Washburn, J., A. E. Gorum, and E. R. Parker, "Causes of Cleavage Fracture in Ductile Materials," Trans. AIME, 215, 230-237, (1959).

57. Keh, A. S., J. C. M. Li, and Y. T. Chou, "Cracks due to the Piling-up of Dislocations on Two Intersecting Slip Planes in MgO Crystals," Acta Met., 7, 694-696, (1959).

58. Stokes, R. J., T. L. Johnston, and C. H. Li, "Effect of Slip Distribution on the Fracture Behavior of MgO Single Crystals," Phil. Mag., 6, 9-24, (1961).

59. Stroh, A. N., Proc. Roy. Soc., A, 223, 404, (1954); ibid., 232 548, (1955); Advance Phys., 6, 418, (1957).

60. Cottrell, A. H., Theory of Brittle Fracture in Steels and Similar Metals," Trans. AIME, 212, 192-203, (1958).

61. Melankholin, N. M., and V. R. Regel, "Investigation of the Destruction Process of NaCl," Soviet Phys., JETP., 2, 696-702, (1956).

62. Bridgman, P. W., Studies in Large Plastic Flow and Fracture, McGraw-Hill Book Co., Inc., New York, (1952).

63. Bridgman, P. W., "The Effect of Hydrostatic Pressure on the Fracture of Brittle Substances," J. Appl. Phys., 18, 246-258, (1947).

64. Griggs, D., "Experimental Flow of Rocks under Conditions Favoring Recrystallization, Geological Society of America, Bulletin, 51, 1001-1022, (1940).

65. "Metallurgical Factors Affecting the Machinability of Steel," Metals Handbook, 1948 Edition, 369-371, The American Society for Metals, Cleveland, Ohio.

66. Knowlton, H. B., "Machinability of Wrought Metals," Machining of Steels, American Society for Metals, (1938).

67. Boulger, F. W., H. A. Moorhead, and T. M. Garvey, "Superior Machinability of MX Explained," Iron Age, 167, 90-95, (1951).

68. Cummings, H. N., F. B. Stulen, and W. C. Schulte, "Relation of Inclusions to the Fatigue Properties of SAE 4340 Steel," Trans. ASM, 49, 482-510, (1957).

69. Epremian, E. and R. F. Mehl, "Investigation of Statistical Nature of Fatigue Properties," National Advisory Committee for Aeronautics, Tech. note 2719, (June, 1952).

70. Frith, P. H., "Fatigue Tests on Rolled Alloy Steels made in Electric and Open-hearth Furnaces," I.S.I. Spec. Rep. No. 50, (1954).

71. Gadd, E. R., "Fatigue from the Metallurgist's Viewpoint," J. Royal Aeronautical Society, 57, 565-580, (1953).

72. Ransom, J. T., "The Effect of Inclusions on the Fatigue Strength of SAE 4340 Steel," Trans. ASM, 46, 1254-1263, (1954).

73. Stulen, F. B., "On The Statistical Nature of Fatigue," American Society for Testing Materials Symposium on Statistical Nature of Fatigue, STP No. 121, 23, (1952).

74. Stewart, W. C. and W. L. Williams, "Effects of Inclusions on the Endurance Properties of Steels," Journ. Am. Soc. Naval Engrs., 60, 475-504, (1948).

75. Gagnebin, A. P., "Selenium Additions to Cast Steel-Influence on Sulfide Inclusions and Ductility," American Foundryman, 12, 43-52, (1947).

76. "Nonmetallic Inclusions in Steel," Metals Handbook, 1948 Edition, 445-452, The American Society for Metals, Cleveland, Ohio.

77. Ogawa, S. Y., T. B. King, and N. J. Grant, "Deformation and Fracture Characteristics of Fe-S, Fe-S-O, and Fe-S-Mn Alloys at High Strain Rates and Temperatures," Trans. AIME, 224, 12-18, (1962).

78. Kinzel, A. B. and Walter Crafts, "Inclusions and their Effect on the Impact Strength of Steel," Iron Age, 127, 781-783,(1931).

79. Pickering, F. B., "Some Effects of Mechanical Working on the Deformation of Nonmetallic Inclusions," J. Iron and Steel Inst., 189, part 2, 148-159, (1958).

80. Scheil, E. and R. Schnell, "Mitt. Forsch Ver. Stahlwerke demnächst," after Scheil, E., "Statistische Gefügeuntersuchungen I," Zeitschrift für Metallkunde, 27, 199-209, (1935).

81. Dehlinger, U., Zeitschrift für Metallkunde, 26, 227, (1934) After ref. 8.

82. Van Vlack, L. H., "Correlation of Machinability with Inclusion Characteristics in Resulphurized Bessemer Steels," Trans. ASM, 45, 741-753, (1953).

83. Scheil, E. and W. Sibert, "Statistical Researches on Structure. IV. The Deformation of Inclusions of Iron Aluminide and Silicon Crystals in Aluminum on Rolling," Zeitschrift für Metallkunde, 32, 288-289, (1940).

84. Puttick, K. E., "The Structure, Deformation, and Fracture of Pearlite, Part II: Deformation and Structure," J. Iron and Steel Inst., 185, 167-176, (1957).

85. Gurland, J., "Metallographic Study of the Deformation of a Particle Strengthened Alloy, WC-Co," Division of Engineering Report, Brown University, Providence, R. I., Nonr 562(19)/1., (May, 1958).

86. Nishimatsu, C. and J. Gurland, "Experimental Survey of the Deformation of a Hard-Ductile Two-Phase Alloy System, WC-Co," Division of Engineering Report, Brown University, Providence, R. I., Nonr 562(19)/2., (Sept., 1958). Also, Trans. ASM, 52, 469-484, (1960).

87. Hill, R., The Mathematical Theory of Plasticity, Oxford Press, London, (1950).

88. Edelson, B. I., and W. M. Baldwin, Jr., "The Effect of Second Phases on the Mechanical Properties of Alloys," Trans. ASM, 55, 230-250, (1962).

89. Geisler, A., "Precipitation from Solid Solutions of Metals," Phase Transformations in Solids, John Wiley and Sons, New York, (1951).

90. Koppenaal, T. J., and N. M. Parikh, "Microstraining in Fiber-Reinforced Siver," Trans. AIME, 224, 1173-1176, (1962).

91. Keeler, J. H., "Tensile Properties of Zr-Cr Alloys-Particle Strengthening Effects," ASM Transactions, 48, 825-842, (1956).

92. Pearson, C. E., and R. N. Parkins, The Extrusion of Metals, 2nd Edition, John Wiley and Sons, Inc., New York, (1960).

93. Bishop, J. F. W., "The Theory of Extrusion," Metallurgical Reviews, 2, 361-390, (1957).

94. Wistreich, J. G., "Fundamentals of Wire Drawing," Metallurgical Reviews, 3, 97-142, (1958).

95. Sachs, G. and W. Eisbein, "Power Consumption and Mechanism of Flow in the Extrusion Process," Mitt. Material, 16, 67-96, (1931).

96. Johnson, W., B.I.S.R.A. Report, MW/E/55/54. After ref. 92.

97. Fink, C., Z. Bergwes, Prevsz., 22, 200, (1874). After ref. 92.

98. Siebel, E. and E. Fangemeier, "Researches on Power Consumption in the Extrusion and Punching of Metals, Mitt. K. W. Inst. für Eisenforschung, 13, 29-43, (1931).

99. Hoffman, O. and G. Sachs, Introduction to the Theory of Plasticity for Engineers, McGraw-Hill Book Company, Inc., New York (1953).

100. Treco, R. M., "Theoretical and Experimental Analysis of the Extrusion Process for Metals," Trans. ASM, 55, 697-718, (1962).

101. Hencky, H., "Über einige statisch bestimmte taelle des Gleichgewichts in plastische Gleichgewicht," Zeit. angew. Math. und Mech., 3, 241-251, (1923).

102. Geiringer, H., Proc. Third International Congress for Applied Mechanics, 2, Stockholm, (1930).

103. Prager, W. and P. G. Hodge, Jr., Theory of Perfectly Plastic Solids, John Wiley and Sons, Inc., New York, (1951).

104. Hill, R., "A Theoretical Analysis of the Stresses and Strains in Extrusion and Piercing," J. Iron Steel Inst. 158, 177-185, (February, 1948).

105. Johnson, W., "Extrusion Through Wedge Shaped Dies, Part I," J. Mech. Phys. Solids, 3, 218-223, (1955).

106. Johnson, W., "Extrusion Through Wedge Shaped Dies, Part II," J. Mech. Phys. Solids, 3, 224-230, (1955).

107. Johnson, W., "Extrusion Through Square Dies of Large Reduction," J. Mech. Phys. Solids, 4, 191-198, (1956).

108. Purchase, N. W. and S. J. Tupper, "Experiments with a Laboratory Extrusion Apparatus Under Conditions of Plane Strain," J. Mech. Phys. Solids, 1, 277-283, (1952-3).

109. Johnson, W., "Experiments in Plane-Strain Extrusion," J. Mech. Phys. Solids, 4, 269-282, (1956).

110. Dodeja, L. C. and W. Johnson, "Experiments in Plane-Strain Extrusion," J. Mech. Phys. Solids, 5, 269-282, (1957).

111. Shield, R. T., "Plastic Flow in a Converging Conical Channel," J. Mech. Phys. Solids, 3, 246-258, (1955).

112. Frisch, J. and E. G. Thomsen, "An Experimental Study of Metal Extrusions at Various Strain Rates," Trans. ASME, 76, 599-606, (1954).

113. Thomsen, E. G., C. Yang, and J. B. Bierbower, "An Experimental Investigation of the Mechanics of Plastic Deformation of Metals," University of California Publications in Engineering, 5, University of California Press, Berkeley, (1954).

114. Thomsen, E. G., and J. Frisch, "Stresses and Strains in Cold Extruding 2S-O Aluminum," Trans. ASME, 77, 1343-1353, (1955).

115. Thomsen, E. G., "Plasticity Equations and Their Application to Working of Metals in the Work Hardening Range," Trans. ASME, 78, 407-412, (1956).

116. Jordan, T. F., and E. G. Thomsen, "Comparison of an Unsymmetric Slip-Line Solution in Extrusion with Experiment," J. Mech. Phys. Solids, 4, 184-190, (1956).

117. Johnson, W., "The Pressure for the Cold Extrusion of Lubricated Rod Through Square Dies of Moderate Reduction at Slow Speeds," J. Inst. Metals, 85, 403-408, (1956-57).

118. Schishokin, W. P., "The Extrusion Properties of Metals and Alloys at Different Temperatures," Zhur. Priklad. Khimii, 2, 663, (1929). After ref. 92.

119. Taylor, G. I. and H. Quinney, "Combined Torsion and Tension of Thin Tubes, "Phil. Trans. Roy. Soc. A, 230, 323-362, (1931).

120. Barrett, C. S., Structure of Metals, McGraw-Hill Book Co. Inc., New York, (1952).

121. Moore, J. W., Personal Communication.

122. Chao, H. C., Personal Communication.